Faculty of Engineering and Information Technology

Research of Inductive Power Transfer System for Electric Vehicle

A thesis submitted for the degree of

Doctor of Philosophy

Shuo Wang

(2016)

Title of the thesis:

Research of Inductive Power Transfer System for Electric Vehicle

Ph.D. student:
Shuo Wang
E-mail: Shuo.Wang-1@student.uts.edu.au

Supervisor:
A/Prof. Youguang Guo
E-mail: Youguang.Guo-1@uts.edu.au

Co-Supervisor:
Dr. Li
E-mail: Li.Li@uts.edu.au

External Supervisor:
Prof. David Dorrell
E-mail: dorrelld@ukzn.ac.za

Address:
School of Electrical, Mechanical and Mechatronic Systems
University of Technology Sydney, NSW 2007, Australia

Certificate of Original Authorship

I certify that the work in this thesis has not previously been submitted for a degree nor has it been submitted as part of requirements for a degree except as fully acknowledged within the text.

I also certify that the thesis has been written by me. Any help that I have received in my research work and the preparation of the thesis itself has been acknowledged. In addition, I certify that all information sources and literature used are indicated in the thesis.

Signature of Student:

Shuo Wang

Date:

Acknowledgments

My thesis could not have come to fruition without the assistance of many contributors.

Hereby, I would express my deep gratitude to my supervisors Professor David Dorrell, Associate Professor Youguang Guo and Dr. Li.

Professor Dorrell supported me with great direction, advices and any other helps in my research. His optimism, patience, motivation, and immense knowledge, has been inspiring me in the past four years. His patient and guidance on solving problems, writing reports and oral communicating with profession rewards my entire research life.

Associate Professor Guo spent plenty of time discussing from experiment design to thesis writing with me and gave me many great advices. He is a model for me in professional integrity.

I am grateful to my co-supervisor Dr Li for his support with my presentations and reviewing the draft.

I would also express my gratitude to Associate Professor Peter Watterson, Dr Paul Walker Dr. Guangzhong Xu, Dr. Chengcheng Liu, Mr. Russell Nicolson, and Mr. Laurence Stonard, for their help with my research.

I would like to thank my colleagues, Dr. Lei Zhang, Dr. Jiageng Ruan, Dr.Sangzhi Zhu, Dr. Xingxing Zhou, Dr. Tianxiao Zhang, Dr. Yu Wang, Dr. Jinglai Wu, and Mr. Jianwei Zhang for their supports.

I also wish to gratefully acknowledge the consistent financial support of the following agents: China Scholarship Council (CSC) and University of Technology, Sydney (UTS).

Most especially to my family, words alone cannot express what I own them for their encouragement and whose patient love enabled me to complete this thesis. Firstly, it is my father Yanzhi Wang my my mother Huapeng Wu. I left China for my study in Australia and

couldn't visit my parents regularly during my past 4 years. My parents never said a word about my absent as their child but just showed their understanding. Secondly, I would like thank my unle Dehong Yu and aunt Huayou Wu. They taught me so much, from living in Australia to how to do research. Finally, I would like to thank my wife, Hongjun Qiao. She came to Australia to support my study and always encourage me. Our time here together in Australia would be my best memories.

Publications and Conference Contributions

The following publications are part of the thesis

Peer reviewed international scientific journal publications

1. S. Wang and D. G. Dorrell, "Loss analysis of circular wireless EV charging Coupler," in IEEE Trans. Magn., vol. 50, no. 11, pp. 1-4, Nov. 2014.
2. S. Wang and D. G. Dorrell, "Copper loss analysis of EV charging coupler," IEEE Trans.Magn., vol. 51, no. 11, pp. 1-4, Nov. 2015.
3. S. Wang, D. G. Dorrell, Y. Guo and M. F. Hsieh, "Inductive charging coupler with assistive coils," IEEE Trans. Magn., vol. 52, no. 7, pp. 1-4, July 2016.

Peer reviewed international scientific conference publications

1. S. Wang and D. G. Dorrell, "Review of wireless charging coupler for electric vehicles", Proc. IEEE 39th Annu. Conf. Ind. Electron. Soc. (IECON), pp. 7274-7279
2. S. Wang and D. Dorrell, "Simulation of electric vehicle inductive charging system," 2015 IEEE 11th International Conference on Power Electronics and Drive Systems, Sydney, NSW, 2015.

Abstract

Electric vehicles are a promising option for future transportation. The technology related to these have undergone rapid development over the last two decades and there are now many commercial electric vehicles available on the market. However, consumers still suffer from the "range anxiety" due to the limited driving range and long recharging time (refuelling time) compared to traditional internal combustion engine vehicles. Wireless charging is an alternative recharging option; currently the usual recharging method uses plug-in charging. With wireless charging, the connection between grid and vehicle can be established in less than a second without any manual operation. Therefore, recharging EVs can take place during a short stop or in motion. This means that there are more recharging windows available during vehicle use which would effectively extend the range of the vehicle and reduce consumers "range anxiety".

This work is divided into three parts. The first part addresses the background and reviews the literature on EV recharging technologies. This is formed from first two chapters: Chapter 1 provides the introduction and outline of this thesis; Chapter 2 puts forward a literature review of the state of the art of recharging technology. The design of the wireless charging coupler is reviewed in this chapter.

The second part is the study of the inductive charging system. Chapter 3 introduces the wireless charging pad analysis, which includes a circular pad and a rectangular pad analysis. The parameters of the pads are analysed. An analytical and numerical combined method for resistance analysis is introduced to wireless charging coupler resistance analysis which is

the first contribution of this research. And Chapter 4 proposes a pad geometry with assistive coils which is a new arrangement that improves the coil coupling which is the secondary contribution of this study. Chapter 5 analyses the inductive power transfer system at circuit level, and experiment validation is carried out.

Finally, conclusions and future work are given in Chapter 6.

Keywords: *EV, Wireless charging technology, Pad design, Pad analysis, Inductive charging system analysis*

.

Contents

Certificate of Original Authorship i
Acknowledgments ii
Publications and Conference Contributions iv
Abstract v
List of Tables xi
List of Figures xii
Nomenclature xvii
Chapter 1 1
Introduction 1
1.1 Background 1
1.2 Research Objectives 3
1.3 Thesis Outline 4
1.4 Reference 6
Chapter 2 7
Literature Review of EV Charging Methods 7
2.1 Conductive charging method 10
2.1.1 Single Stage Charger 12
2.1.2 Two Stage Charger 13
2.1.3 Off Board Charger 15
2.2 Wireless Charging Methods 16
2.2.1 EV Wireless Charging Technologies 18
2.2.2 Magnetic Resonance Coupling Transfer 21
2.2.3 Permanent Magnet Coupling 22
2.2.4 Inductive Charging Method 23
2.3 Review of EV Inductive Charging Technology 23

2.3.1 Coupler Power Source 25
2.3.2 Compensation 27
2.3.3 Stationary Wireless Charging Coupler 29
2.3.4 On-Line/In-Motion Charging 34
2.3.5 Discussion 38
2.4 Summary 40
2.5 References 42
Chapter 3 52
Analysis of Wireless EV Charging Coupler 52
3.1 Introduction 52
3.1.1 Circular Pad Structure 53
3.1.2 Power Levels 53
3.1.3 Self and Mutual Inductances of Coils 54
3.1.4 Modelling of the IPT system 56
3.2 Pad Analysis 59
3.2.1 Analysis Methods 59
3.2.2 Simulation Environment 61
3.2.3 Simulation Result 63
3.3 Copper Loss analysis 72
3.3.1 Skin and Proximity Effect Loss and Calculation Method 73
3.3.2 Loss Analysis of a Conductor 76
3.3.3 Wire Geometric Modelling 77
3.3.4 Coupler Model and Results 83
3.4 Rectangular Pad Analysis 85
3.4.1 Rectangular Pad Simulation 85
3.4.2 Experiment Validation 97
3.5 Summary 100
3.6 Reference 102

Chapter 4 104
Inductive Charging Coupler with Assistive Coils 104
4.1 Introduction 104
4.2 Wireless Charging Systems 105
4.2.1 Two Winding Structure 106
4.2.2 Four Winding Structure 109
4.3 Proposed Coupler with Assistive Coils 111
4.3.1 Circuit Model for Proposed Coupler 113
4.3.2 Simulation Results 114
4.3.3 Circuit Analysis 116
4.4 Summary 119
4.5 References 120
Chapter 5 122
IPT System Analysis 122
5.1 Circuit Analysis with Compensation 123
5.1.1 System Efficiency Relationship with Rload. 123
5.1.2 Secondary Side Output Current 125
5.1.3 Efficiency with the mutual inductance 126
5.1.4 IPT System Performance versus Frequency 128
5.1.5 Impedance Analysis 129
5.2 System Simulation 131
5.2.1 DC Input Simulation 131
5.2.2 Full bridge Inverter 132
5.2.3 Phase shift Control 133
5.2.4 IPT System Simulation Results 135
5.2.5 Charger with Three Phase AC Source Simulation Results 140
5.3 Experiment 143
5.3.1 Coupler setup 145

5.3.2 Power Electronics setup 146
5.3.3 Experiment Result 148
5.4 Summary 154
5.5 References 155
CHAPTER 6 157
Conclusions and Future Work 157
6.1 Conclusions 157
6.2 Future Work 158

List of Tables

Table 2-1. Levels of EV chargers 8
Table 2-2. Battery Charging Methods [2.7] 14
Table 2-3 General Parameters for Three Generations of On-Line EV Charging 36
Table 3-1. Basic Geometrical Parameters 62
Table 3-2. Ferrite Material Characteristics 66
Table 3-3. Parameters of the Wireless Charger 67
Table 3-4. Parameters of the Wireless Charger 71
Table 3-5. Parameters of Simulated Wires 79
Table 3-6. Copper Loss of Primary Side Winding Types 2 and 3 at 20 kHz 85
Table 3-7. Rectangular Pad Parameters 86
Table 3-8. Inductance from Experiment and Simulation 98
Table 3-9. Measured Laid and calculated k with spacing 99
Table 4-1 Parameters of Simulated Coupler 111
Table 4-2 Inductance Matrix of Four Coils 114
Table 4-3 Coupling Coefficient Matrix of Four Coils 115
Table 5-1 Parameters for Efficiency Analysis 125
Table 5-2. Frequency Analysis Parameters 128
Table 5-3 Parameters of the IPT system 130
Table 5-4. Output Power with Phase Shift Angle 138
Table 5-5. System Efficiency Versus Load 153

List of Figures

Fig. 2.1. A unidirectional topology used for Level 1 chargers. 9
Fig. 2.2 A unidirectional topology for Levels 1 and 2 chargers. 9
Fig. 2.3. A bidirectional topology for Level 3 chargers. 10
Fig. 2.4. Structure for conductive charging. 11
Fig. 2.5. Classification of conductive chargers 12
Fig. 2.6. AC/DC conventional boost rectifier [8] 13
Fig. 2.7. Dual active bridge DC/DC converter. 15
Fig. 2.8. General structure for Level 3 fast Charging. 16
Fig. 2.9 Wireless charging technology 21
Fig. 2.10. MRCT EV charging system. 22
Fig. 2.11 General structure of the IPT system. 24
Fig. 2.12 Full bridge inverter. 26
Fig. 2.13. Basic compensation topology. 28
Fig. 2.14. IPT system: a) early IPT charging system, b) IPT charging system with compensation. 30
Fig. 2.15. Flux of circular pad. 31
Fig. 2.16. Top view and cross view of a flux pipe pad. 32
Fig. 2.17. Structure of DD pad: (a) top view (b) cross view. 33
Fig. 2.18. A possible lumped on road charging. 35
Fig. 2.19. Three phase track topologies: (a) bipolar and (b) unipolar. 37
Fig. 2.20. The top view and cross view of OLEV power transfer system: (a) dual type and (b) mono type. 38
Fig. 3.1. Geometry of circular pad. 53
Fig. 3.2. Concept of mutual inductance using two magnetically coupled loops. 55
Fig. 3.3. Circuit model of IPT system. 56
Fig. 3.4. Circuit model using equivalent source for coupler windings *Lp* and *Ls*. 57

Fig. 3.5. Circular pad full scale FEA simulation model. 61

Fig. 3.6. Maxwell 3D representation of one-6th section. 63

Fig. 3.7. Coupling factor *k* for transformer with and without ferrite cores. 65

Fig. 3.8. Flux density in the ferrite cores. 67

Fig. 3.9. Voltages of secondary winding and capacitor 68

Fig. 3.10. Ohmic losses in the shield and ferrite core. 69

Fig. 3.11. Flux Leakage. 70

Fig. 3.12. Force on the winding. 72

Fig. 3.13. Concept of skin and proximity effects on stranded and bundled conductors. 75

Fig. 3.14. Simulation model of wires a) single conductor; b) 61 strands model; c) 349 strands 78

Fig. 3.15. Loss distribution in a single conductor. 80

Fig. 3.16. Loss of single conductor wire verse frequency and radius. 81

Fig. 3.17. (a) Skin effect factor of wires; (b) Proximity effect G factor of wires. 82

Fig. 3.18. (a) Maxwell 3D representation of one-sixth section; (b) The magnetic field strength along the wire over time. 82

Fig. 3.19. The magnetic field strength over winding. 83

Fig. 3.20. Simulation model of rectangular pad: a) coupler model side view, b) top view of primary side coupler. 85

Fig. 3.21. Self-inductances of primary and secondary windings and mutual inductance with 186 mm ferrite bar on both sides 86

Fig. 3.22. Mutual inductance versus misalignment with 186 mm ferrite bar on both sides 87

Fig. 3.23. Mutual inductance versus air bap distance with 186 mm ferrite bar on both sides 87

Fig. 3.24. Coupling coefficient versus misalignment and air gap distance with 186 mm ferrite bar on both sides 89

Fig. 3.25. Secondary side coil with 93 mm ferrite bar simulation 90

Fig. 3.26. Inductance of primary and secondary winding and mutual inductance with 93 mm ferrite bar on secondary side 90

Fig. 3.27. Mutual inductance versus air gap distance with 93 mm ferrite bar on secondary side 91

Fig. 3.28. Mutual inductance versus misalignment with 93 mm ferrite bar on secondary side 91

Fig. 3.29. Coupling coefficient versus misalignment and air gap distance with 93 mm ferrite bar on secondary side 92

Fig. 3.30. FEA model for secondary side coil only pad..... 92

Fig. 3.31. Inductance of primary and secondary winding and mutual inductance of secondary side coil only pad 93

Fig. 3.32. Mutual inductance versus air gap distance with secondary side coil only pad.... 94

Fig. 3.33. Mutual inductance versus misalignment with secondary side coil only pad. 94

Fig. 3.34. FEA model for coil only pad. 95

Fig. 3.35. Inductances of primary and secondary windings, and mutual inductance of coil only pad..... 95

Fig.3.36 Mutual inductance versus air gap distance with coil only pad 96

Fig. 3.37. Mutual inductance versus misalignment with coil only pad..... 96

Fig. 3.38. Comparison of mutual inductance of different pads..... 97

Fig. 3.39. Rectangular pad setup. 98

Fig. 3.40. Experiment and FEA results of coupling coefficient k..... 100

Fig. 4.1. Wireless charging circuit. 106

Fig. 4.2. General structure for series-series compensation. 107

Fig. 4.3. Simulation results: (a) uncompensated circuit efficiency and power output, (b) SS compensated efficiency and power output..... 109

Fig. 4.4. General structure for four-coil system. 111

Fig. 4.5. General structure for four-coil system: a) 3D view of transformer; b) top view of primary coupler; c) side view of primary coupler..... 112

Fig. 4.6. Circuit model for proposed coupler with assistive coil system. 113

Fig. 4.7. Coupling coefficient via airgap length` 115

Fig. 4.8. Two-coil system characteristic with *C1* and *C4*. 117

Fig. 4.9. Proposed coupler optimisation (efficiency and power maps)..... 118

Fig. 5.1. Efficiency versus R_{load}..... 125

Fig. 5.2. Efficiency map of mutual inductance and Rload..... 127

Fig. 5.3. Pout and efficiency versus HF power source frequency..... 129

Fig. 5.4. The frequency analysis: a) impedance verse frequency, b) Phase angle versus frequency..... 131

Fig. 5.5. IPT system simulation model 132

Fig. 5.6. Full bridge inverter. 133

Fig. 5.7. The phase shift control for full bridge Inverter..... 134

Fig. 5.8. Full bridge output voltage and output current 135

Fig. 5.9. Load voltage V_{load} and current $I_{load.}$ 136

Fig. 5.10. Output power (top) and input power waveforms (bottom). 136

Fig. 5.11. Inverter output voltage and current at α =120. 137

Fig. 5.12. Output power (top) and input power waveforms at α =120^{o}. 138

Fig. 5.13. Output power and input power versus phase shift angle 139

Fig. 5.14. Efficiency versus phase shift angle. 140

Fig. 5.15. Simulation model of IPT system with three phase input. 141

Fig. 5.16. Output current of three phase rectifier. 141

Fig. 5.17. Three phase rectifier DC link voltage. 142

Fig. 5.18. Three phase IPT system input power and output power. 142

Fig. 5.19. IPT experiment circuit. 143

Fig. 5.20. Test rig: primary side. 144

Fig. 5.21. Test rig: coupler and load. 144

Fig. 5.22. a) Coupler primary side, and b) Coupler 146

Fig. 5.23. Rectifier module and IGBT module for experiment. 147

Fig. 5.24. Schematic diagram of gate drive. 148

Fig. 5.25. PCB view of gate drive. 148

Fig. 5.26. DSP output, gate drive signal and the inverter output. 149

Fig. 5.27. Time delay between the drive signal and the output voltage. 150

Fig. 5.28. The voltage and current inputs of the primary side. 151

Fig. 5.29. The voltage, current and power to the load. 151

Fig. 5.30. Inverter output voltage and current at 21 kHz. 152

Fig. 5.31. Inverter output voltage and current at 20 kHz 152
Fig. 5.32. System efficiency versus load resistance 153

Nomenclature

Global abbreviations used in this thesis

AC	=	Alternating current
CO_2	=	Carbon dioxide
DC	=	Direct current
EMI	=	Electromagnetic interface
EV	=	Electric vehicle
FEA	=	Finite element analysis
FEM	=	Finite element method
HEV	=	Hybrid electric vehicle
HF	=	High frequency
MRCT	=	Magnetic resonance coupling transfer
PFC	=	Power factor correction
PMCT	=	Permanent magnet coupling transfer
SWC	=	Stationary wireless charging
WPT	=	Wireless power transfer

Chapter 1

Introduction

1.1 Background

There is a great increase in the number of the vehicles on road in recent years and the total number is expected to reach the level of 2.5 billion in 2050 [1.1]. Although there is an improvement in the vehicle efficiency, the greenhouse gas emission (GHG) from vehicles has been offset by the increased total travel of vehicles. About 40% of the growth in carbon dioxide (CO_2) emissions from all energy-using sectors is produced by the transportation since 1990. Reducing the GHG emission from vehicles is becoming a serious issue, as GHG is a major factor in climate changes.

In recent years, the electric vehicle (EV) and hybrid electric vehicle (HEV) has regained the attention of researchers because they are considered better choice than internal combustion engines vehicles in reducing the GHG, especially in urban area. The EV and HEV produce no GHG emission on road. Vehicles that travel fewer than 50 km per day, which is within the range of using on board battery only, are responsible for more than 60% of daily passenger vehicle km [1.2], so using electricity to power the vehicles would dramatically shift the GHG emissions and criteria pollutants from distributed vehicle tailpipes to large centralized power plants which could produce less GHG emission while generating the same amount of energy for its high efficiency. The assessment has proved that the greenhouse gas

emission from plug-in electric vehicles reduces the GHG emissions by 32% compared to conventional vehicles.

Although the HEV and EV could reduce the GHG emission, they are still not widely accepted by the consumers due to the limitation of the price and the driving range, especially for the latter.

There are several ways to extend the EV driving range, and more on board battery cells is one of them. Extra battery cells increase the total possible energy on board. Therefore, the driving range of EV would be longer. On the other hand, however, extra battery also means more weight and volume for the on board energy storage. And as energy density of battery is still low compared to gasoline, the energy storage system would have a significant increase in weight and volume. The range/cells ratio also would decrease after the battery on board reaches certain limit.

At the same time the cost of the on board energy storage would increases if extra battery is added. The price for the EV battery is a serious issue. The raw materials are expensive, and even with mass production, the price might not show a significant decrease in the future. [1.3]. Expensive energy storage would leads to high cost for production as well as market price of EV.

Another reason for "range anxiety" is the time for EV to "refill the tank". High energy density batteries are used for EV applications, such as the lithium-ion battery cells in Tesla sports car, but recharging time is still relatively long compared to refilling a gasoline tank. For Tesla sports car, which is an EV, the 53 kWh on board battery storage requires approximately 7

hours to charge using a 240 volt, 40-amp outlet, and 4.5 hours using 240 volts, 70-amp outlet. The Prius Plug-in Hybrid with 4.4 kWh battery capacity will take 1.5 hours with 240 volts' outlet [1.4]. The recharging power of the battery is limited, in order to protect the battery and reach a longer life cycle. Although supercapacitors are introduced to overcome the battery disadvantage in power ratio, the fast recharging is only for short distance/ emergency recharging. The energy density and power density issues are still not solved for long distance drive over the EV driving range. Therefore, it is necessary to have more charging opportunities for EV.

1.2 Research Objectives

In order to develop high efficiency inductive charging system for EV, the focus of this thesis is to solve technical problems related to coupler parameter estimation, charging system modelling, and high performance coupler design. The main objectives of this research project can be described as:

- Develop finite element analysis model to achieve accurate coupler parameters for accurate circuit modelling;
- Analyse the resistance of coupler to get estimation of copper loss model; and
- Propose new coupler geometry to reduce the power-efficiency splitting and increase the misalignment tolerance.
- Analysis the IPT system performance on circuit level

1.3 Thesis Outline

The thesis is organised at follows:

In Chapter 1, the background and motivation of this thesis are introduced, defining the main focus in the development of wireless charging technology.

In Chapter 2, the electric vehicle charging methods including conductive and wireless charging technologies are reviewed and compared. The state of art inductive charging technologies is reviewed in three key areas: 1) Pad geometry design, 2) Compensation circuit, and 3) Power electronics design and control.

In Chapter 3, the geometry analysis methods are introduced. A circular pad model based on the finite element analysis is built and simulated in both magnetostatic and transient solvers. The inductance of the winding is simulated with different airgaps and misalignments. The core loss in this model is analysed via simulation. The resistance of Litz wire is further investigated. An inductive charging pad Litz wire AC resistance analysis method based on FEA and analytical model is presented. The eddy current effect AC resistance and proximity effect resistance are analysed. Three types of Litz wire are analysed as circular pad winding candidates based on the model in Chapter 3.

In Chapter 4, the two coil system and four coil system characteristics are presented. The pad structure is investigated. A new four coil pad geometry is proposed. By introducing four assistive coils, the stability of pad is reached.

In Chapter 5, the FEA analysis of a rectangular pad is presented. The two coil performance with Series-Series compensation is investigated. A circuit model is simulated in Simulink based on parameters from the FEA analysis. The experiment is setup based on above simulation.

In Chapter 6, the conclusions of the thesis are drawn, accompanied by future work proposal.

1.4 Reference

[1.1] OECD and I. T. Forum., ITF Transport Outlook 2015: OECD Publishing. DOI: http://dx.doi.org/10.1787/9789282107782-en.

[1.2] C. Samaras and K. Meisterling, "Life Cycle Assessment of Greenhouse Gas Emissions from Plug-in Hybrid Vehicles: Implications for Policy," Environmental Science & Technology, vol. 42, pp. 3170-3176, 2008.

[1.3] S. Lukic, J. Cao, R. C. Bansal, F. Rodriguez and A. Emadi, "Energy storage systems for automotive applications", IEEE Trans. Ind. Electron., vol. 55, no. 6, pp. 2258-2267, Jun. 2008.

[1.4] M. Yilmaz and P. T. Krein, "Review of Battery Charger Topologies, Charging Power Levels, and Infrastructure for Plug-In Electric and Hybrid Vehicles," IEEE Trans. Power Electron., vol. 28, pp. 2151-2169, 2013.

Chapter 2

Literature Review of EV Charging Methods

The EV charger plays a great role in the EV technology. The recharging time and the lifecycle of the battery are related to the EV charger. It is supposed to be high efficiency, low cost, low weight, low volume, etc. The charger is supposed to have low disturbance to the power grid. The unity power should be ensured to minimise the impact on power quality. Also, it would maximise the amount of real power delivered via the charger.

The allowable harmonics and DC current injected to the power grid are limited in several standards [2.1]. Generally, the power factor correction (PFC) would be the first stage for the charger, and many different topologies for the PFC were proposed, such as using boost converter, parallel boost, full bridge, and multilevel converter.

The chargers are catalogued into three different levels by the power and voltage ratio as shown in Table 2-1. Different levels of chargers are for different locations and different charging circumstances. As different countries may have different standards for grid voltage and frequency, the same level charger has different voltage ratios.

Levels 1 and 2 chargers would be the primary charging options for private recharging facilities. Level 1 charger could be installed at home or mostly is expected be integrated on board. A unidirectional topology for Level 1 chargers is shown in Fig. 2.1. Level 2 chargers are designed as the major choice in private and public recharging facilities. The installation

of equipment for this level may be required as the chargers may not be fully integrated on board. A unidirectional topology for Level 2 chargers is shown in Fig. 2.2.

Table 2-1. Levels of EV chargers

Power level types	**Charger Location**	**Typical Use**	**Expected Power Level**	**Charging Time (Hour)**	**Vehicle Technology**
Level 1 (Opportunity) **120 Vac (US)** **230 Vac (EU)**	On-Board 1-Phase	home or office	1.4kW(12A)	4-11	PHEVs (5-15kWh)
			1.9kW(20A)	11-36	EVs (16-50kWh)
Level 2 (Primary) **240 Vac (US)** **400 Vac (EU)**	On Board 1 phase or 3 phase	Private /Public Outlets	4kW (17A)	1-4	PHEVs (5-15kWh)
			8kW (32A)	2-6	EVs (16-30kWh)
			19.2kW (80A)	2-3	EVs (3-50kWh)
Level 3 (Fast) **208-600 Vac or Vdc**	Off Board 3 phase	Commercial filling station	50kW	0.4-1	EVs
			100kW	0.2-0.5	(20-50kWh)

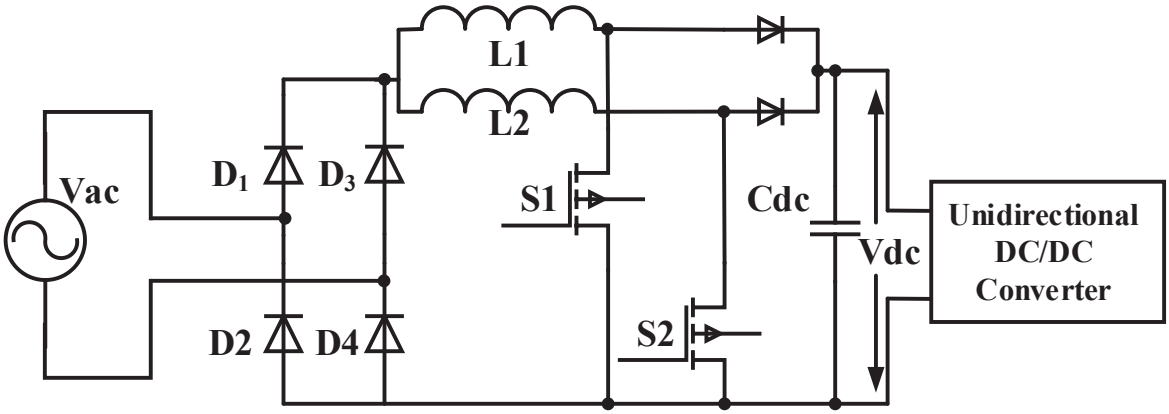

Fig. 2.1. A unidirectional topology used for Level 1 chargers.[2.1]

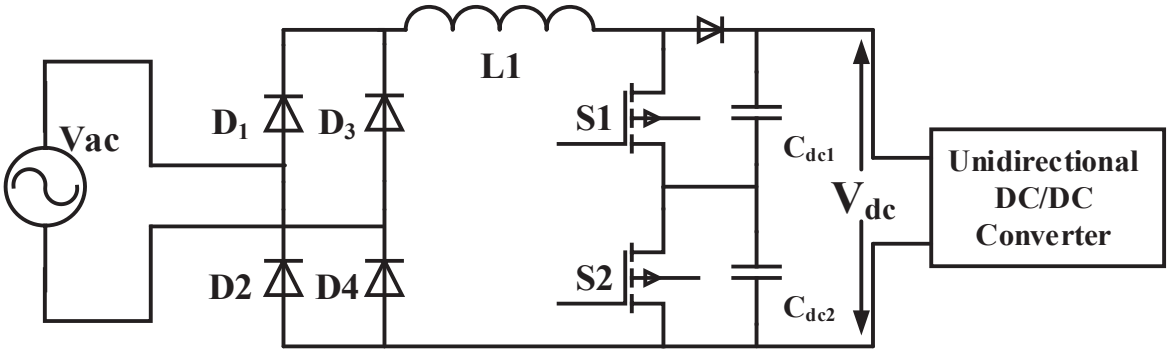

Fig. 2.2 A unidirectional topology for Levels 1 and 2 chargers. [2.1]

Fast charging would be on level 3, which is the commercial recharging facility level. A topology for level 3 chargers is shown in Fig. 2.3. This level offers possibility of 1-hour recharging. It would be the primary choice for the highway rest area, the city recharging station or shopping centre car park. The off board equipment is required to control the high power flow to the EV. As the voltage and power rating are much higher than those for Levels

1 and 2, it may require supervision during charging process, and the facility should be well maintained at all time.

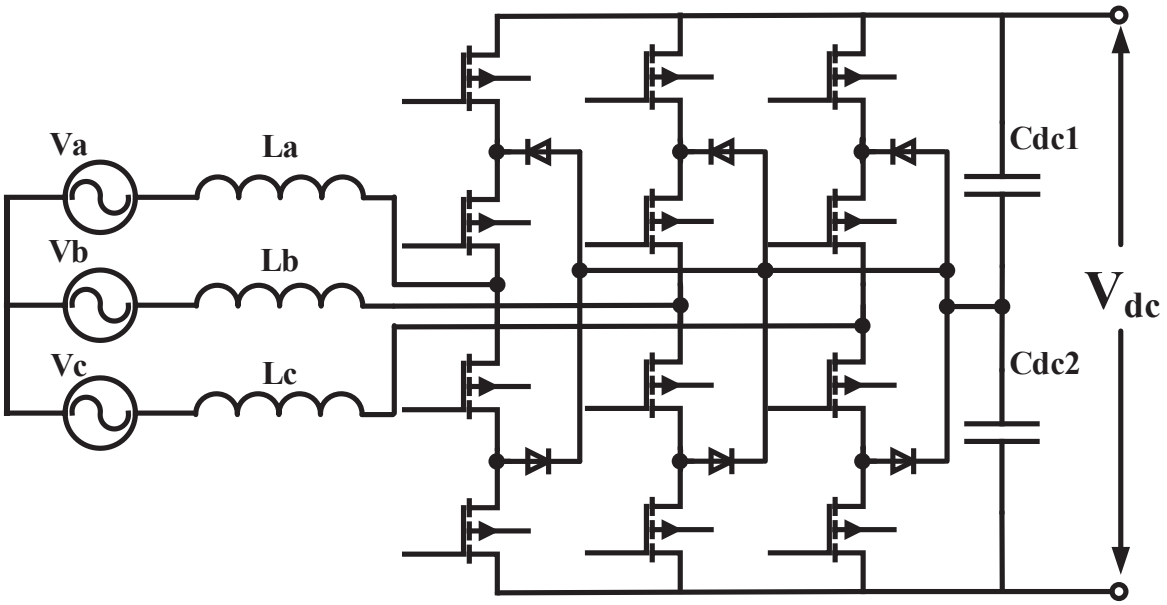

Fig. 2.3. A bidirectional topology for Level 3 chargers.[2.1]

The conductive charging and inductive charging are the major methods for EV recharging. The conductive charging method has a cable which connects the power sockets and the EV. And in inductive charging, conduction cable is replaced by electromagnetic interface (EMI). There would be an airgap between the grid side and the EV side.

2.1 Conductive charging method

The general structure of conductive charger is shown in Fig. 2.4. The AC current is transferred via the power grid. However, for batteries, the output voltage is DC due to its chemical characteristic. In order to recharge the battery, DC source is necessary. From Fig.

2.4, it can be seen that the single/three phase AC current from grid is rectified to the DC via a rectifier, followed by a DC to DC converter. The energy storage system is connected and recharged by the DC/DC converter. Therefore, topologies of conductive charging could be catalogued by different rectifiers and DC converters stages. Also, it could be catalogued into on board charger and off board charger by its location, as shown in Fig. 2.5. The following sections will review those chargers.

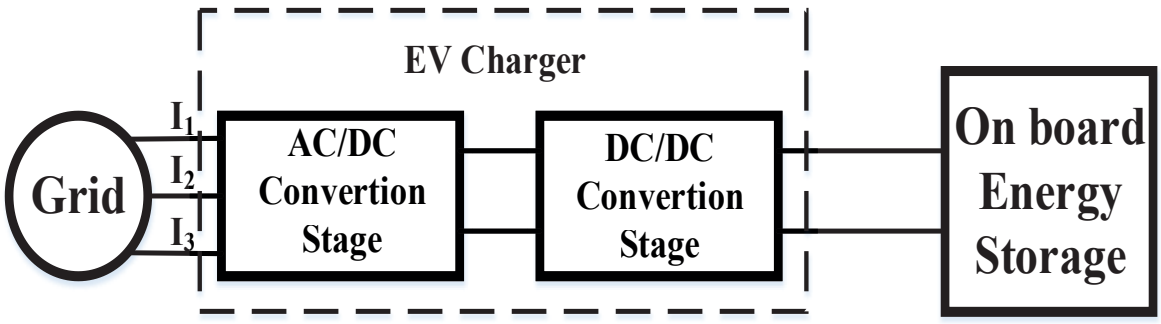

Fig. 2.4. Structure for conductive charging.

The on board charger is for Level 1 and Level 2 charging facility, which is relatively low power comparing to Level 3 charger which is off board. The design objective for the on board charger is to minimise the weight and volume while satisfying the required power level and standards.

The on board charger could be further classified into single stage charger, two stages charger, and integrated charger [2.2]. The single stage charger is an on board AC/DC interface between the battery and grid, while two stages charger has an AC/DC rectifier on grid side, and DC/DC converter on the battery side. The integrated charger combines the charging

circuit with propulsion circuit in the EV powertrain, which reduced the components number, size and weight.

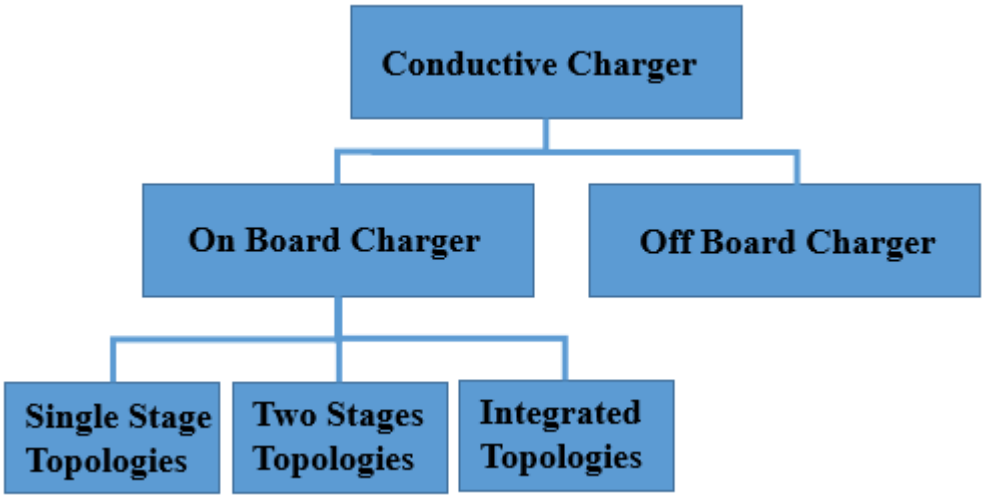

Fig. 2.5. Classification of conductive chargers

2.1.1 Single Stage Charger

Single stage charger is opportunity battery charger which is supposed to be low power on board charger. It offers the simplest topology with the least components to acquire low volume and weight on board. The most widely used topologies for single stage charger are half bridge, full bridge, and multi-level converters [2.3]. Those topologies reach high efficiency with limited number of components. However, there is no galvanic isolation in the circuits. Galvanic isolation is important features for safety reason, and a single stage isolated charger was proposed in [2.4].

2.1.2 Two Stage Charger

The two-stage charger includes rectifier and DC/DC stages. The rectifier stage may not be carried on board, depending on specific design to reduce the total weight and component counts on board. The rectifier converts AC power to DC as well as the charger power quality to grid, and the DC/DC converter manages the charging for battery.

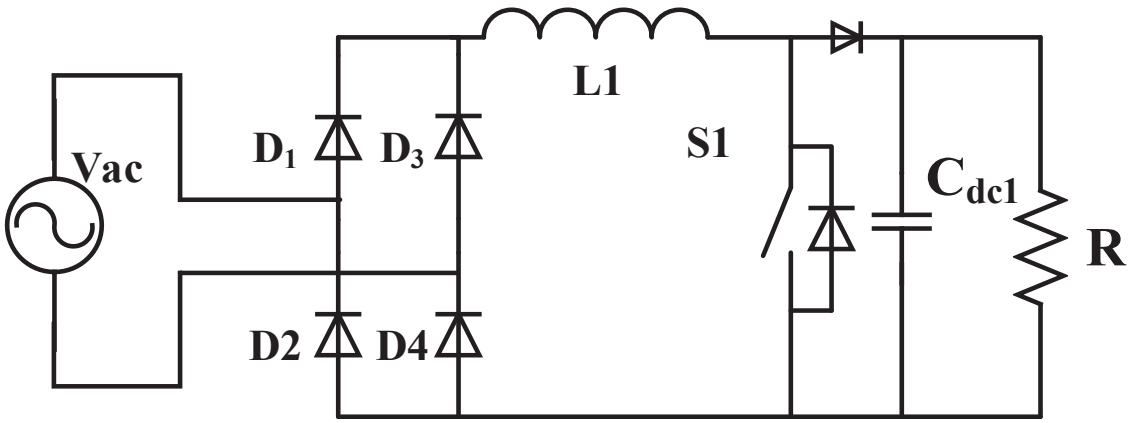

Fig. 2.6. AC/DC conventional boost rectifier [8]

A. Rectifier with Power Factor Correction

The major role for the rectifier is to supply DC power link for the DC converter stage. At the same time, unity power factor and low harmonics in AC side is required for quality input. There are many factors to be considered for rectifier such as efficiency, power factor, cost, robustness, control complexity and total harmonic distortion (THD). Boost rectifier is widely used for its simplicity in topology and control. A conventional boost rectifier is shown in Fig. 2.6 [2.5].

There is only one fully controlled device in the boost stage, which makes the rectifier at low cost. The conduction loss is appreciable as only three diodes are in the conduction path when it is operating. However, the rectifier suffers from a high reverse-recovery loss. Many other boost type rectifier topologies were proposed to enhance the total rectifier efficiency, such as half bridge boost rectifier, full bridge rectifier and three level boost rectifier [2.6].

B. DC/DC converter topologies

The DC/DC converter is connected directly to the battery and it converts the DC voltage to desired battery recharging level. There are different methods for battery charging as shown in Table 2-2 [2.7]. The current-fed and voltage-fed bridge converter is one of the most common used topologies. Dual active bridges (DAB) topology with two full bridges on both sides of a high frequency transformer, as shown in Fig. 2.7, is also widely used [2.8].

Table 2-2. Battery Charging Methods [2.7]

Battery Charging Methods
Trickle Charge- Constant Current- Constant Voltage
Five step Charging Pattern
Pulse Charging Method
Boost Charging Method

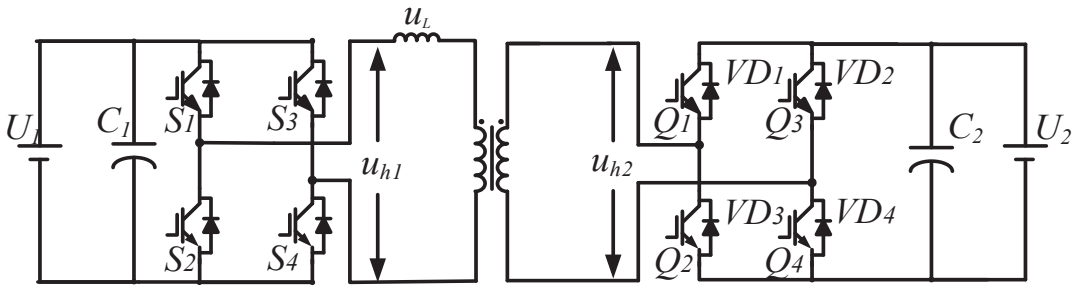

Fig. 2.7. Dual active bridge DC/DC converter.

C. Integrated Charger

For electric motor driven vehicle, the traction system is power electronics converter based propulsion structure. Both single and two stage chargers are independent of the powertrain system, which means that two converter systems are on EV. The integrated charger combines the charging system with the traction system by using traction converter as part of the charging circuit. This reduces the number of components required on board as well as the total weight and volume for both systems [2.9]. Although two systems share part of the components, they still operate independently as EVs are not moving when the conductive charging is in action.

2.1.3 Off Board Charger

For level 3 chargers, having on board high power charger might not be preferred choice as there are practical limitation for on board charging facilities in volume, weight and cost. Fig. 2.8 shows the general structure for level 3 fast chargers [2.10]. Galvanic isolation is required

for level 3 chargers, and there are two types of isolation topologies. One type has isolation at front end stage with a low frequency transformer and the other type has high frequency transformer at DC-DC stage. For the same power capability, the line transformer has bigger volume than the high frequency transformer. For commercial charging stations, which have high power ratio, using line transformer may take plenty of space. However, high frequency transformer type has higher cost on the high frequency DC-DC converter.

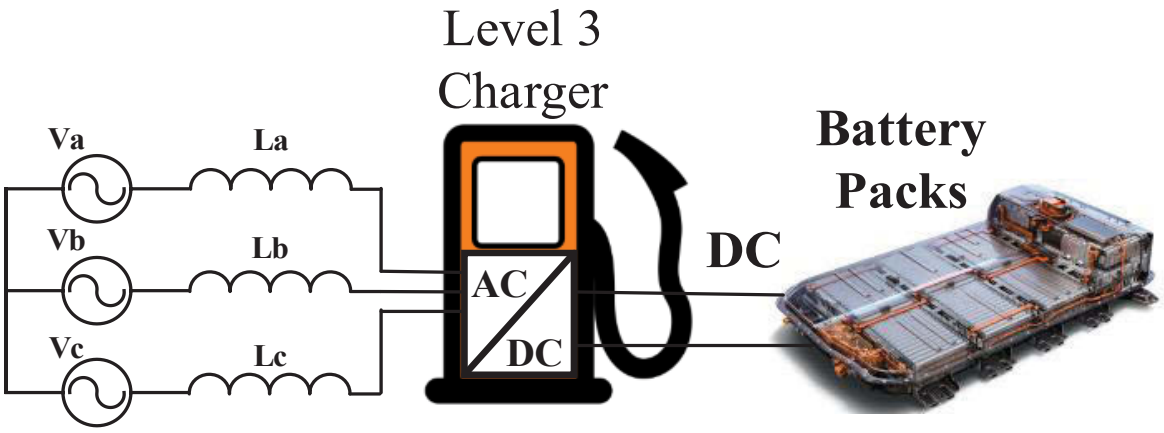

Fig. 2.8. General structure for Level 3 fast Charging.

The fast charging may affect the life time of the battery as abusive charging has negative effect in maintaining a long battery life.

2.2 Wireless Charging Methods

The conductive charging offers from low to high power charging solutions with or without on board power regulation devices. Level 1 and 2 chargers could be installed at home or

office parking spot, which gives EV more "refilling" opportunities than the ICE vehicles. However, it has not solved the "range anxiety" problem with current battery technology. The power ratio of the battery limits the charging speed, and therefore, fully recharging battery requires relatively long time. The level 3 fast charger could reduce the recharging time, but it is only available at limited commercial recharging stations and at a cost of reduction of battery life cycle.

Another option to release the "range anxiety" is to extend the recharging windows. When conductive charging is performed, EV needs to be connected to the grid with a cable wire manually. This limits the recharging windows to long time parking or recharging parking.

The idea of wireless charging is to transfer power to stationary or moving vehicles across an airgap without physical contact between the vehicle and the grid. A magnetic connection between the electric vehicle and the grid is employed instead of a connection by wire. The elimination of wire connection gives EV recharging move flexibility and will allow full automation and charging in motion. A magnetic recharging connection could be established and released in less than 1 s without manual operation, which gives an EV more potential charging windows. No physical contact between the EV and the grid means that the user is also isolated from the recharging grid system and therefore the relative hazards are reduced.

The following sections will review the state of art wireless charging technologies, including the pad geometries, compensation circuit, system control, etc.

2.2.1 EV Wireless Charging Technologies

Transferring power wirelessly across the space has been human's dream for a long time. In the early 20th century, Nikola Tesla devoted to a program to transfer large amount of power across continental distance wirelessly. He tried to bypass the electrical wire grid, but due to many technical and finance difficulties, he did not finish the project. Some other wireless power transfer technologies were developed, such as using laser and microwave to transfer power. Due to safety and efficiency reasons, these systems were not widely used in industry applications.

In recent years, more and more electric and electronic devices have been introduced to people's daily life, which makes the life more convenient. At the same time, recharging batteries have become a regular route in many people's living schedule; many devices such as mobile phone, iPad or even electric shaver have to be charged regularly. Although many signal lines have been removed due to the development of wireless signal transfer devices in the past 20 years, the absence of any charging wire still would bring uncomfortable experience to users. The using of wires is becoming a burden with the development of all kinds of electric and electronic devices.

The requirement for different types of wireless charging applications are not the same, for example, power, efficiency, distance comparing to receiver size.

For low power level electronics devices, such as the portable consumer electronics and implantable biomedical devices, the priority concern is the maximum power received by the devices. The wireless charging system should supply sufficient power to support devices or

recharging batteries within limited time. The transfer efficiency is supposed to be high which means minimising the size of the receiver. However, as long as enough power is transferred to the receiver side, the total efficiency of the charging system is not the major concern. There will not be significant increase in cost with lower system efficiency, which combines the power sources efficiency, transfer efficiency and battery charging efficiency.

At the same time, the size of power receivers in those devices is limited as there is no much space. The transfer distance is relatively long compared to the size of the receiver. Therefore, the major requirements for implantable devices are to supply sufficient power to devices, with smaller receiver size possible, across a relatively long distance comparing to the receiver size.

This is different from EV wireless charging application, where efficiency plays critical roles. The total efficiency takes charger power source efficiency, the transfer efficiency and on board charging efficiency. The required energy to fully recharge the EV is much higher than portable electronics, and if the total efficiency is low, the cost for recharging would be much higher. The Tesla sports car model S has 85 kWh on board battery storage system for maximum 426 km range [2.11]. For a family using Tesla Model S, with 20,000 km driving range per year, it requires at least 47 times fully charging. The average electricity price at New South Wales, Australia is 36.21 cents per kilowatt hour (c/kwh) for resident use according to the 2014 Residential Electricity Price Trends [2.12]. The recharging cost would be 1441.4 AUD per year. If the system efficiency is 20% lower, there would be an extra 360 AUD cost to recharge the car.

As conductive charging is mature with high efficiency, the wireless charging needs to have similar level efficiency to be competitive in the market. Therefore, for EV wireless charging, the goal is to transfer sufficient power with the highest system efficiency possible to the EV.

In order to solve the charging anxiety caused by the charging wires, the wireless charging technology has been put into the scope of the researchers. Many power transfer methods such as inductive power transfer and electromagnetic resonance transfer were developed in the past twenty years.

The research of wireless charging for EV could be catalogued into stationary wireless charging (SWC) and on-line/in motion/dynamic wireless charging as shown in Fig. 2.9. The stationary wireless charging systems charge EV when it stops or parks at certain positions. The primary and second sides for stationary charging start transferring power when they are both in a relatively small zone. Couplers based on inductive power transfer (IPT), magnetic resonance coupling transfer (MRCT) and permanent magnet coupling transfer (PMPT) technologies are designed for stationary wireless charging. The on-line/in motion charging systems charge EV while EV is running on the road. The primary side would be embedded under the road, and the on board second side pickup would capture the power.

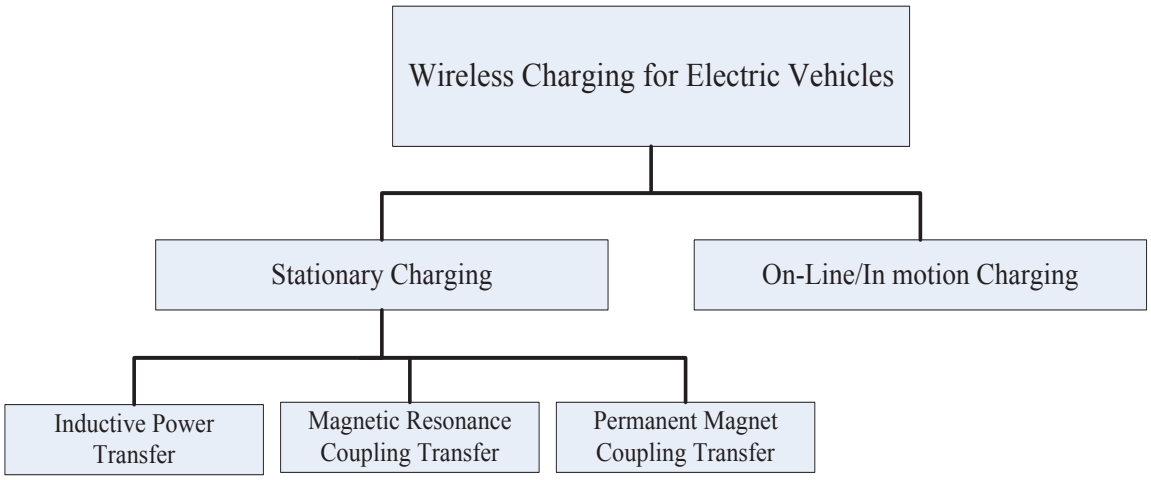

Fig. 2.9 Wireless charging technology

2.2.2 Magnetic Resonance Coupling Transfer

Electromagnetic resonant coupling technology is based on coupled mode theory and it was proposed in [2.13] as shown in Fig. 2.10. It is able to transfer the power to across a large air gap. The transfer efficiency of the device developed in [2.13] is approximately 90 % within 1 m. The coupler has two antennas which resonate at the same frequency. The concept of resonance is similar to the IPT with resonant windings; however, in this technique, the self-inductance of the antennas and the integrated capacitance form the resonance, and the frequencies are in MHz ranges.

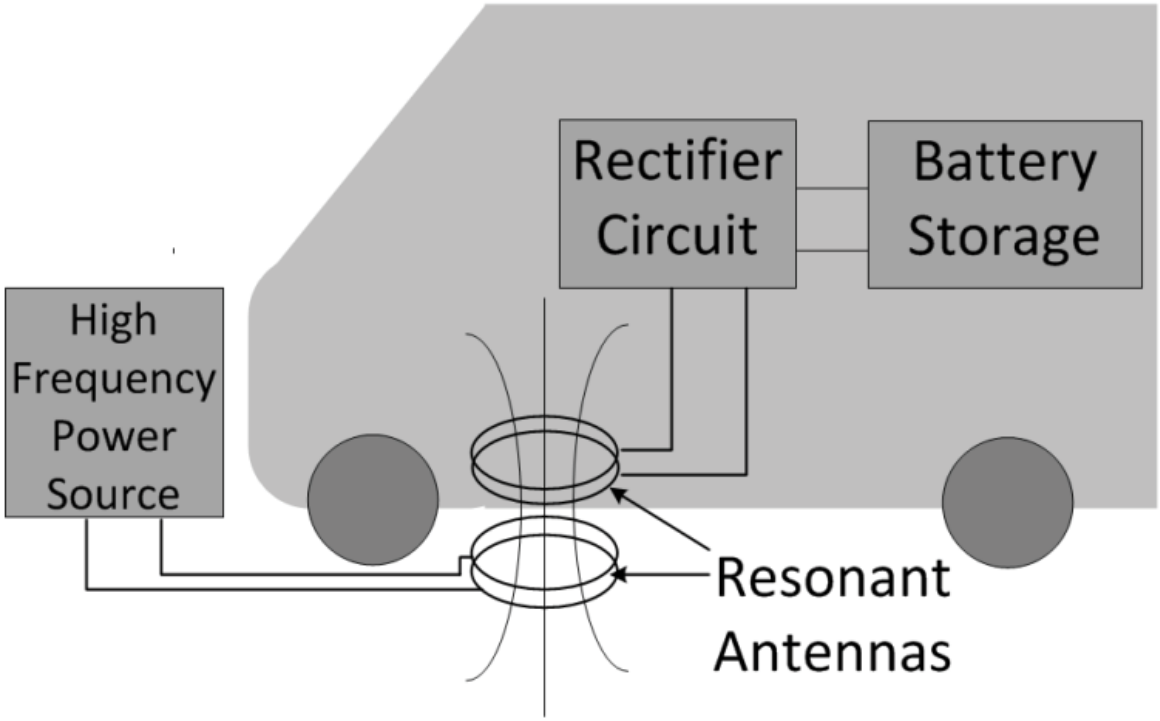

Fig. 2.10. MRCT EV charging system.

In [2.14], MRCT was proposed for EV wireless charging. Open- and short-end helical antennas were studied in [2.15]. Using magnetoplate wires [2.16] to improve the efficiency was also discussed. The limitation for this technique is the state-of-the-art semiconductor devices which have poor efficiency in MHz ranges. It should be borne in mind that the devices have to transmit high power.

2.2.3 Permanent Magnet Coupling

The permanent magnet coupling technique was developed by the University of British Columbia. It is based on the "magnetic gear effect". The magnetic gear is the coupler in this

technique [2.17-2.18]. The rotating permanently magnetized rotor on the primary side makes the secondary rotor rotate at the same speed. This is the synchronous speed.

The prototype in [2.19] allows the WPC system to transfer power across a 150 mm distance with efficiency of 81% at a relatively low frequency of 150 Hz. There may be issues with this system due to noise and vibration because it consists of several mechanical components. It may also have alignment and maintenance issues.

2.2.4 Inductive Charging Method

The inductive charging technique was introduced to road lighting applications, factory automation, biomedical implants and many other applications [2.20]. The power is transferred via a magnetic link with airgap between primary and secondary sides. For electrical vehicle wireless charging, the magnetic link is a loosely coupled transformer, as the separation between the bottom of vehicle and the ground for commercial vehicle is generally supposed to be over 15 cm.

In the following sections, the current state of the art inductive charging technologies in the design of wireless power charging couplers are reviewed.

2.3 Review of EV Inductive Charging Technology

The general structure of inductive power transfer (IPT) EV system is shown in Fig. 2.11. There are five major parts in the IPT EV charging, high frequency (HF) converter, compensation circuit, coupler, on board charging circuit, and the battery storage.

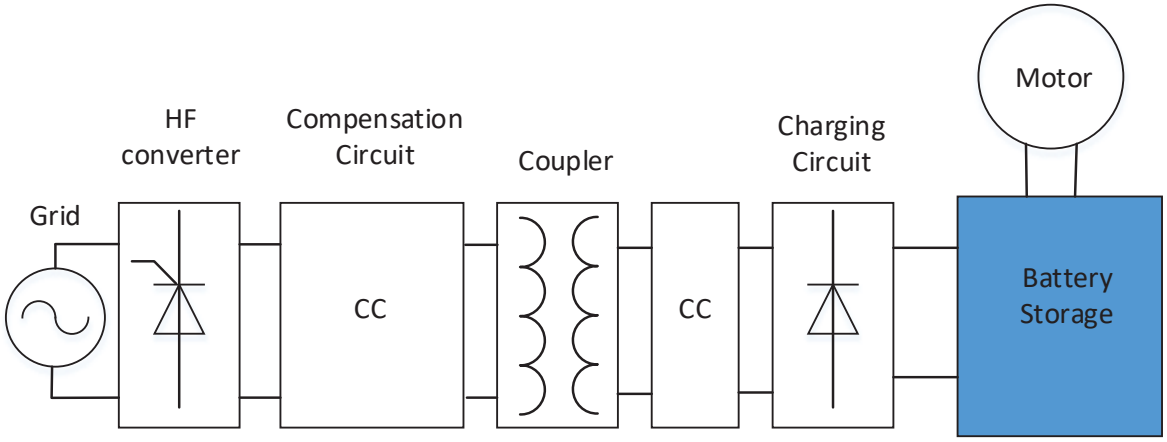

Fig. 2.11 General structure of the IPT system.

The power from the grid is transferred from the primary side to the secondary side of the coupler to charge the battery with a power converter on each side. The high frequency supply from the primary side converter is obtained from the utility power via a rectifier and converted to high frequency AC power with a PWM inverter, which may be a multilevel inverter. The secondary charging circuit then rectifies the high frequency AC power to DC to charge the on board battery. Since the secondary coupler is an on-board device, its size should be sufficiently small so that it can be embedded on the vehicle. Using high frequency to excite the coupler is necessary to reduce the size and weight of the coupler and also to allow for a low flux density since there is a large airgap. The compensation circuit is necessary as the high leakage inductance caused by the airgap between ground and vehicle limits the power transfer ability.

2.3.1 Coupler Power Source

In order to meet the requirement for commercial use of EV IPT system, the recharging cost should be within similar level to conductive charging. With high energy storage devices on board, the total efficiency of the charging system should be as high as possible, otherwise the recharging cost would be high and IPT would be less competitive in the market. Therefore, power source efficiency is critical for the EV IPT application.

The EV inductive power transfer system operating frequency is usually in the range of 10 kHz to 300 kHz [2.20]. It is possible for couplers to operate in higher frequency range with high transfer efficiency, but this frequency range is chosen based on the limitation of power source. High frequency power sources with high internal resistance have high power loss in the power source which is against the high efficiency principle for high power applications. The power electronics based inverter which has low internal resistance is the proper candidate for the EV IPT application.

Currently, the most commonly used topology is the full bridge inverter. A typical bidirectional IPT system using full bridge inverter is shown in Fig. 2.12. The phase shift control is implemented for controlling the output power of the full bridge. Other PWM modulation methods which are well developed in solid state transformer are not widely implemented in IPT application because of the limitation of the power electronics switching frequency.

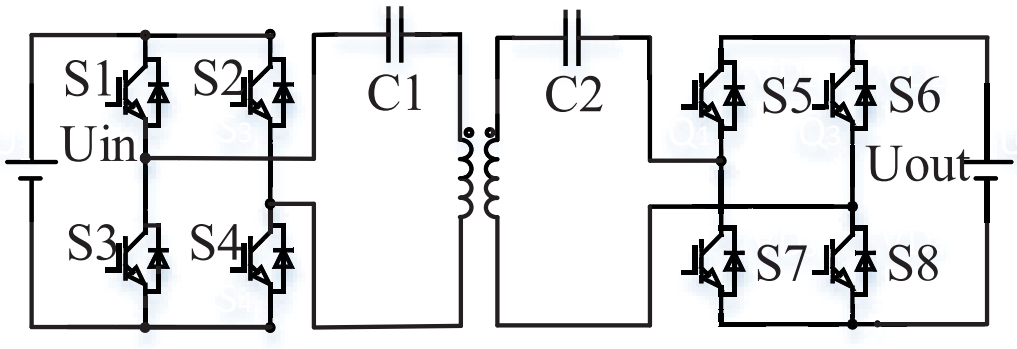

Fig. 2.12 Full bridge inverter.

The primary and secondary sides locations are separated in wireless charging. And there are several control methods based on this characteristic, such as primary side control [2.22-2.25], secondary side control [2.26-2.28] and dual sides control [2.29]. The primary and dual controls are suitable for steady charging scenario in most of the projects, where there is one primary pad/track, and a fixed number of pickups on the secondary sides. The secondary side control is designed for multiple pickup secondary pads receiving power from one pad.

The active front end for power factor correction is necessary for application with large variation in distance or misalignment [2.29]. The power factor would be compensated for the grid.

With the development of the GaN and SiC power electronics devices, which have high turn on/off speed, it has the potential to implement those modulation methods to reach faster dynamic response in the future.

2.3.2 Compensation

The distance between the primary and secondary sides should be relatively large to give some ground clearance for the vehicle, as already discussed. The airgap between the primary and secondary sides leads to weak coupling between windings. The magnetic coupling coefficient *k* gives a measure to how close the coupling is between the primary and secondary sides. This is defined by

$$k = \frac{M}{\sqrt{L_1 L_2}} \tag{2.1}$$

where M is the mutual inductance between the two sides of the coupler, and L1 and L2 are the self-inductances of the primary and secondary coils. In order to transfer more power, k should be as high as possible. Hence the coil and core designs are very important in order to achieve a high coupling coefficient.

In [2.26], the researchers state that compensation is more effectively realised by the addition of capacitance in series or parallel with both sides of the transformer, which is an improvement over the use of soft switching techniques. This will support the output voltage and compensation on primary side is required to minimize the VA rating of the inverter. The secondary side compensation is used to help the power transfer ability since the voltage is boosted.

There are four basic structures: series-series (SS), series-parallel (SP), Parallel-Parallel (PP), and Parallel-Series (PS), as shown in Fig. 2.13. The capacitors on both sides form resonant circuits with the inductances of the transformer so that reactive power is not

transferred across the air-gap since reactive power is supplied from both sides. This reduces copper loss and iron loss in the coupler as well as switching losses and the VA rating of the power electronic converters.

Normally, the primary and secondary resonant frequencies are tuned in the same way as given by

$$\omega = \frac{1}{\sqrt{L_s C_s}} = \frac{1}{\sqrt{L_p C_p}} \tag{2.2}$$

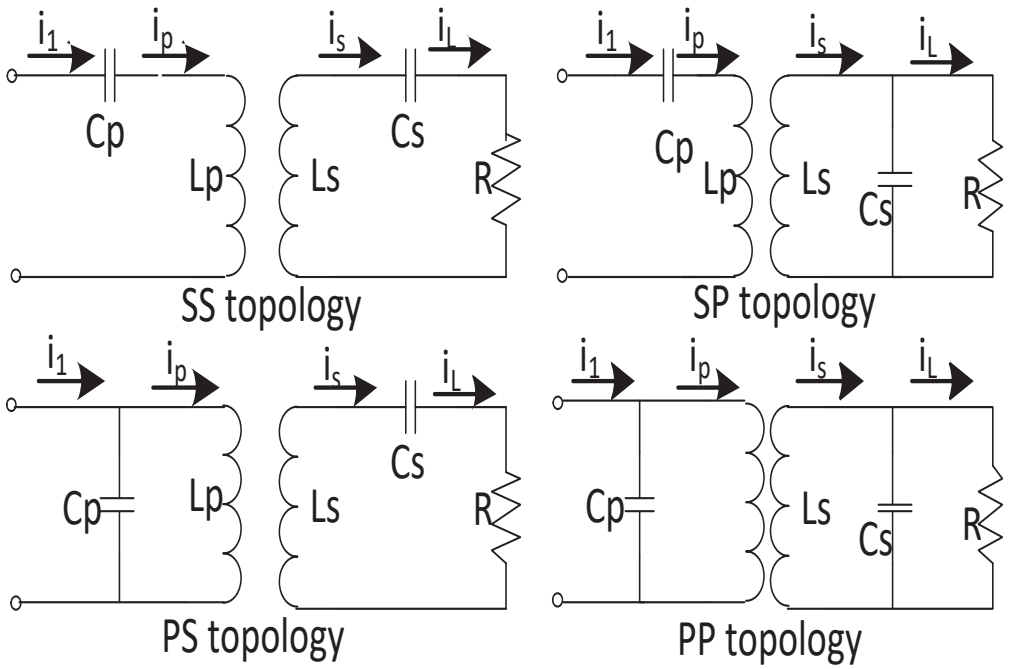

Fig. 2.13. Basic compensation topology.

LCL compensation circuit is used in [2.30-2.32] to reach current source performance. LCLC is introduced to cancel the nonlinear effect of the rectifier diode, and reach unity

power factor as certain load condition [2.33-2.34].

2.3.3 Stationary Wireless Charging Coupler

As already stated, stationary wireless charging takes place when the EV is parked such as in a car park, garage or when the vehicle is stationary for a short time which could possibly be at road junctions or even at future recharging stations. Obviously for charging over a short period then it is necessary to have batteries or energy storage units (such as super- or ultra-capacitors) that can store energy rapidly and efficiently. An SWC could be fully automatic since hard-wire connection is eliminated by the wireless connection between couplers. This means that EV could take every possible opportunity to charge the battery even when it is only a short stop. The primary side would need to be embedded under the ground, and the secondary side needs to be underneath the EV to reduce the electromagnetic leakage and interference with other vehicles and objects. One of the main issues is clearance and air-gap.

Inductive charging method has a magnetic link between the primary and secondary sides. In EV inductive charging technology, there might be cores in primary and secondary sides, but there is no core which goes through both primary and secondary at the same time. The conductive charging with isolation transformer is not considered as inductive charging in EV charging technology.

The couplers of IPT chargers are loosely coupled transformers in which there is no core that links the primary and secondary coils. Therefore, the coupler has to transfer the power across the air-gap. An early stationary IPT system for EV [2.35] and one with compensation in [2.23] and [2.26] are shown in Fig. 2.14. As can be seen, the only basic difference is the

tuning capacitor across the primary and secondary. The primary and secondary sides of IPT stationary couplers are generally designed as pads.

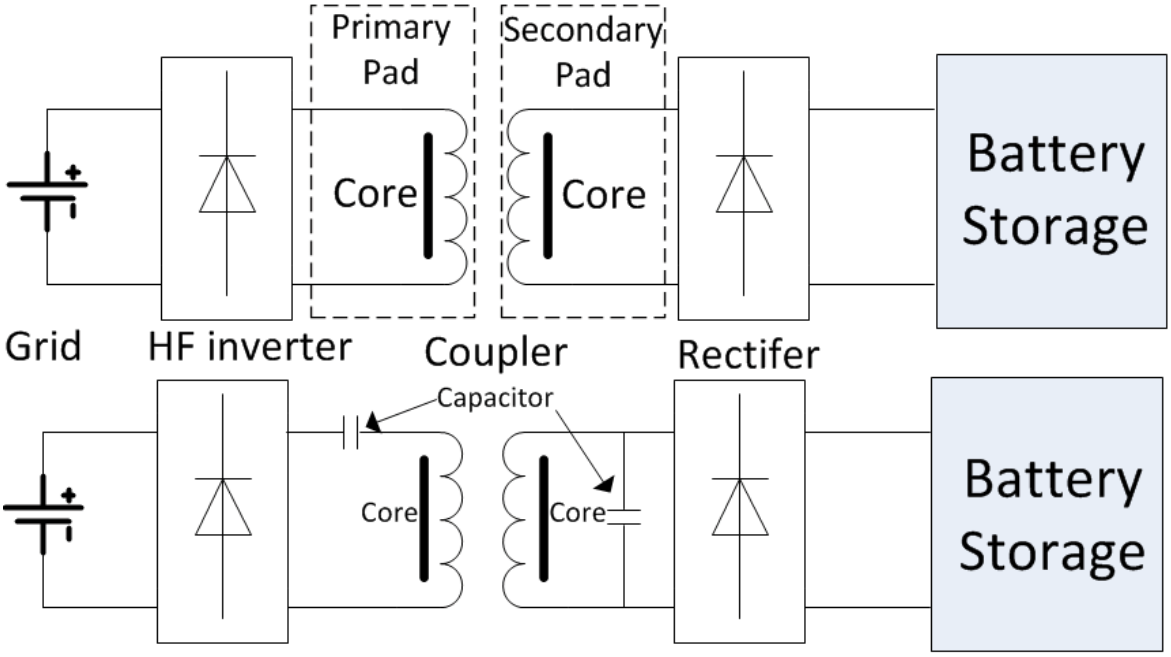

Fig. 2.14. IPT system: a) early IPT charging system, b) IPT charging system with compensation.

It has already highlighted that for EV applications, the EV IPT system is a loosely coupled IPT system. In order to transfer more power, *k* should be as high as possible. Hence the coil and core design are very important in order to achieve a high coupling coefficient.

Many core shapes have been developed. From [2.36-2.38], the pot core coupler style is used. In [2.38] and [2.39-2.41], ferrite plates are used for the coupler core. In [2.38], a 3 mm air-gap core is used where a 100 kHz and 97% efficiency system is realized. In [2.42], and a U-shape core is used.

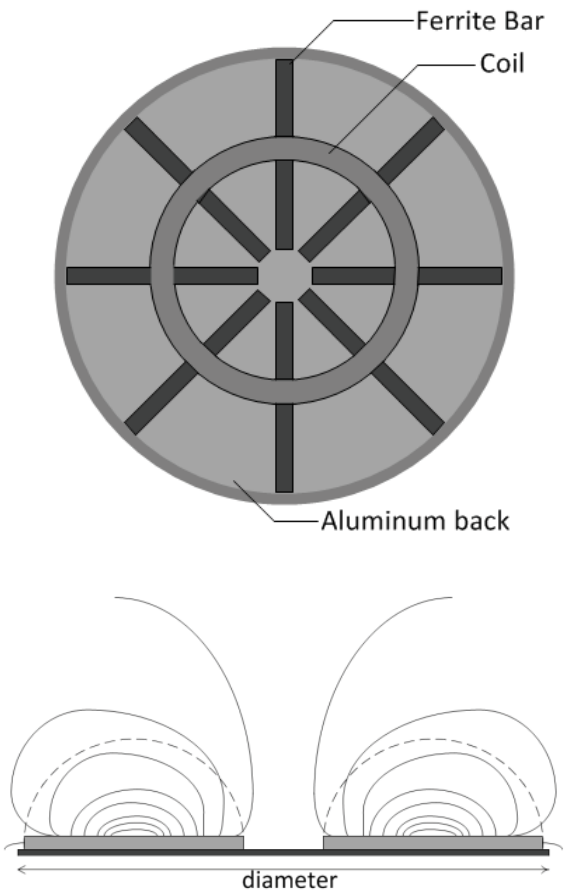

Fig. 2.15. Flux of circular pad.

In [2.43] and [2.44], a circular pad structure is utilized. Ferrite bars are used to form a circular structure and replace the solid ferrite discs as shown in Fig. 2.15. The weight of the coupler was then reduced while a coupling factor 0.15 was achieved with a 200 mm air-gap and 700 mm diameter circular pads. The authors discussed the relationship between the coupling coefficient, the amount of ferrite and the space between the strips. They simulated the structure with finite element analysis (FEA). It found that larger pads are required for greater power transfer and improved horizontal tolerance.

Similar circular pads were used in [2.25]. These were inserted in concrete and the losses were investigated. Rectangular coils with back ferrite core pads were also designed and simulated with FEA and a comparison made.

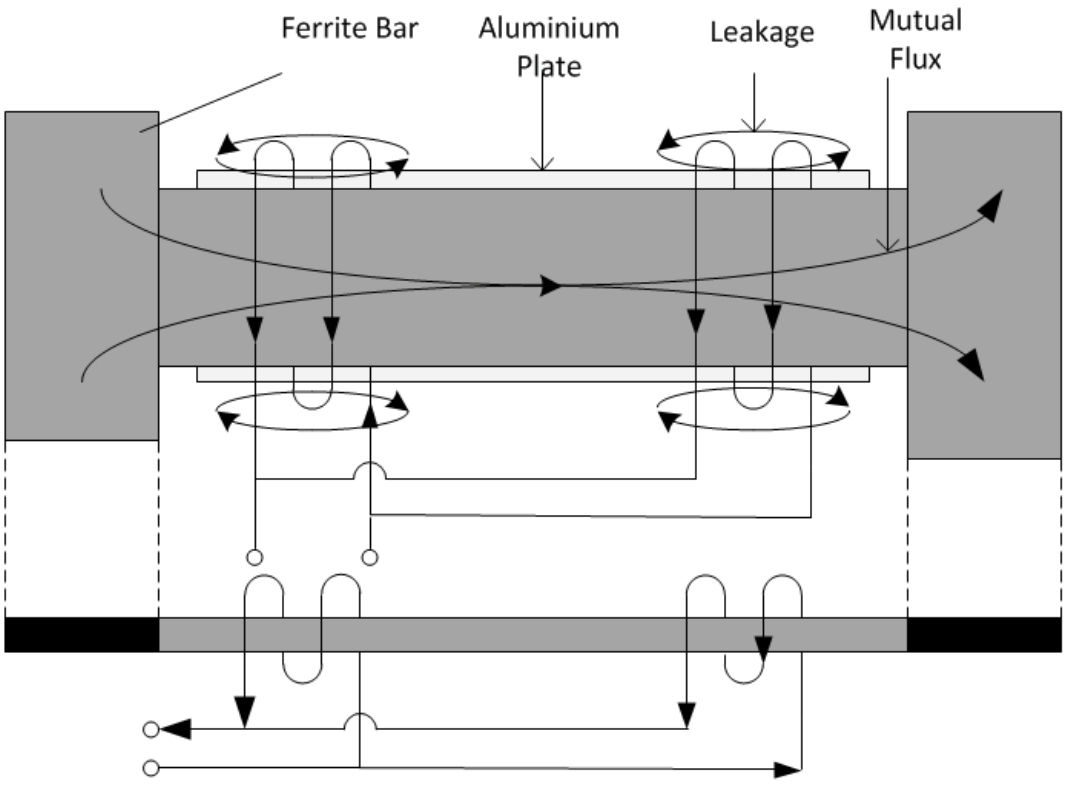

Fig. 2.16. Top view and cross view of a flux pipe pad.

Reference [2.45] explains the concept of fundamental flux path height, which is roughly one quarter of the diameter of the circular pads as shown in Fig. 2.15. This paper also designs flux pipe pads, as illustrated in Fig. 2.16. These enhance the fundamental flux path heights. The flux pipe has two coils wound around both ends of the middle ferrite strips. This coupler creates higher flux paths than the circular pad, and achieves a coupling factor of 0.2 at 200

mm. It is 4 mm thicker than the circular coupler for the reason that coils are wound around the core.

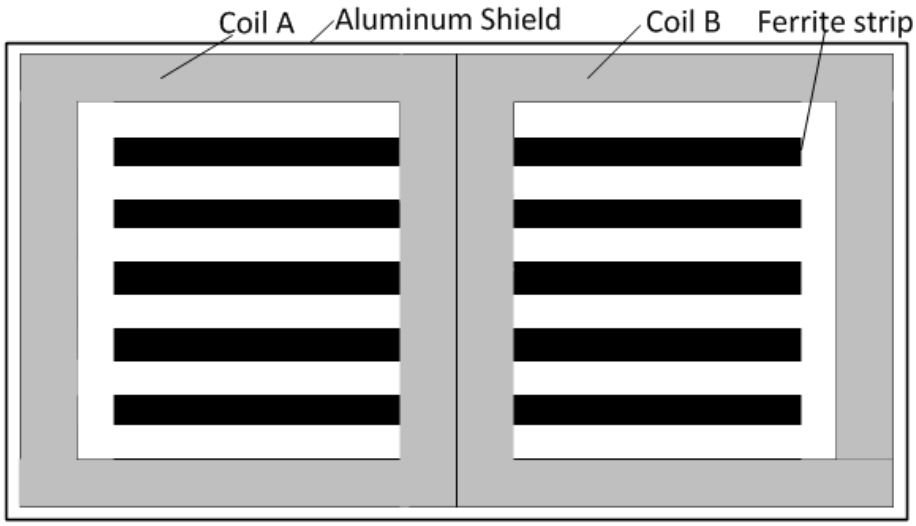

(a)

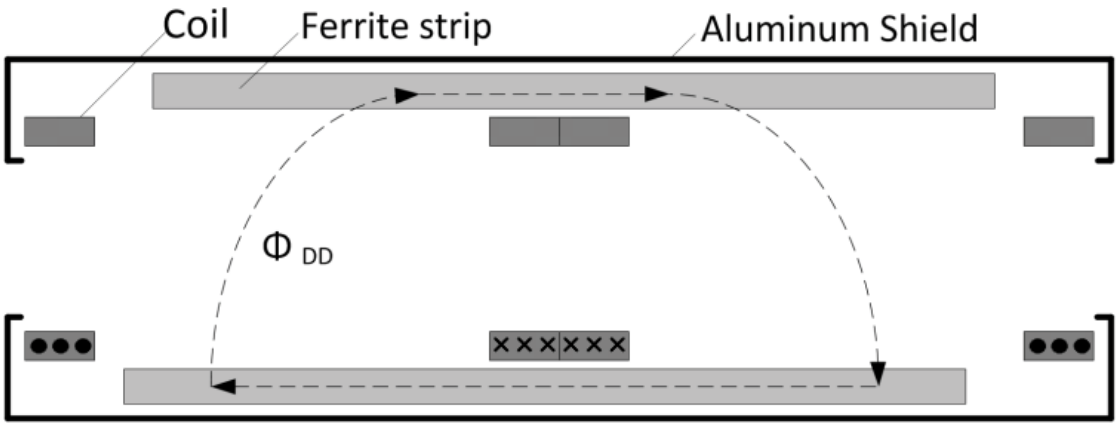

(b)

Fig. 2.17. Structure of DD pad: (a) top view (b) cross view.

In [2.46] and [2.47], polarized "DD" pads where developed. These are illustrated in Fig. 2.17. The topology of the DD pad is similar to that of flux pipe. The coils lie on the ferrite strips rather than wound around the strips. This change makes the flux leave from the top of the coils instead of from ends of strips for which the aluminium back plate can be employed to reduce the leakage flux from back and sides. While aluminium is not magnet, the eddy currents will suppress flux leakage.

In [2.48], MnZn material 6H40 was suggested to be used for high frequency EV IPT application. The MnZn material was selected for the core material for its high flux saturation and low power loss when operating below 100 kHz. In [2.44], EPCOS N87 MnZn material was selected for the core material and in [2.25], Spectrum Magnetics MnZn ferrite plates were selected.

2.3.4 On-Line/In-Motion Charging

Substantial on-board battery capacity is required because the vehicle needs continuous power for traction drive and also the amount of power required may be high for reasonable acceleration. A limited battery reserve may not be able to deliver this power in an efficient manner. A roadway charging system would charge the moving EV dynamically, minimizing battery storage required. The power may be delivered directly to the drive which would increase efficiency. This is not a radical solution – on-line over-head wire power delivery was used to supply trolley buses several decades ago and in some cities they are still used. For wireless supply, the couplers use a lumped pad structure [2.19] and distributed power lines [2.49] as the primary side.

Lumped on-road charging has a series of pads which are similar to the stationary charging pads to form a power track along road lanes. A possible lumped on-road charging topology is shown in Fig. 2.18 [2.19]. As the vehicle moves over the pads, a continuous magnetic field is formed with the powered pads. The secondary pickup couples with the magnetic field which induces emfs and generates current so that power crosses the air-gap. A position detection technique is required to turn on and turn off the pads, otherwise there will be substantial and unnecessary losses in the primary coils that are excited but not coupled.

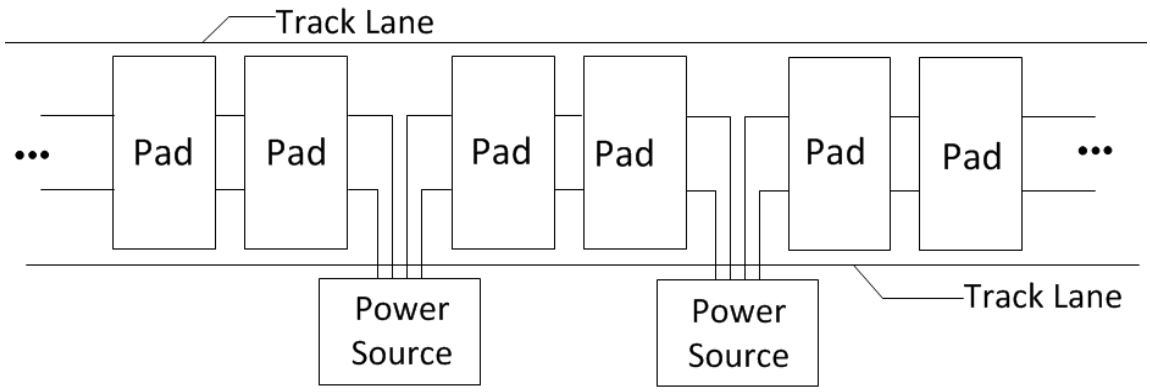

Fig. 2.18. A possible lumped on road charging.

Circular pads are not suitable for dynamic charging, because they have a null in their power profiles when horizontally offset by 38 % of the pad diameter [2.44,2.50]. The pads in [2.25] to [2.46] have good performance on their normal direction of the track. A three phase system was proposed in [2.51], as shown in Fig. 2.19. The wires lie on the strips and form a magnetic field.

Research on on-line electric vehicle (OLEV) charging has been conducted at the Korea Advanced Institute of Science and Technology (KAIST) for some time and they have developed several distributed power line and pickup coil systems [2.49] [2.52-2.57]. The E-core and U-core primary sides are used in their first and second generations. In the third generation, a fish bone structure is used for the underground core. The parameters of the three generations are shown in Table 2-3.

Table 2-3 General Parameters for Three Generations of On-Line EV Charging

	1G	**2G**	**3G**
Air gap	10 mm	170 mm	170 mm
Efficiency	80 %	72 %	71 %
Unit power	3 KW	6 KW	17 KW
Weight	10 Kg	80 Kg	110 Kg

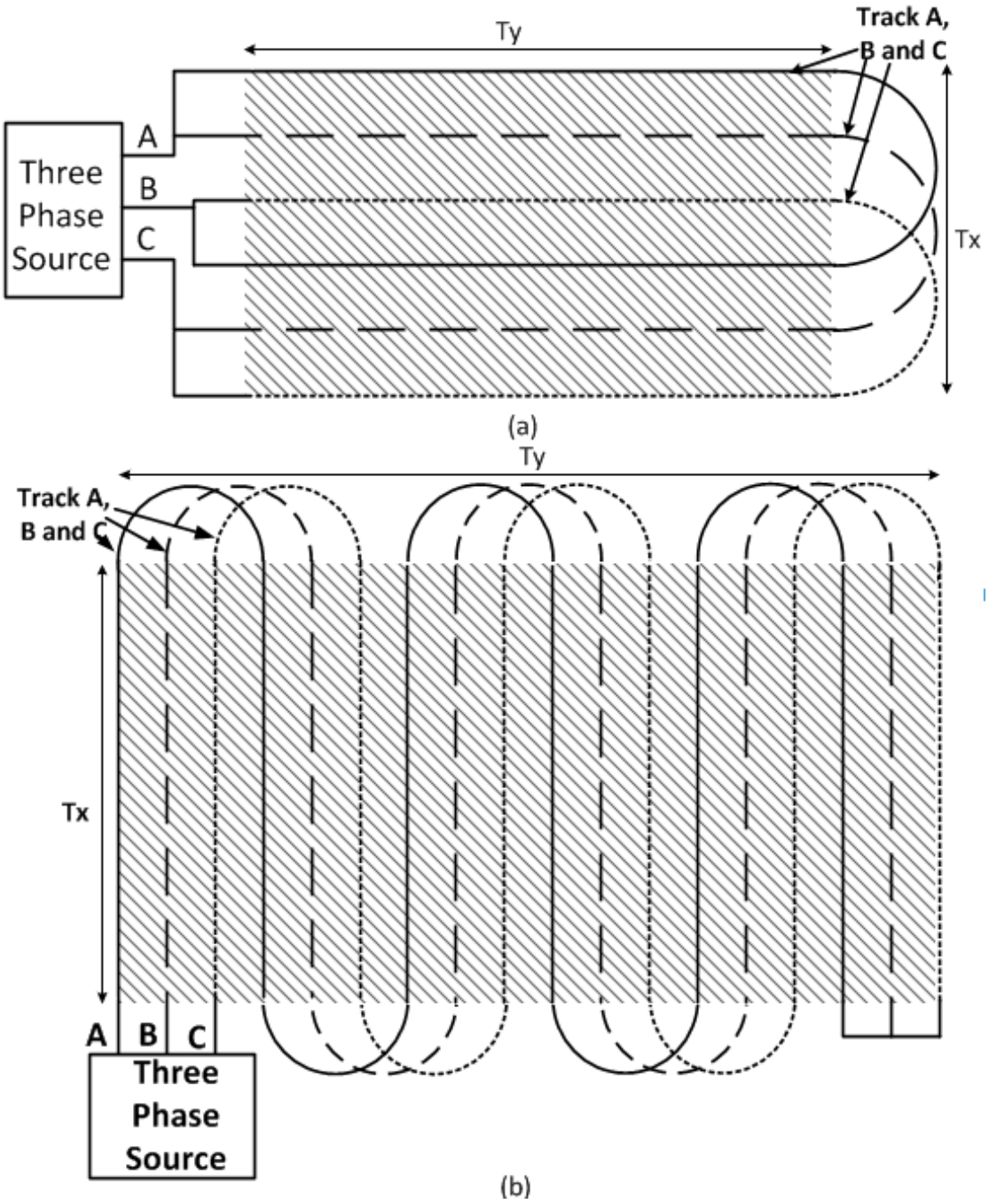

Fig. 2.19. Three phase track topologies: (a) bipolar and (b) unipolar.

In [2.55], a dual type and mono type of power transfer couplers were designed and these are illustrated in Fig. 2.20. The duel type has two opposite power lines and it enables a large amount of power transfer due to the better coupling coefficient when compared to mono type. However, the mono type has a better misalignment tolerance.

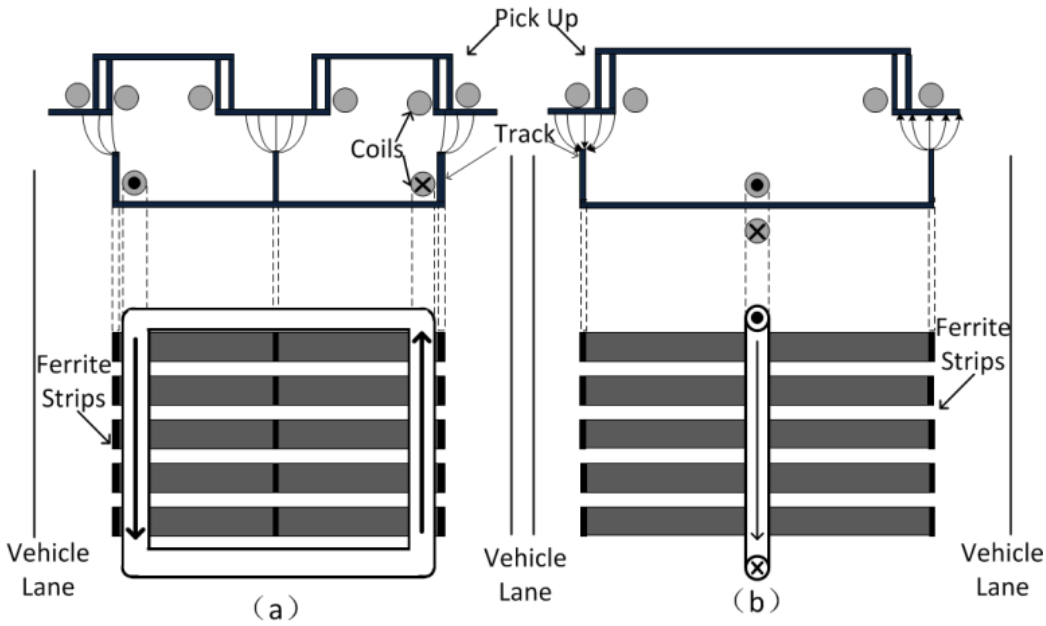

Fig. 2.20. The top view and cross view of OLEV power transfer system: (a) dual type and (b) mono type.

2.3.5 Discussion

There are other technologies such as acoustic energy transfer [2.58] and capacitive power transfer [2.59-2.62] which have been proposed; however, due to their limited efficiency and power, they are currently not used in the EV wireless charging. The current research of EV wireless charging involves a range of relative topics not only including the coupler optimization but also the control for the power electronics devices, system control for power

flow and battery charging, etc. And in-motion charging could be a new development in energy management and optimization of an EV. In [2.63], the effect of range extension by on-road charging was studied. Both the effects of stationary charging and on-line charging are simulated under several standard driving conditions. Stationary charging was tested for the urban driving condition where there are many stop/start points due to traffic lights. Stationary charging systems can be located under the road near traffic lights, and the results show that a 20 kW wireless charging system would increase the range by 172% under the Urban Dynamometer Driving Schedule and 311% under the European Standard ECE-EUDC combined urban test cycle. With a 30 kW system, the state of charge (SOC) of the battery remains approximately the same after driving through. For in-motion charging, with a 30 kW charging system with a highway cover of 40%, the SOC of battery is almost constant throughout the journey. In [2.64], the authors derived a model for the mutual inductance between the coils in an IPT system, which would save the computing time of FEA software. The stability and performance of a wireless charging system should be robust, and the control of the system is also very important. In [2.65], the author pointed out that the inductive coupled transfer system is a typical high-order and complex non-linear system. Using the Generalized State-Space Averaging (GSSA) method, the IPT system was approximated to a linear system and a μ-controller was proposed for the system. The bidirectional power flow control method for EV IPT systems was studied in [2.66-2.69]. Safety is always a very important concern for wireless charging; the charging system has to meet the electromagnetic field exposure standards set by the International Committee on Electromagnetic Safety (ICES) in the USA, the International Commission on Non-Ionizing Radiation Protection (ICNIRP) in Europe and the Australian Radiation Protection and

Nuclear Safety Agency in Australia. In [2.25,2.44,2.45], Auckland University published studies which used an aluminium backing plate and a ring as a shield against stray magnetic fields. In [2.69], in addition to passive shielding using a metallic plate, a reactive shielding using a resonant current loop was employed.

In system modelling, the accuracy of coupler parameters is critical. This thesis introduces a numerical and analytical combined method to analyse the AC resistance of the coupler. The thesis also propose a coupler with assistive coils. Those are the major contribution of this thesis.

In order to define the minimum performance under acceptable criteria, the SAE standard J2954 was started in 2010. The last version was released in May 2016. Many auto OEMs and Bus OEMs including BMW, Ford and Toyota etc, as well as other organizations： Argonne Natíonal Laboratory, TÜV North America, University of Tennessee and etc. Three type of charging were explored: residential, on-road static and on-road dynamic. There are also four power classes for wireless charger, which are WPT1, WPT2, WPT3 and WPT4. The minimum target efficiency for first three classes should be over 85% and minimum target efficiency at offset position should be over 80%. The suggested efficiency for WPT4 is still to be determined. The J2954 system frequency is 85kHz, and for compensation tuning, the frequency should in range of 81.38kHz to 90kHz.

2.4 Summary

In this chapter, the high frequency power source, compensation circuit, and the coupler geometry are reviewed. In order to achieve high system efficiency, the power electronics based inverter is widely used for EV IPT system. To enhance the power transfer capability, the compensation circuit is essential. The compensation in the secondary side aids the power transfer, and the primary side compensation reduces the VA rating of the power electronics. The stationary couplers have different performance yet there is no certain geometry which has the best performance over the rest. The dynamic charging has track and pad types of primary windings. The received power is relatively stable when the vehicle is moving along the track type primary. The pad type does not need to energies long track therefore it has the potential to reduce the loss in primary when powering the vehicle.

2.5 References

[2.1] M. Yilmaz and P. T. Krein, "Review of battery charger topologies, charging power levels, and infrastructure for plug-in electric and hybrid vehicles", IEEE Trans. Power Electron., vol. 28, no. 5, pp. 2151-2169, 2013

[2.2] N. Wong and M. Kazerani, "A review of bidirectional on-board charger topologies for plugin vehicles", presented at the 25th Can. Conf. Elect. Comput. Eng., pp. 1-6, 2012

[2.3] B. Singh, B. N. Singh, A. Chandra, K. Al-Hadad, A. Pandey, and D. Kothari, "A review of single-phase improved power quality AC-DC converters", IEEE Trans. Ind. Electron., vol. 50, no. 5, pp. 962-981, 2003

[2.4] S.N. Vaishnav and H. Krishnaswami, "Single-stage isolated bi-directional converter topology using high frequency AC link for charging and V2G applications of PHEV," 2011 IEEE, VPPC, Sep 2011, pp. 1-4.

[2.5] J. P. M. Figuerido , F. L. Tofili and B. L. A. Silva, "A review of single-phase PFC topologies based on the boost converter", Proc. IEEE Int. Conf. Ind. Appl., pp. 1-6, 2010

[2.6] A. Khaligh and S. Dusmez, "Comprehensive topological analysis of conductive and inductive charging solutions for plug-in electric vehicles", IEEE Trans. Veh. Technol., vol. 61, no. 8, pp. 3475-3489, 2012

[2.7] E. Ayoub and N. Karami, "Review on the charging techniques of a Li-Ion battery," 2015 TAEECE, 2015, pp. 50-55.

[2.8] Y. Du , S. Lukic , B. Jacobson and A. Huang, "Review of high power isolated bi-directional DC-DC converters for PHEV/EV DC charging infrastructure", Proc. IEEE ECCE., pp. 553-560, 2011

[2.9] Y. Lee , A. Khaligh and A. Emadi, "Advanced integrated bidirectional AC/DC and DC/DC converter for plug-in hybrid electric vehicles ", IEEE Trans. Veh. Technol., vol. 58, no. 8, pp. 3970-3980, 2009

[2.10] S. Dusmez , A. Cook and A. Khaligh, "Comprehensive analysis of high quality power converters for level 3 off-board chargers", Proc. IEEE Veh. Power Propulsion Conf., pp. 1-10, 2011

[2.11] "Annual report on form 10-K for the year ending December 31, 2012, Tesla Motors INC." Available: http://ir.tesla.com/secfiling.cfm?filingid=1193125-13-96241&cik

[2.12] "2014 Residential Electricity Price Trends, Australia." Available: www.aemc.gov.au/Markets-Reviews.../2014-Residential-Electricity-Price-Trends

[2.13] A. Kurs, A. Karalis, R. Moffatt, J. D. Joannopoulos, P. Fisher, and M. Soljačić, "Wireless Power Transfer via Strongly Coupled Magnetic Resonances," Science, vol. 317, pp. 83-86, 2007-07-06 00:00:00 2007.

[2.14] T. Imura , H. Okabe and Y. Hori, "Basic experimental study on helical antennas of wireless power transfer for electric vehicles by using magnetic resonant couplings", Proc. IEEE Vehicle Power Propulsion Conf., pp. 936-940, 2009

[2.15] T. Imura , H. Okabe , T. Uchida and Y. Hori, "Study on open and short end helical antennas with capacitor in series of wireless power transfer using magnetic resonant couplings", Proc. IEEE Ind. Electron. Soc. Annu. Conf., pp. 3884-3889, 2009

[2.16] T. Mizuno , S. Yachi , A. Kamiya and D. Yamamoto, "Improvement in efficiency of wireless power transfer of magnetic resonant coupling using magnetoplated wire", IEEE Trans. Magn., vol. 47, no. 10, pp. 4445-4448, 2011

[2.17] W. Li, " High efficiency wireless power transmission at low frequency using permanent magnet coupling," M.S. thesis, Sci. Dept., BC. Univ, Vancouver., BC, 2009.

[2.18] L. A. Whitehead, "Systems and methods for dipole enhanced inductive power transfer," US 13/203,404, Dec 15, 2011.

[2.19] J. T. B. G. A. Covic, M. Budhia, and C.-Y. Huang, "Electric Vehicles-Personal transportation for the future," Proc. World Battery, Hybrid Fuel Cell Elect. Veh. Symp. Exhibi., Shenzhen, China, 2010.

[2.20] A. W. Green and J. T. Boys, "10 kHz inductively coupled power transfer concept and control", IEE Proc. Power Electron. Variable-Speed Drives, pp. 694-699, 1994

[2.21] S. Y. R. Hui, W. Zhong and C. K. Lee, "A critical review of recent progress in mid-range wireless power transfer", IEEE Trans. Power Electron., vol. 29, no. 9, pp. 4500-4511, 2014

[2.22] H. L. Li, A. P. Hu, G. A. Covic and T. Chunsen, "A new primary power regulation method for contactless power transfer", Proc. IEEE ICIT, pp. 1-5

[2.23] Y. H. Chao, J. J. Shieh, C.-T. Pan, W.-C. Shen and M.-P. Chen, "A primary-side control strategy for series-parallel loosely coupled inductive power transfer systems", Proc. IEEE Conf. Ind. Electron. Appl., pp. 2322-2327, 2007

[2.24] J. Miller, O. Onar and M. Chinthavali, "Primary-side power flow control of wireless power transfer for electric vehicle charging", IEEE J. Emerg. Sel. Topics Power Electron., vol. 3, no. 1, pp. 147-162, 2015

[2.25] J. M. Miller, C. P. White, O. C. Onar and P. M. Ryan, "Grid side regulation of wireless power charging of plug-in electric vehicles", Proc. IEEE ECCE, pp. 261-268

[2.26] W. Chwei-Sen, O. H. Stielau, and G. A. Covic, "Design considerations for a contactless electric vehicle battery charger," IEEE Trans. Power Electron, vol. 52, pp. 1308-1314, 2005.

[2.27] J. T. Boys, C. I. Chen and G. A. Covic, "Controlling inrush currents in inductively coupled power systems", Proc. 7th IPEC, vol. 2, pp. 1046-1051

[2.28] J. U. W. Hsu, A. P. Hu, and A. Swain, "A wireless power pickup based on Directional tuning control of magnetic amplifier," IEEE Trans Ind. Electron, vol. 56, pp. 2771-2781, 2009.

[2.29] T. Diekhans and R. W. D. Doncker, "A dual-side controlled inductive power transfer system optimized for large coupling factor variations and partial load," IEEE Trans on Power Electron, vol. 30, pp. 6320-6328, 2015.

[2.30] C. S. Tang, Y. Sun, Y. G. Su, S. K. Nguang, and A. P. Hu, "Determining multiple steady-state ZCS operating points of a switch-mode contactless power transfer system," IEEE Trans on Power Electron, vol. 24, pp. 416-425, 2009.

[2.31] B. Sharp and H. Wu, "Asymmetrical Voltage-Cancellation control for LCL resonant converters in Inductive Power Transfer systems," IEEE APEC, 2012, pp. 661-666.

[2.32] C. Y. Huang, J. T. Boys, and G. A. Covic, "LCL Pickup Circulating Current Controller for Inductive Power Transfer Systems," IEEE Trans on Power Electron, vol. 28, pp. 2081-2093, 2013.

[2.33] N. A. Keeling, G. A. Covic, and J. T. Boys, "A Unity-Power-Factor IPT Pickup for High-Power Applications," IEEE Trans. on Ind. Electron, vol. 57, pp. 744-751, 2010.

[2.34] N. Keeling, G. A. Covic, F. Hao, L. George, and J. T. Boys, "Variable tuning in LCL compensated contactless power transfer pickups," IEEE ECCE, 2009, pp. 1826-1832.

[2.35] K. W. Klontz , A. Esser , R. R. Bacon , D. M. Divan , D. W. Novotny and R. D. Lorenz, "An electric vehicle charging system with ‘universal’ inductive interface ", Proc. Power Conv. Conf., pp. 227-232, 1993

[2.36] R. Laouamer , M. Brunello , J. P. Ferrieux , O. Normand and N. Buchheit, "A multi-resonant converter for non-contact charging with electromagnetic coupling", Proc. 23rd Int. Conf. Ind. Electron. Control Instrum., vol. 2, pp. 792-797, 1997

[2.37] S. Valtchev , B. Borges , K. Brandisky and J. B. Klaassens, "Resonant contactless energy transfer with improved efficiency", IEEE Trans. Power Electron., vol. 24, no. 3, pp. 685-699, 2009

[2.38] H. Sakamoto, K. Harada, S. Washimiya, K. Takehara, Y. Matsuo, and F. Nakao, "Large air-gap coupler for inductive charger [for electric vehicles]," IEEE Trans Magn, vol. 35, pp. 3526-3528, 1999.

[2.39] F. Nakao, Y. Matsuo, M. Kitaoka and H. Sakamoto, "Ferrite core couplers for inductive chargers",Proc. Power Conv. Conf., vol. 2, pp. 850-854, 2002

[2.40] X. Liu and S. Y. Hui, "Optimal design of a hybrid winding structure for planar contactless battery charging platform," IEEE Trans on Power Electron, vol. 23, pp. 455-463, 2008.

[2.41] M. Dockhorn , D. Kurschner and R. Mecke, "Contactless power transmission with new secondary converter topology",Proc. 13th Power Electron. Motion Control Conf., pp. 1734-1739, 200

[2.42] K. Chang-Gyun, S. Dong-Hyun, Y. Jung-Sik, P. Jong-Hu, and B. H. Cho, "Design of a contactless battery charger for cellular phone," IEEE Trans. on Ind. Electron., vol. 48, pp. 1238-1247, 2001.

[2.43] M. Budhia, G. A. Covic and J. T. Boys, "Design and optimisation of magnetic structures for lumped inductive power transfer systems ", IEEE Trans. Power Electron., vol. 26, no. 11, pp. 3096-3108, 2011

[2.44] M. Budhia, G. A. Covic, and J. T. Boys, "Design and optimization of circular magnetic structures for lumped inductive power transfer systems," IEEE Trans. Power Electron., vol. 26, pp. 3096-3108, 2011.

[2.45] M. Budhia, G. Covic and J. Boys, "A new IPT magnetic coupler for electric vehicle charging systems",Proc. Ind. Electron. Conf., pp. 2487-2492, 2010

[2.46] M. Budhia , G. A. Covic , J. T. Boys and C. Y. Huang, "Development and evaluation of single sided flux couplers for contactless electric vehicle charging", Proc. IEEE Energy Conversion Congr. Expo., pp. 614-621, 2011

[2.47] M. Budhia, J. T. Boys, G. A. Covic, and C. Y. Huang, "Development of a single-sided flux magnetic coupler for electric vehicle IPT charging systems," IEEE Trans.Ind. Electron., vol. 60, pp. 318-328, 2013.

[2.48] Y. Matsuo, O. M. Kondoh, and F. Nakao, "Controlling new die mechanisms for magnetic characteristics of super-large ferrite cores," IEEE Trans on Magn, vol. 36, pp. 3411-3414, 2000.

[2.49] N. P. Suh, D. H. Cho, C. T. Rim, "Design of on-line electric vehicle (OLEV)," Plenary lecture at the 2010 CIRP Design Conference, April 2010.

[2.50] G. A. Covic and J. T. Boys, "Inductive power transfer," Proceedings of the IEEE, vol. 101, pp. 1276-1289, 2013.

[2.51] M. Budhia, G. Covic, and J. Boys, "Magnetic design of a three-phase Inductive Power Transfer system for roadway powered Electric Vehicles," IEEE Vehicle Power and Propul. Conf., 2010, pp. 1-6.

[2.52] S. Lee, J. Huh, C. Park, N. S. Choi, G. H. Cho, and C. T. Rim, "On-line electric vehicle using inductive power transfer system," IEEE ECCE, 2010, pp. 1598-1601.

[2.53] J. Huh, S. Lee, C. Park, G. H. Cho, and C. T. Rim, "High performance inductive power transfer system with narrow rail width for on-line electric vehicles," IEEE ECCE, 2010, pp. 647-651.

[2.54] J. Huh, S. W. Lee, W. Y. Lee, G. H. Cho, and C. T. Rim, "Narrow-Width inductive power transfer system for online electrical vehicles," IEEE Trans. on Power Electron., vol. 26, pp. 3666-3679, 2011.

[2.55] J. Shin, B. Song, S. Lee, S. Shin, Y. Kim, G. Jung, et al., "Contactless power transfer systems for on-line electric vehicle (OLEV)," IEEE IEVC, 2012, pp. 1-4.

[2.56] S. Ahn and J. Kim, "Magnetic field design for high efficient and low EMF wireless power transfer in on-line electric vehicle", Proc. EuCAP, pp. 3979-3982, 2011

[2.57] S. Boyune , S. Jaegue , L. Seokhwan , S. Seungyong , K. Yangsu , J. Sungjeub and J. Guho, "Design of a high power transfer pickup for on-line electric vehicle (OLEV)", Proc. IEEE Int. Electr. Veh. Conf., pp. 1-4, 2012

[2.58] M. G. L. Roes, J. L. Duarte, M. A. M. Hendrix, and E. A. Lomonova, "Acoustic Energy Transfer: A Review," IEEE Trans.Ind. Electron., vol. 60, pp. 242-248, 2013.

[2.59] M. Kline , I. Izyumin , B. Boser and S. Sanders, "Capacitive power transfer for contactless charging", Proc. 26th Annu. IEEE Appl. Power Electron. Conf. Expo., pp. 1398-1404, 2011

[2.60] J. A. Rose and J. A. Cates, "Capacitive charge coupling with dual connector assemblies and charging system," US5714864 A, Feb 3, 1998

[2.61] C. Liu , A. P. Hu , N.-K. C. Nair and G. A. Covic, "2-D alignment analysis of capacitively coupled contactless power transfer systems", Proc. IEEE ECCE, pp. 652-657, 2010

[2.62] C. Liu, A. P. Hu, B. Wang, and N. K. C. Nair, "A capacitively coupled contactless matrix charging platform with soft switched transformer control," IEEE Trans.Ind. Electron., vol. 60, pp. 249-260, 2013.

[2.63] S. Chopra and P. Bauer, "Driving range extension of EV with on-road contactless power transfer: a case study," IEEE Trans. on Ind. Electron., vol. 60, pp. 329-338, 2013.

[2.64] J. Acero, C. Carretero, I. Lope, R. Alonso, x00D, Lucia, et al., "Analysis of the mutual inductance of planar-lumped inductive power transfer systems," IEEE Trans. Ind. Electron., vol. 60, pp. 410-420, 2013.

[2.65] Y. L. Li, Y. Sun, and X. Dai, "μ-synthesis for frequency uncertainty of the ICPT system," IEEE Trans. Ind. Electron., vol. 60, pp. 291-300, 2013.

[2.66] U. K. Madawala and D. J. Thrimawithana, "A bidirectional inductive power interface for electric vehicles in V2G systems," IEEE Trans. Ind. Electron., vol. 58, pp. 4789-4796, 2011.

[2.67] D. J. Thrimawithana, U. K. Madawala, and M. Neath, "A synchronization technique for bidirectional IPT systems," IEEE Trans. Ind. Electron., vol. 60, pp. 301-309, 2013.

[2.68] M. J. Neath, A. K. Swain, U. K. Madawala, D. J. Thrimawithana and D. M. Vilathgamuwa, "Controller synthesis of a bidirectional inductive power interface for electric vehicles", Proc. 3rd IEEE ICSET, pp. 60-65

[2.69] J. Shin, S. Shin, Y. Kim, S. Ahn, S. Lee, G. Jung, et al., "Design and implementation of shaped magnetic-resonance-based wireless power transfer system for roadway-powered moving electric vehicles," IEEE Trans. Ind. Electron., vol. 61, pp. 1179-1192, 2014.

Chapter 3

Analysis of Wireless EV Charging Coupler

3.1 Introduction

Since the wireless charging pad is critical to the system performance, the loss of the coupler is an important issue. For solving geometry related magnetic field problem, there are analytical method and numerical method. The analytical model of IPT coil parameters is presented in [3.1-3.3]. The analysis based on air-core pad is presented in [3.2]. In [3.1], a planar core coupler with small airgap is analysed with the analytical method. In practical EV IPT applications, both coil only and pot core pads are not preferred. Adding magnetic material would help the coupling between the primary and secondary sides, which aids the power transfer capability and system efficiency. The coupling coefficient of coil only pads is lower compared to the same diameter pads with magnetic materials. The pot core is used in IPT applications where the core weight would not affect the system design significantly. The EV on board system prefers lightweight design as any extra weight on board would reduce the EV driving range. In order to transfer sufficient power for charging EV, the diameters of the pads are usually in 500-700 mm range, which gives proper flux linkage between them. Using pot core, which covers the whole pad within the above diameter range, results in a heavy on-board system.

3.1.1 Circular Pad Structure

The structure of the circular pad, which is widely used in stationary charging designs, is shown in Fig. 3.1. Ferrite strips are used to replace the pot core to reduce the weight of the charging pad. The coil is placed above the ferrite strips with an aluminium back plate at the bottom. The strips improve the coupling between the primary winding and the secondary winding. Ferrite is used because it has a high resistivity at medium frequency, and therefore the eddy loss is reduced [3.4].

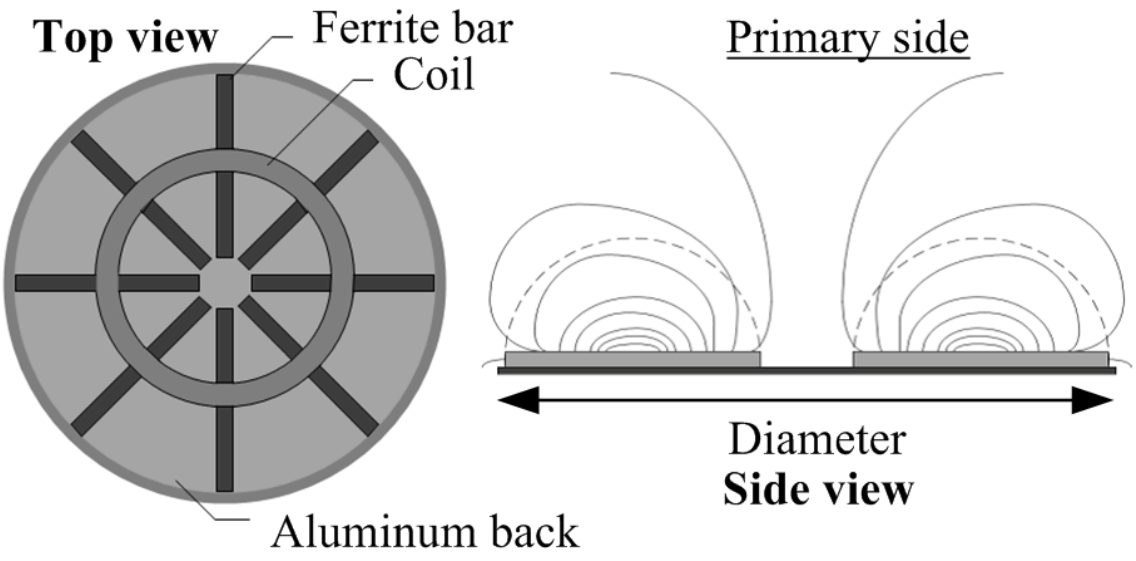

Fig. 3.1. Geometry of circular pad.

3.1.2 Power Levels

As already stated in the previous chapter, there are three charging power levels for EV charging: Levels 1, 2 and 3, and higher level indicates high power transfer capability. In this research, the IPT EV charging system aims at level 1, the opportunity charger and level 2

charger is supposed to be the main method for both private and public facilities. Level 3 is generally designed for a recharging station for commercial charging facilities and it is not considered here. The power of level 3 charger is much higher than the other two level chargers, and its voltage ratio in 20-100 kHz is a challenge for commercially available power electronics devices.

3.1.3 Self and Mutual Inductances of Coils

The two coil IPT coupler is formed by two windings with core. Each winding has its own inductance and resistance. The two windings are coupled with each other via the magnetic field. The inductance depends on the winding, core geometry, and the permeability of the core material [3.5].

The definition of inductance for a linear inductor using magnetic flux linkage method [3.5] is

$$L = \frac{\lambda}{i} = \frac{N}{i}\iint_S \ BdS \tag{3.3}$$

where λ is the flux linkage, i is the AC current which produces the flux linkage, B is the flux density, and S is the cross-sectional area.

The voltage across the inductor is

$$v_L = \frac{d\lambda}{dt} = N\frac{d\phi}{dt} = L\frac{di_L}{dt} \tag{3.4}$$

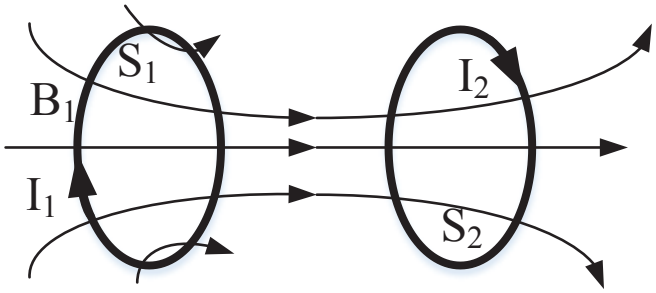

Fig. 3.2. Concept of mutual inductance using two magnetically coupled loops.

For two magnetically coupled closed loops as shown in Fig. 3.2, the closed loop C_1 forms inductor L_1 and the closed loop C_2 forms L_2. It has N_1 turns, and the current in L_1 is I_1 which produces a flux density B_1 in the space, and the flux density within the closed loop $C2$ is defined as B_{12}. The mutual magnetic flux passing through the inductor L_2 is,

$$\varphi_{12} = \int_{S_2} B_{12} \bullet d\, S_2 \tag{3.5}$$

The mutual inductance between the $L1$ and $L2$ is

$$M_{12} = \frac{\lambda_{12}}{I_1} = \frac{N_2}{I_1} \iint_{S_2} B_{12} dS_2 \tag{3.6}$$

The flux density B_{12}can be expressed in terms of vector potential A_1[3.5],

$$B_{12} = \nabla \times A_1 \tag{3.7}$$

and the magnetic potential [3.5] is given by

$$A_1 = \frac{\mu N_1 I_1}{4\pi} \oint_{C_1} \frac{dL_1}{R} \tag{3.8}$$

Hence, the Neumann's formula for mutual inductance is

$$M_{12} = M_{21} = M = \frac{\mu N_1 N_2}{4\pi} \oint_{C_1} \oint_{C_2} \frac{dL_1 \cdot dL_1}{d} \quad (3.9)$$

where d is the distance between dL_1 and dL_2.

3.1.4 Modelling of the IPT system

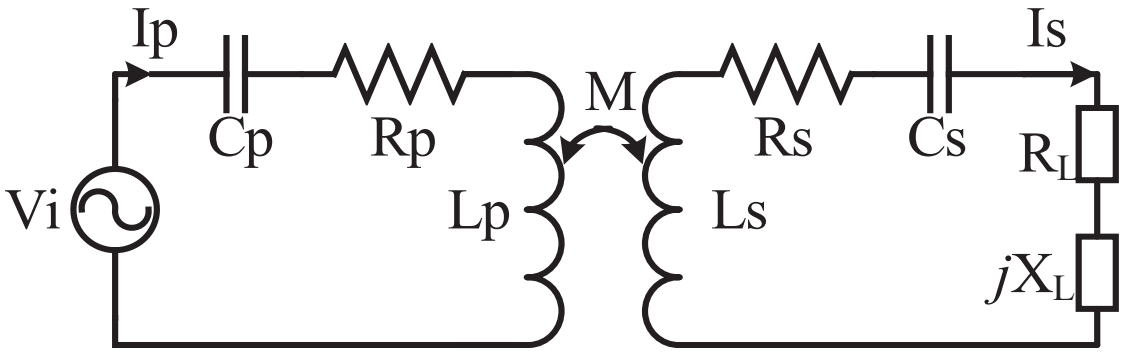

Fig. 3.3. Circuit model of IPT system.

The equivalent model of an SS compensated IPT system is shown in Fig. 3.3, where *Vi* is the input voltage of HF power source, and the angle frequency is ω. The C_p and C_s are the compensation capacitors of primary and secondary sides respectively. The L_p is the primary winding inductance and the *Ls* is the secondary winding inductance. The *M* is the mutual inductance between the primary and secondary windings. The R_L and the X_L are the load equivalent resistance and impedance. R_p and R_s are the winding resistances.

The impedances of primary side, secondary side, and load are defined as

$$Z_p = j\left(\omega L_p - \frac{1}{\omega C_p}\right) + R_p \tag{3.10}$$

$$Z_s = j\left(\omega L_s - \frac{1}{\omega C_s}\right) + R_s \tag{3.11}$$

$$Z_L = j\left(\omega L_L - \frac{1}{\omega C_L}\right) + R_L \tag{3.12}$$

The secondary side impedance is

$$Z_{22} = Z_S + Z_L \tag{3.13}$$

And the mutual impedance is

$$X_m = j\omega M \tag{3.14}$$

The circuit model could be equivalent to the circuit in Fig. 3.4. The reflected impedance from secondary side to primary side is

$$Z_{21} = \frac{X_m^2}{Z_{22}} \tag{3.15}$$

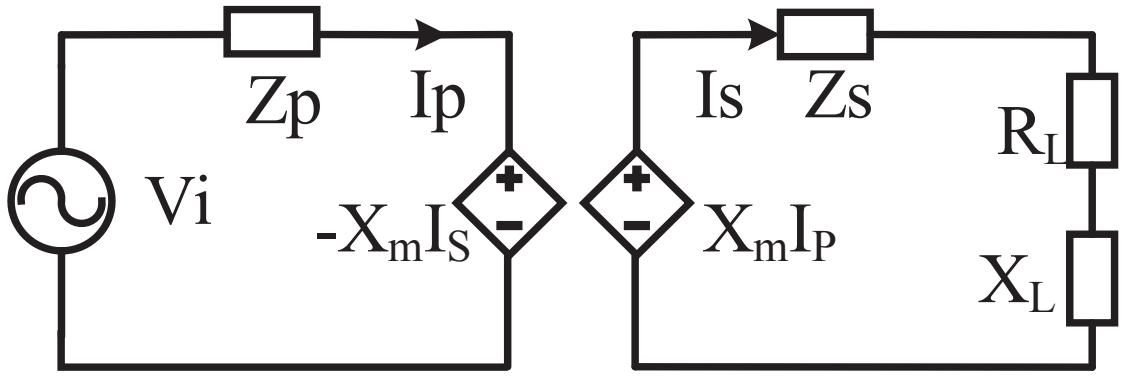

Fig. 3.4. Circuit model using equivalent source for coupler windings *Lp* and *Ls*.

Therefore, the currents of primary side and secondary side are

$$I_p = \frac{V_i}{Z_p + Z_{21}} \tag{3.16}$$

$$I_s = \frac{j\omega M I_p}{Z_s + Z_L} \tag{3.17}$$

From the equivalent circuit, the input power from the HF power sources is,

$$P_{in}(R_L, X_L) = \frac{V_i^2 [R_p + Re(Z_{21})],}{(Z_p + Z_{21})^2} \tag{3.18}$$

The real power received by the load is,

$$P_{out}(R_L, X_L) = \frac{X_m^2 V_i^2 R_L}{Z_c} = \frac{(\omega M)^2 V_i^2 R_L}{Z_c} = \frac{\omega^2 V_i^2 k^2 L_1 L_2 R_L}{Z_c} \tag{3.19}$$

where

$$Z_c = (Z_p + Z_{21})^2 (Z_s + Z_L)^2 \tag{3.20}$$

The system efficiency is

$$\eta = \frac{P_{out}}{P_{In}} \tag{3.21}$$

The system performance could be evaluated using the above equations. However, the system performances, such as the input power, output power and system efficiency, rely on the coupler parameters, including the coupling coefficient *k*, the primary and secondary inductances L_1 and L_2, and the resistances. Without careful determination of these parameters, the system modelling would be inaccurate. Therefore, coupler pad analysis is essential.

3.2 Pad Analysis

3.2.1 Analysis Methods

There are several methods to get the parameters of a designed pad structure, such as prototyping measurement, analytical method, and finite element analysis method. The prototype measurement is the most accurate method, but it might be expensive and time-consuming. The results are not applicable for other designs. In this thesis, it is only used as the validation for the pad analysis.

A) Analytical method

In [3.1] a pad with the planar-lumped core is analysed with the analytical model. The self-inductance of winding with planar coil is

$$L_i = Im(Z_{v,i}/\omega) + Im(\Delta Z_{v,i}/\omega) \tag{3.22}$$

where $Z_{v,i}$ is the self-impedance of the coil in the air, and $\Delta Z_{v,i}$ is the contribution of the core.

The mutual inductance between coil i and coil j is

$$M_{ij} = M_{v,ij} + Im(\Delta Z_{ul,ij}/\omega) \tag{3.23}$$

where $M_{v,ij}$ is the mutual inductance between coil i and coil j in the air The $\Delta Z_{ul,ij}$ is the contribution of the core material. Analytical method gives accurate result for the built model using planar core, but the contribution of the planar coil $\Delta Z_{v,i}$is complex.

The EV charging pads, which were mentioned in literature review for both stationary and dynamic wireless charging, have complex boundaries for practical reasons, such as the consideration for on board weight. For the coupler using ferrite bars, the coupler geometry is not symmetrical on all directions around the central point of the pads. It is not easy to build a model using analytical methods for pads with different numbers of ferrite bars. Furthermore, if the ferrite bars are used to replace the planar core, the geometry and the boundary condition would be even more complex, and it is almost impossible to have an analytical model. Some coupler designs, for example, with rectangular pads and DD pads, are significantly different from each other, which are not supposed to have universal analytical model.

B) Finite element analysis

The finite element analysis is a numerical method for complex geometry problem. It is widely used in mechanical engineering and electrical engineering in the motor and transformer design. As an alternative method for topology optimization of structures, the meshless method is relatively simple and is able to provide sufficient numerical accuracy and stability for certain classes of problems.

The FEA method is a good solution for complex geometry problems, and it is applicable for different pad geometries. By changing the geometry parameters in the model and solving the problems in FEA software, solutions with a certain class of accuracy would be obtained.

The disadvantage of FEA is that it requires a lot of computation resources, and at the same time it is also quite time-consuming.

3.2.2 Simulation Environment

In order to enhance the performance of the coupler, it is essential that the design of the coupler results in an optimised geometry to maximise electromagnetic field coupling. In this case, the circular pads are simulated using the ANSYS Maxwell 3D.

A) Full Scale Model

The full scale model is shown in Fig. 3.5. The parameters of the full scale model are listed in Table 3-1. A circular pad with 700 mm diameter is set in the Maxwell 3D.

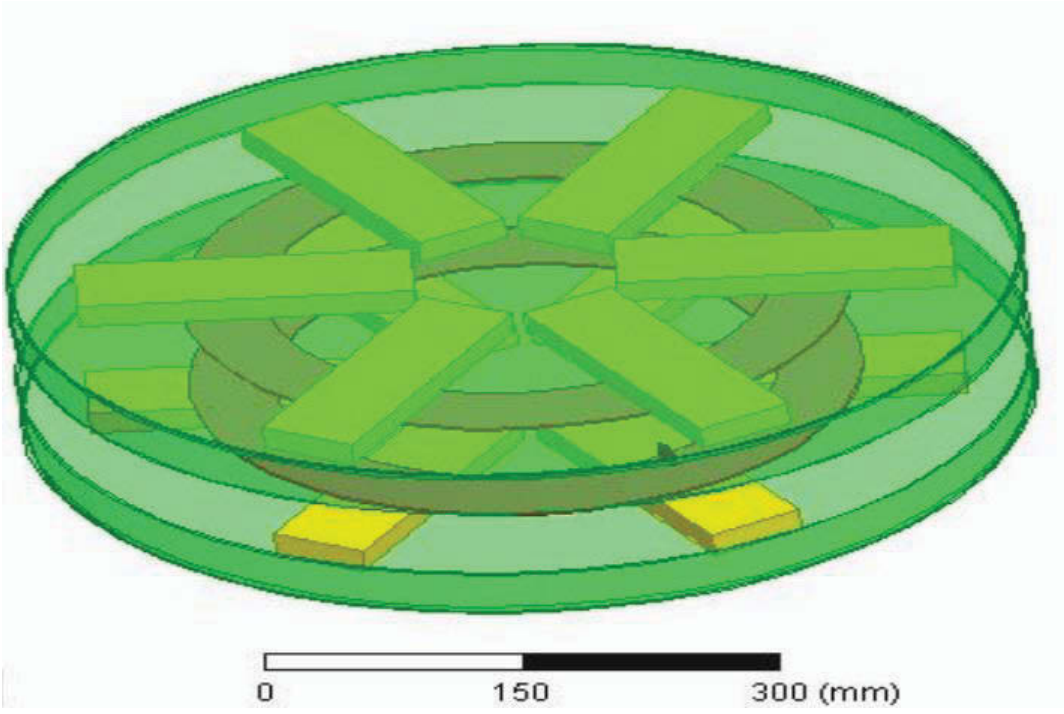

Fig. 3.5. Circular pad full scale FEA simulation model.

Table 3-1. Basic Geometrical Parameters

Back plate radius	*Rb* = 350 mm; height = 5 mm
Winding	Inner Diameter=100 mm
	Outer Diameter=250mm.
	Height = 5 mm
Strip	Length = 250 mm; width = 80 mm; height = 5 mm
Airgap	100 mm

B) One sixth model

In order to reduce the calculation time, a one-sixth section of the circular pad is modelled and periodicity is assumed. The one-sixth model is shown in Fig. 3.6 with the parameters given in Table 3-1.

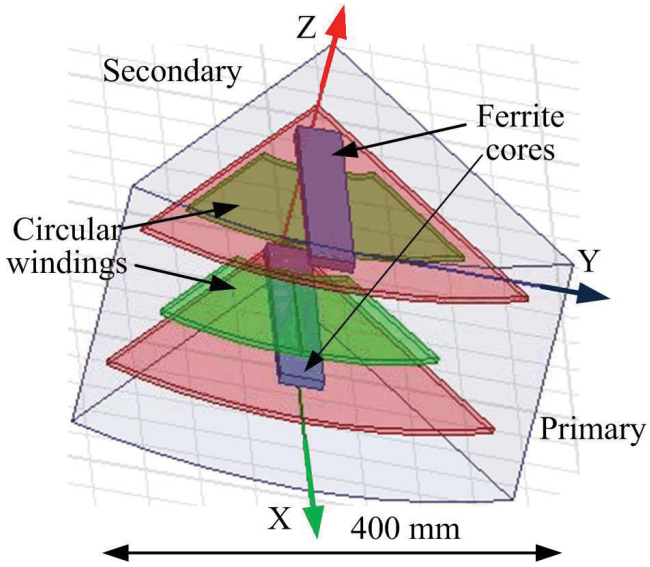

Fig. 3.6. Maxwell 3D representation of one-6th section.

3.2.3 Simulation Result

The coupling coefficient limits the power transfer ability of coupler. Using a mutual inductance model, the SS structure can be modelled by the circuit in Fig. 3.3. The series connected capacitor in secondary makes the output give the current source characteristics, while parallel connection offers the voltage source characteristics. The current source is well suited for battery charging, however, in many EV applications, DC bus is used for on board electric systems where the voltage source is more suitable. Another reason is that FEA software does not have strong utility in control to tuning the circuit into resonance, while the SS structure can be more easily tuned into resonance. There is no reflected reactance to the primary at the secondary resonance frequency in the SS structure, which can be seen from equation (3,9). This means that the secondary side would not interfere with the resonance frequency of the primary side. Both sides could be tuned into resonance, respectively.

A) Power Transfer Model

The reflected impedance from the secondary to the primary is

$$Z_r = -\frac{\omega^2 M^2}{Z_s} \tag{3.24}$$

where ω is the operational frequency and Zs is the impedance at the secondary side. When the operational frequency is the secondary resonance frequency, the secondary impedance is

$$Z_s = j\omega L_s + \frac{1}{j\omega C_s} + R = R \tag{3.25}$$

So that the reflected impedance becomes

$$Z_r = \frac{\omega^2 M^2}{R} \tag{3.26}$$

The power transferred from the grid to the load R_L can be calculated from

$$\mathrm{P} = \mathrm{Re}[Z_r] I_p^2 = \frac{\omega^2 M I_p^2}{R_L} \tag{3.27}$$

This shows that, the couplers with a higher mutual inductance have higher power transfer capability than those with lower mutual inductance. For the same coupler with different airgap or misalignment, those with higher coupling coefficient between primary and secondary winding gives higher power transfer capability.

B) 700mm Coupler FEA Simulation Results

The magnetic strips are added to enhance the coupling between the primary and secondary winding. Fig. 3.7 shows the relationship between the coupling factor and distance between the windings. There is a sharp decrease in *k* in both the ferrite core and air core simulations. The coupling coefficient *k* uses the ferrite core and is almost doubled that of air core at 280 mm air gap.

EPCOS N87 soft ferrite was used in this design. Soft ferrite was chosen because it has high permeability and low core loss at high frequency. The ferrite has low conductivity which reduces the eddy current losses in the core. The material characteristics are listed in Table 3-2.

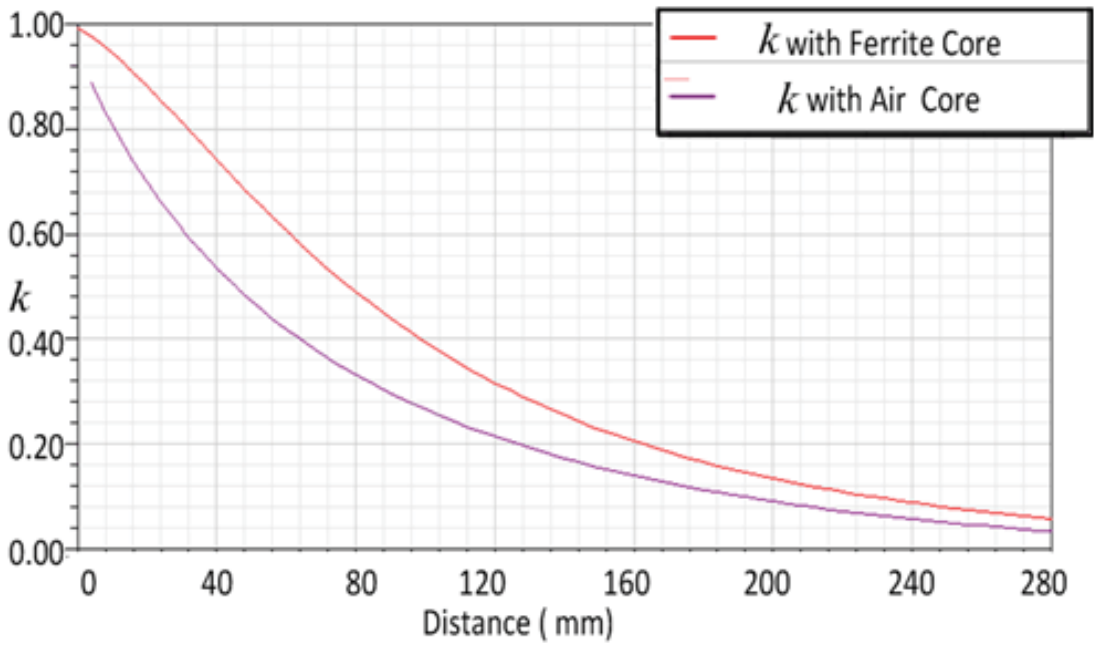

Fig. 3.7. Coupling factor *k* for transformer with and without ferrite cores.

Table 3-2. Ferrite Material Characteristics

Material	N87	
Base material	MnZn	
Electrical conductivity	σ = 10 S/m	
Saturation polarisation	J = 0.47 T	
Initial relative permeability at 25°C	2200	
Flux density	*Bs* (25°C)	490 mT
	Bs (100°C)	390 mT
Mass density	4850 kg/m^3	
Relative core loss at:		
25 kHz, 50 mT, 25°C	*Pv*	5.8 kW/m^3
25 kHz, 100 mT, 25°C		35.70 kW/m^3
25 kHz, 200 mT, 25°C		126.99 kW/m^3
25 kHz, 300 mT, 25°C		277.20 kW/m^3

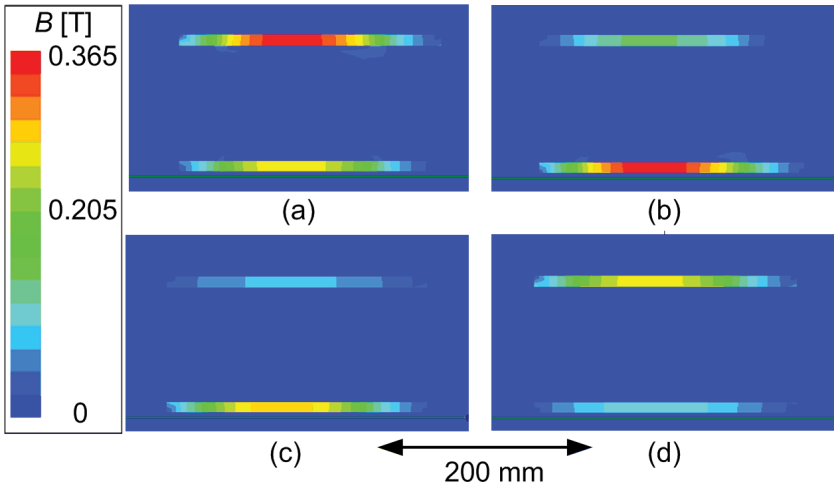

Fig. 3.8. Flux density in the ferrite cores.

Table 3-3. Parameters of the Wireless Charger

Nominal frequency	20 kHz
Primary Current (peak)	120 A
Rated load	3 ohm
Primary inductance	130 μH
Primary capacitance	4.96 μF
Secondary inductance	133 μH
Secondary capacitance	4.85 μF

With a current source I_{peak} equal to 120 A, the SS structure circuit shown in Fig. 3.3 is simulated. The winding was set to 20 turns of stranded Litz wire. The flux density in the N87

ferrite core should work within the linear range of the B/H curve to reduce the core loss. The flux density in core is shown in Fig. 3.8 in the XZ plane.

The charger works at a resonant frequency in which the secondary winding and the capacitor voltages are shown in Fig. 3.9. The peak voltages in the secondary winding and secondary capacitor are almost the same while the phases are nearly in anti-phase. Since the primary side is also resonating at the same frequency, the power factor from grid is almost unity.

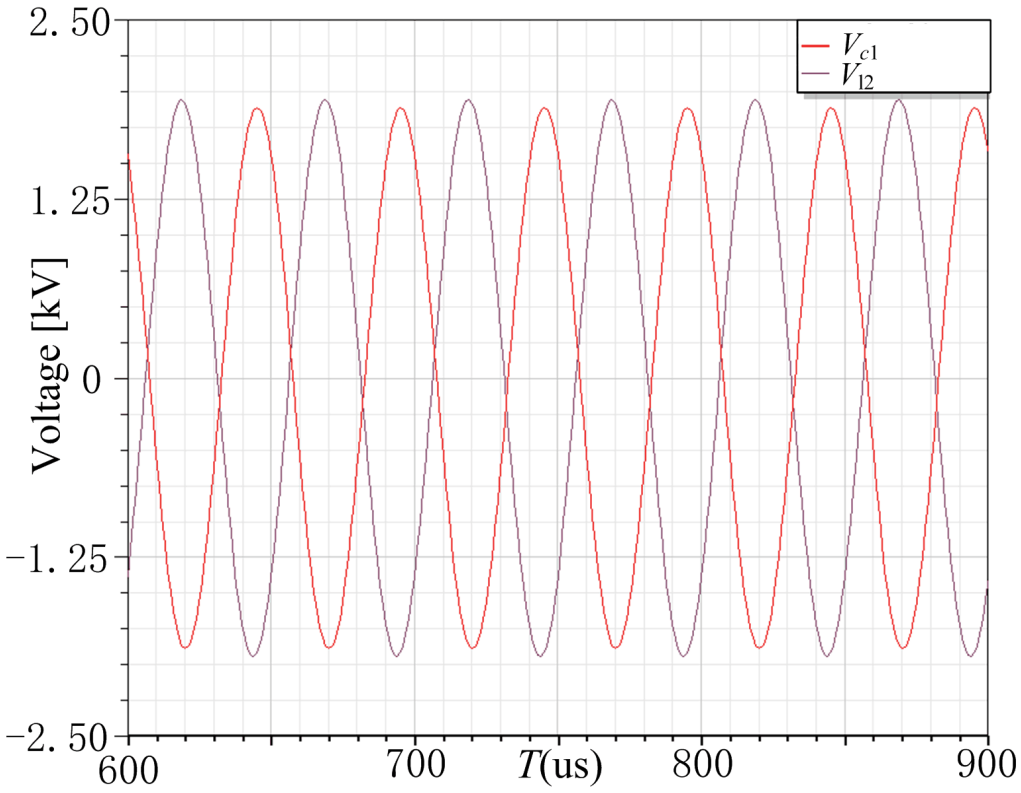

Fig. 3.9. Voltages of secondary winding and capacitor

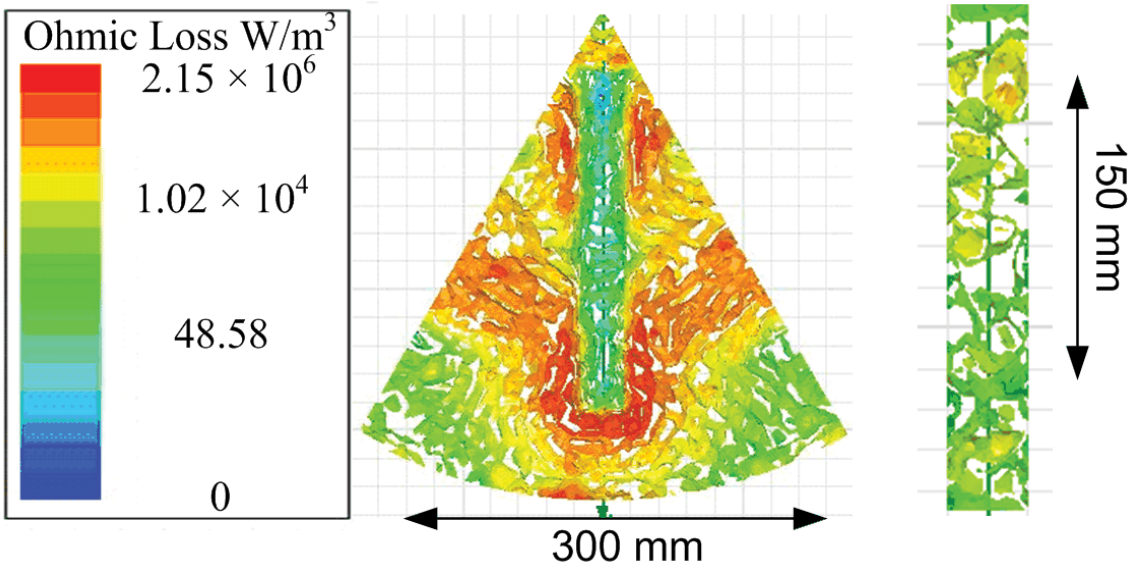

Fig. 3.10. Ohmic losses in the shield and ferrite core.

The Ohmic-losses in the shield and in the ferrite at 0.00049 μs are shown in Fig. 3.10. The majority of the eddy current loss is in the back-plate, especially in the area next to the heads of the ferrite bar. The average loss in primary side plate is 33 W. The back plates shield the space above and below as shown in Fig. 3.11. The flux density in the space above and below is less than 0.22 mT, which is much less than that on the left side where there is no aluminium plate. The aluminium plate is essential for the coupler design in order to meet human radiation explosion standards.

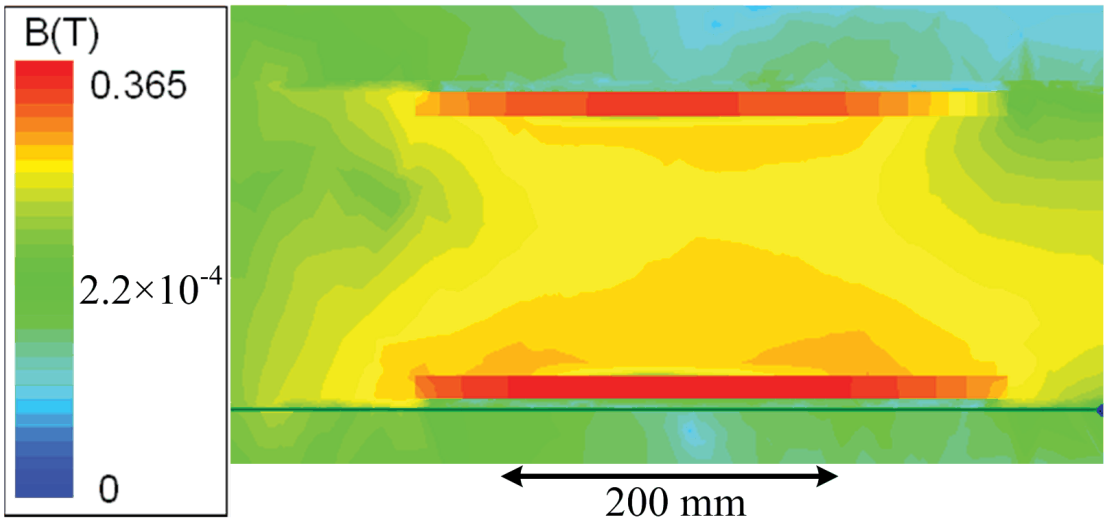

Fig. 3.11. Flux Leakage.

C) Maximum Power Transfer Capability

The saturation *Bs* shows the maximum flux density in the core material. The maximum power transfer capability is limited by the flux density in the ferrite. For a limited conduction area, *Bs* is proportional to Ni (Amp-turns). For the simulated coupler, the maximum power transfer capability is constrained by I_{peak}=120 A with 20 turns winding.

From (3.25), when the load condition is set, the output power of an SS compensated IPT system is shown.

The reduction in diameter is also a reduction in the weight of the whole coupler. To optimise the size for certain power level applications, a coupler with 560 mm diameter is also simulated with I_p = 120 A. The diameter ratio of 560 mm coupler is 0.8 compared to the 700 mm coupler. A comparison of the 700 mm coupler and 560 mm coupler is shown in Table

3-4. The transferred power is reduced dramatically with reduction of the size. The core loss, which includes the eddy current loss and hysteresis loss, is low, while the copper loss in the shields is higher.

Table 3-4. Parameters of the Wireless Charger

Parameters	560 mm Diameter	700 mm Diameter
Nominal Size factor	0.8	1
I_{load} (rms)	63.51 A	81.39 A
V_{load} (rms)	190.52 V	244 V
Power	5252.02 W	19859.16 W
Core loss (Average)	0.12 W	0.23 W
Eddy current loss in Shield	78.65 W	89.18 W
Copper loss	88.45 W	133.14 W
Coupler Efficiency	96.81%	98.88%

The forces generated by the primary and secondary winding currents on the primary winding are shown in Fig. 3.12. The force is negligible because the weight level of coupler is several tens of kgs.

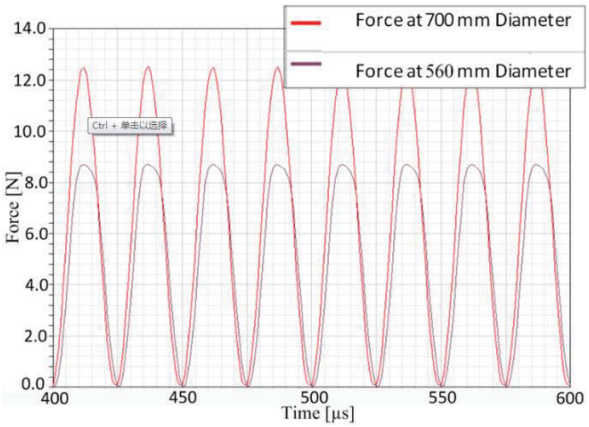

Fig. 3.12. Force on the winding.

3.3 Copper Loss analysis

The loss in the coupler can be categorised into core loss and copper loss. Litz-wire is used to reduce the eddy current loss in medium frequency applications. This section analyses the loss and the AC resistance of multi-conductor wires and calculates the magnetic field of the coupler when within a winding. The copper loss of the coupler is estimated using this calculation.

The loss in an inductive power transfer (IPT) system can be divided into switching loss in the converters, and copper and core losses in the coupler. Generally, an IPT system works in the 10 to 100 kHz range. The high frequency magnetic field induces large eddy current in both the core and the coils, therefore ferrite and Litz wire are chosen as core and winding components. The ferrite has a high resistivity and therefore the eddy current loss is low. Litz wire is selected to reduce the skin effect. The core loss in a circular pad was analysed in the pad analysis using FEA [3.6]. However, the loss in the Litz wire was ignored and assumed to be equal to the DC copper loss. Further loss calculations in multi-stranded conductors were

put forward in [3.7-3.12] under different conditions. The loss in the transformer windings is critical to the high efficiency operation of the transfer system. Litz wire is used to reduce the eddy current effect loss in high frequency applications. However, using Litz wire with the same outer diameter would cause the increase in DC resistance, which would cause extra loss compared to single conductor. In [3.11], it shows for a given Litz-wire winding, there is a frequency at which effective resistance becomes worse than the solid-round winding with the same cross-section conductor area. Therefore, Litz wire type needs to be chosen carefully in design to make the reduction in AC loss exceeding the increase in DC loss, especially for medium frequency applications, where the AC loss is not as great as high frequency applications in MHz frequency. In this part, the copper losses of two types of wires in the circular pad coupler are analysed.

3.3.1 Skin and Proximity Effect Loss and Calculation Method

The skin depth of the conductor helps define the eddy current effect on the single conductor. The skin depth is defined as

$$d = \sqrt{2/\omega\mu_0\sigma} \tag{28}$$

where ω is angular frequency, σ is conductivity of the conductor, and μ_0 is the permeability of free space.

In Fig. 3.13 for the strand representation, the current in each strand is assumed to be 1/7 of the total input current. With no proximity effect, the strand current is not affected by other

strands or external magnetic fields. For bundle representation, the total current is set to be a constant value, but the current in each strand is affected by each other and external magnetic fields. Normal wire with parallel conductors can be considered as bundles and Litz wire can be considered as stranded wire. Skin effect on strands leads to current flowing on the surface of each strand if the current is not affected by other strands. For bundled conductors, the current density is higher on the outer layer of conductors. Proximity effect in strand representation gives current redistribution due to internal proximity effects between strands and external magnetic fields, while with bundle representation the current density is higher on one side of the conductors.

For medium frequency applications, eddy current effects cause significant losses in addition to the DC resistive loss in a wire when the skin depth d is less than the conductor radius r. Therefore, the single conductor wire is not used. Litz wire is formed from a set of twisted strands or a set of twisted bundles which is formed from strands. Eddy current loss can be classified into skin and proximity effects as shown in Fig. 3.13.

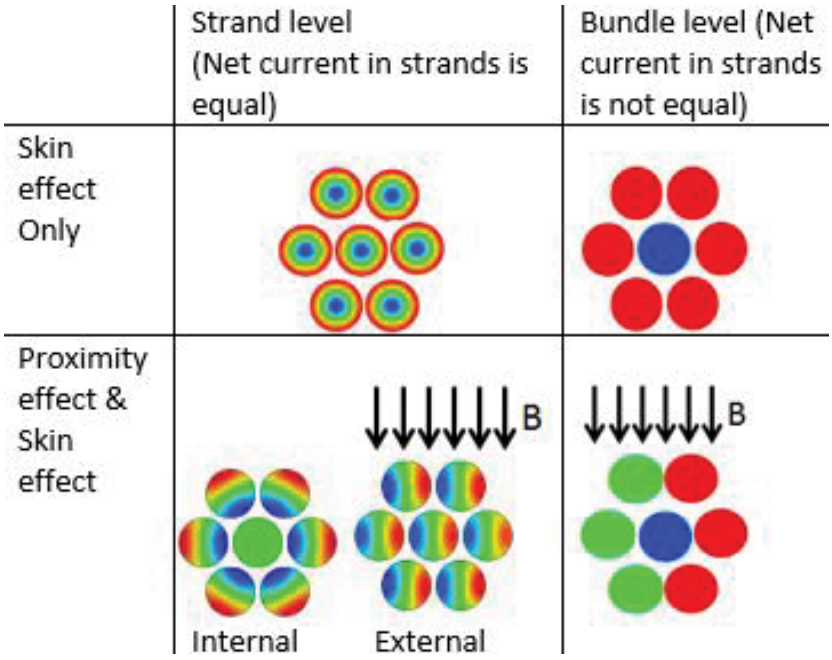

Fig. 3.13. Concept of skin and proximity effects on stranded and bundled conductors.

Skin effect is the tendency for AC current to flow near the surface of the conductor, which is caused by the magnetic flux produced by the AC current. Current flows on the surface of a single strand, while at a parallel bundle level, the current tends to flow on the surfaces furthest away from the other strands. Skin effect causes an uneven distribution of the current in the conductors, so the current density in the surface will be higher than that in the centre. Non-uniform distribution leads to a reduction in effective conduction area and causes an increase in loss. In this part, the skin-effect (or AC) resistance is defined by

$$R_{AC} = k_{sk} R_{DC} \tag{3.29}$$

where k_{sk} is the skin effect factor and R_{DC} is the dc resistance.

Proximity effect is where the current distribution in a conductor is influenced by an external magnetic field. In this research, the proximity-effect losses are defined as

$$P_{prco} = \frac{G|H|^2}{\sigma} \tag{3.30}$$

where H is the peak of the magnetic field strength H(t) and G is the proximity factor. This is per unit length so the total length of the wire l is used to obtain the total loss. The proximity effect resistance (using complex notation) is

$$R_{prox} = \frac{P_{OhmiclLoss}}{(II^*)} \tag{3.31}$$

3.3.2 Loss Analysis of a Conductor

Several analyses of high frequency winding losses are presented in the literature. The first method is generally called Dowell's method [3.13], which proposed the first analytical method for conductor windings. The round conductor was replaced by the square conductors with the same conduction areas resulting in a one-dimensional problem which can be solved analytically.

Based on a Bessel function solution, which solves the field in a cylinder conductor, Ferreira developed an analytic model. In this model, the losses in a stranded conductor are caused by an external field. The external field is the leakage field which is assumed to be uniform and equal to the average value over the conductor. The leakage field of the transformer or inductor could be modelled by the analytical method described in [3.14]. This method was considered to be more accurate in the high frequency range.

More recently the finite element method (FEM) has become popular. The finite element method is a numerical calculation method for field problems. In this chapter, the FEM model is used for copper loss analysis in an IPT coupler. The IPT coupler is a loosely coupled transformer and the geometries of couplers are quite different from a traditional transformer or inductor. The leakage field is calculated in the FEM model. Due to the orthogonality existing between skin effect and proximity effect [3.15], their losses can be calculated separately. The total loss can be calculated and the total resistance is

$$R_{total} = R_{skin} + R_{prox} \tag{3.32}$$

3.3.3 Wire Geometric Modelling

For a high frequency electromagnetic field problem, it can be divided into two analyses with two different scales to reduce the complexity. The first one is on the scale of the whole transformer in Cartesian coordinates. And the second one is at the conductor level scale as shown in Fig. 3.14.

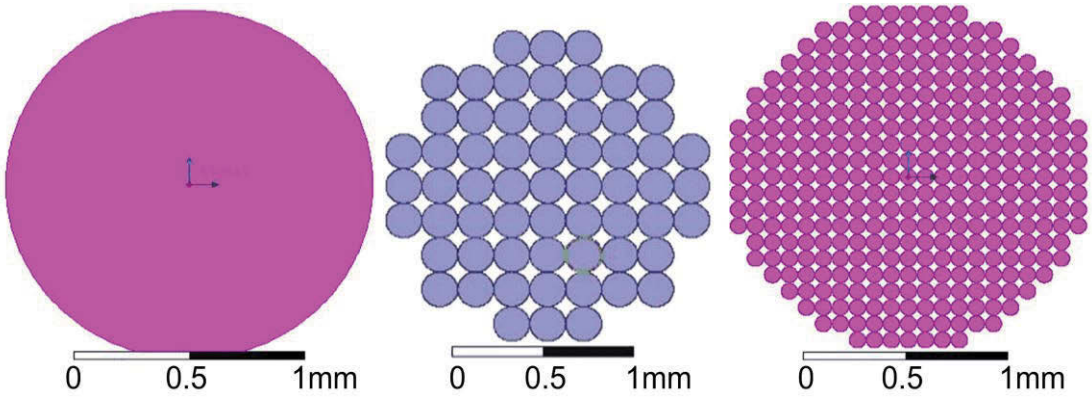

Fig. 3.14. Simulation model of wires a) single conductor; b) 61 strands model; c) 349 strands

The IPT coupler simulation model can be built on a global scale, by assuming the turns of stranded conductors as one solid uniform conducting region. By solving the large scale simulation, the eddy current loss in the core can be analysed as well as the local electromagnetic field linking the winding. The electromagnetic field for the winding is required and this is affected by the ferrite core position. The conductor level simulation is required to calculate the resistance under AC current and external magnetic field. For the coil simulation, a model was built in the FEM software Maxwell 2D, and for the coupler simulation Maxwell 3D is used.

A) Modelling of Wires

From the simulation results in [3.6], the current ratio was determined. Three kinds of wire are simulated based on the current ratio and the parameters of the wires are shown in Table 3-5. The real Type 2 Litz wire has 60 strands and Type 3 has 350 strands. For simulation reasons, the strand numbers are slightly changed to 61 and 349. Table 3-5 shows that for the

same outer diameter of Litz wire, the conduction area decreases with the increasing of strand number. This is because the fill factor decreases with more strands since insulation layer is fixed so more strands mean relatively more space for insulation. Hence Type 2 wire has a lower unit length DC resistance than Type 3 wire. The simulation models of the three wires are shown in Fig. 3.14. Each wire is simulated with two separate conditions: 1) an alternating current I_{ejwt}; and 2) an applied transverse magnetic field strength H_{ejwt} over the cross-sectional area. Both I and H are determined by the design of the IPT coupler geometry.

Table 3-5. Parameters of Simulated Wires

Type	strands	Diameter [mm]	Area [mm2]
1	1	1.6	2.01
2	61	0.2	1.92
3	349	0.08	1.75

B) Resistance of Unit Wire with Alternating Current

For 2D simulation of the wire, the total current is I_{ejwt}. The radius of the wire is r. By solving the problem in FEA, the current density of in the conductor can be calculated, and the total joule loss is

$$\mathrm{P} = \frac{1}{\sigma}\int_{s} |J|^2 \, \mathrm{dS} \tag{3.33}$$

where J is the current density, S is the conduction area and σ is the conductivity. A single conductor was simulated at different frequencies. The Ohmic loss density of a 0.7 mm conductor with I_{peak} = 10 A is shown in Fig. 3.15. The power loss per unit length of the wire is 0.56 W.

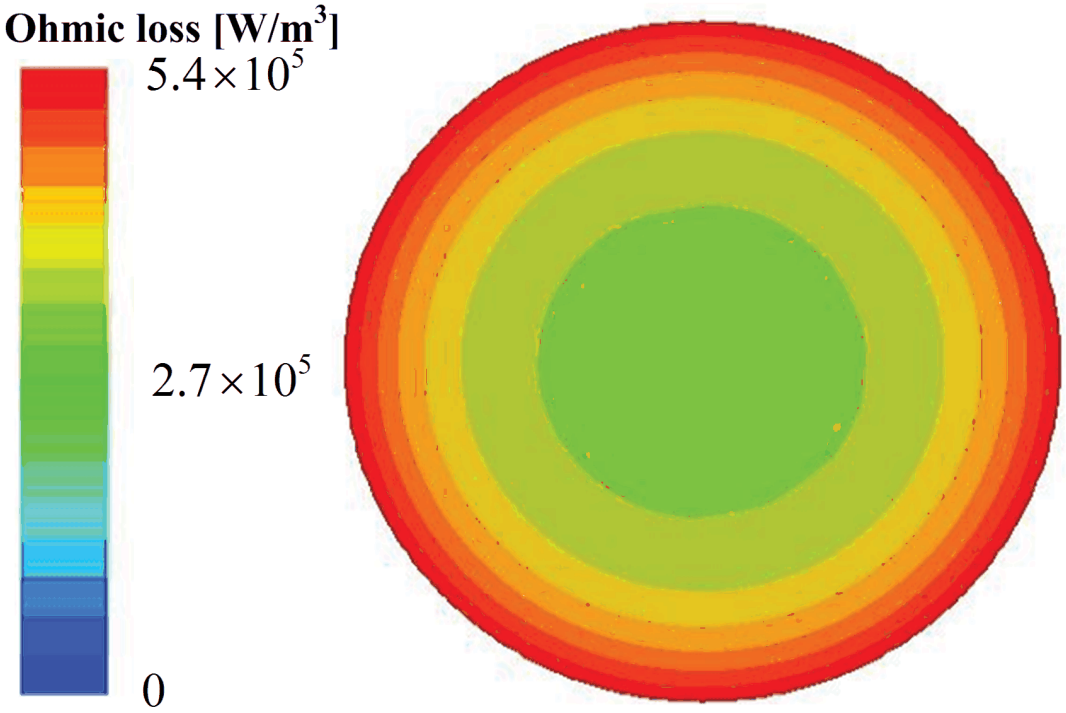

Fig. 3.15. Loss distribution in a single conductor.

Fig. 3.16 shows the loss of the unit length single conductor carrying I = 10 A. The radius varies from 0.5 to 1 mm on a linear scale and the frequency axis is from 1 Hz to 1 MHz on a logarithmic scale. The loss increases with increasing frequency and there is a dramatic increase towards the MHz range. The loss decreases with radius increase for a large conduction area since the current is constant but the area is increasing.

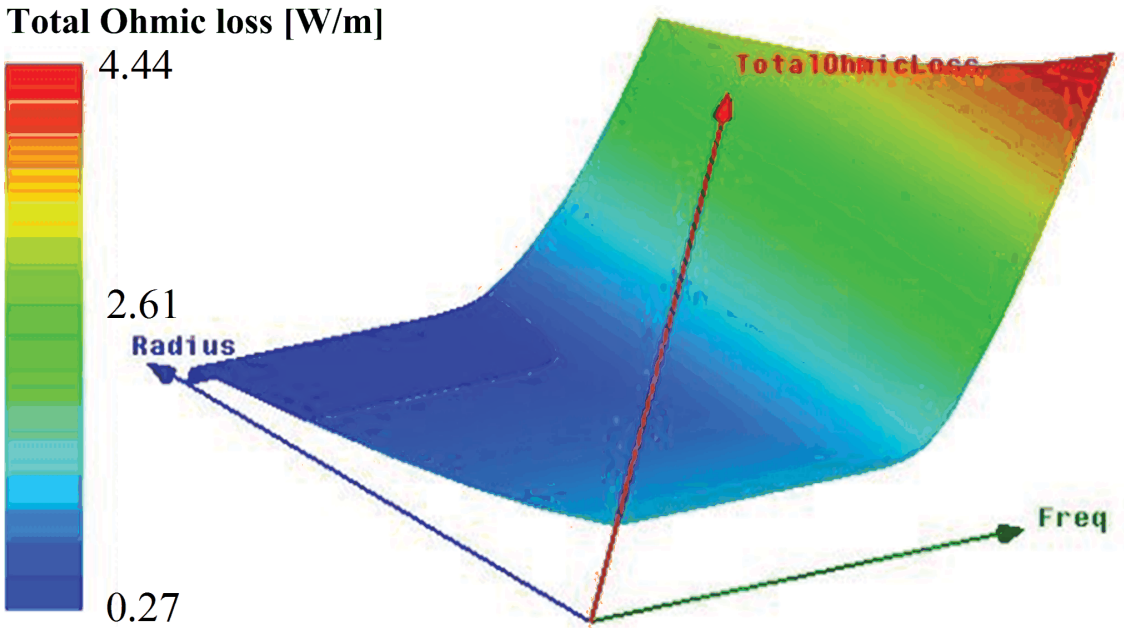

Fig. 3.16. Loss of single conductor wire verse frequency and radius.

The losses for the two wire bundles with 61 strands of 0.2 mm diameter and 349 strands of 0.08 mm are calculated. The parameters of the single strand wire and the two wire bundles are given in Table 3-5 and the DC resistances R_{dc} are noted.

The skin factors k_{sk} for the bundled wires are shown in Fig. 3.17(a), where k_{sk61} is the skin effect factor for the Type 2 wire, and k_{sk349} is the skin effect factor for the Type 3 wire. k_{sk61} increases at a higher rate than k_{sk349}.

C) Proximity Effect Simulation

The proximity effect losses for the bundled Type 2 and Type 3 wires were also simulated. The proximity factor is calculated from

$$G = \frac{P_{Prox} \cdot \sigma}{|H|^2} \tag{3.34}$$

The proximity factors for Types 2 and 3 wires are shown in Fig. 3.17(b). G_{61} increases much faster than G_{349}. This shows that using thinner wire gives a significant reduction in loss for multi-conductor wire. This is to be expected.

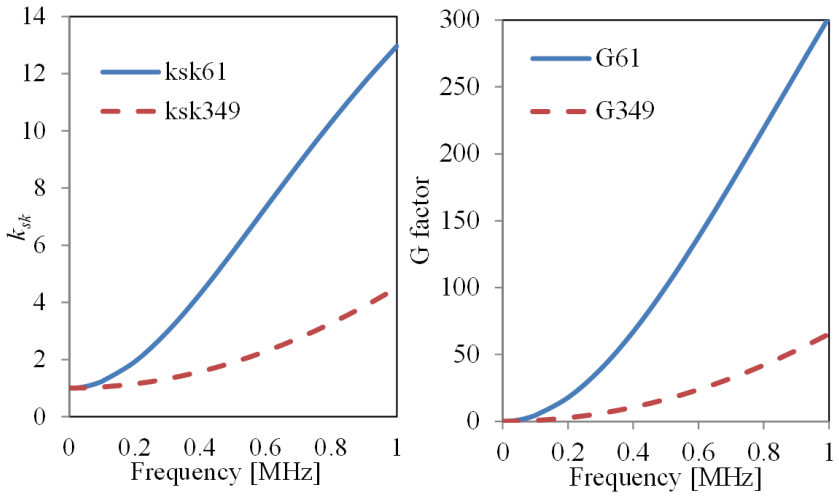

(a) (b)

Fig. 3.17. (a) Skin effect factor of wires; (b) Proximity effect G factor of wires.

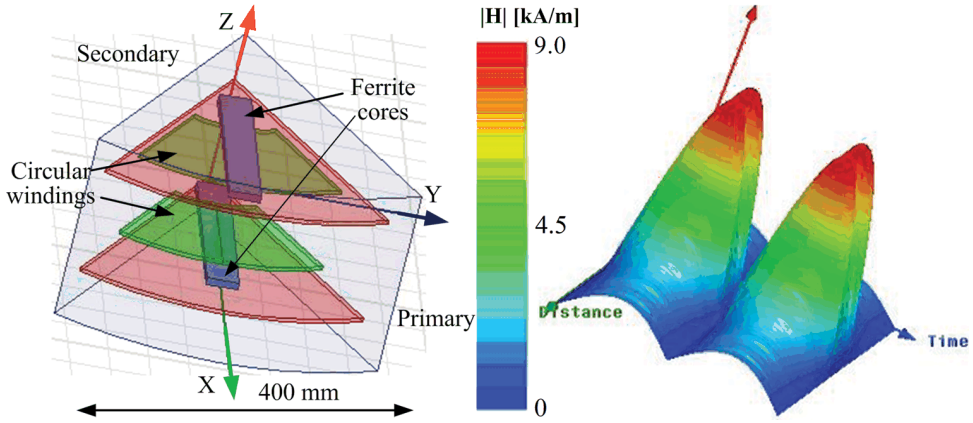

(a) (b)

Fig. 3.18. (a) Maxwell 3D representation of one-sixth section; (b) The magnetic field strength along the wire over time.

3.3.4 Coupler Model and Results

A 1/6th model of a circular pad was simulated as shown in Fig. 3.18(a). The parameters of the pad are shown in Table 3-1. The primary side ferrite is on top of the shield, and the coils are on top of the ferrite. The primary and secondary sides of coupler are symmetrical about the airgap. The ferrite material is N87 and the winding is set to 20 turns of stranded wire.

A) Magnetic Field Across the Winding

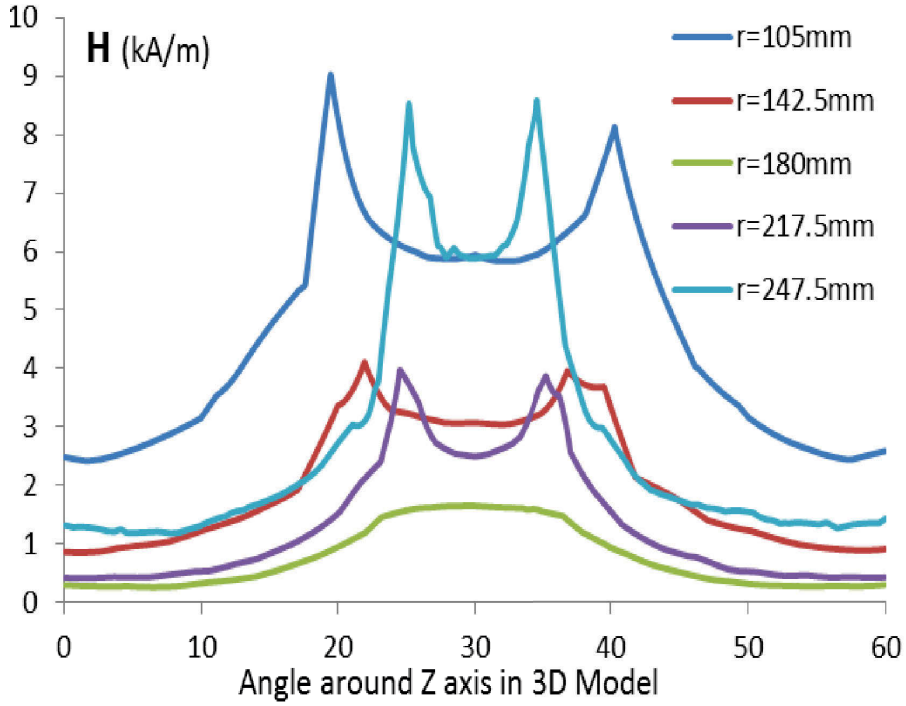

Fig. 3.19. The magnetic field strength over winding.

The magnetic field strength is shown in Fig. 3.19. From the figure we can see that both the inner and outer turns have high magnetic field strength, while in the middle of the winding, the magnetic field strength is low. This is because that the flux flows from the ferrite core,

and both sides have high flux leakage. From (3.32), we can know that the inner outer turns of wire have high losses as well.

B) Magnetic Field on the Winding Over Time

The coupler is excited by a 20 kHz AC source, and from Fig. 3.18(b) it can be seen that the shape of the H field on the winding over time is also sinusoid, so the proximity effect on the wire can be calculated using the proximity effect factor. From (3.32), the proximity effect loss at any cross area of winding can be calculated. R_{total} can be obtained from the integral of R_{ac}.

C) Total Loss of the Coupler

The total loss is

$$\mathrm{P}_{total} = \mathrm{P}_{ac} + \mathrm{P}_{prox} \tag{3.35}$$

For each turn of the winding, the proximity effect loss at a certain frequency is

$$P_{Prox,n} = \int_l \frac{G|H|^2}{\sigma} dl \tag{3.36}$$

where l is the length of the turn of the winding in the 1/6th model. The total proximity effect loss is the sum of all the 20 turns of the winding so that

$$\mathrm{P}_{total,Prox} = \sum_{n=1}^{20} P_{Prox,n} \tag{3.37}$$

The total loss of the coupler at 20 kHz is shown in Table 3-6. The total length of each winding is 22.15 m. The effective resistance of Type 3 wire is 14.3% lower than that of Type 2 wire.

Table 3-6. Copper Loss of Primary Side Winding Types 2 and 3 at 20 kHz

Calc. Param.	Pskin_total [W]	Rs [Ω]	PProx_total [W]	Rp [Ω]	Rac [Ω]
Type 2	11.87	0.237	0.384	0.0077	0.245
Type 3	10.53	0.210	0.0562	0.00113	0.2107

3.4 Rectangular Pad Analysis

In order to validate the accuracy of FEA simulation, a rectangular pad is simulated and the full scale prototype is set up.

3.4.1 Rectangular Pad Simulation

A) Simulation model with 186 mm ferrite bars on both sides

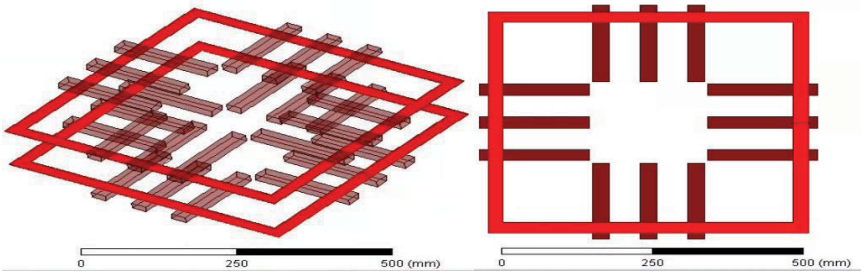

Fig. 3.20. Simulation model of rectangular pad: a) coupler model side view, b) top view of primary side coupler.

The rectangular pad model is shown in Fig. 3.20. EPCOS N87 ferrite is chosen as the core material. The size of the ferrite bar is 186*28*16 mm. For the primary side, a total number of 12 ferrite bars are used. The inner side of the ferrite bar is 100 mm from the central point, and the ferrite bars on each side of the rectangular winding is 80 mm away from the bar in the central of that side. The Litz-wire diameter is set to 2.5 mm, and each winding width has 10 turns, therefore the total winding width is 25mm. The inner side of the winding is 245 mm from the central point. The outer side of the ferrite is 572 mm.

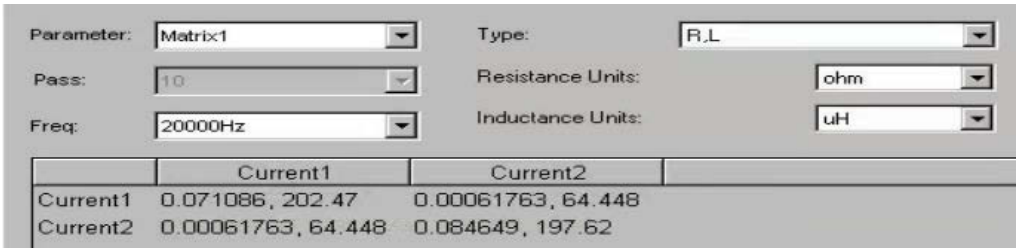

Fig. 3.21. Self-inductances of primary and secondary windings and mutual inductance with 186 mm ferrite bar on both sides

Table 3-7. Rectangular Pad Parameters

	Size
Coupler	572*572 mm^2
Winding (10 turns)	2.5 mm
Ferrite (12 piece each side)	186*28*16 mm

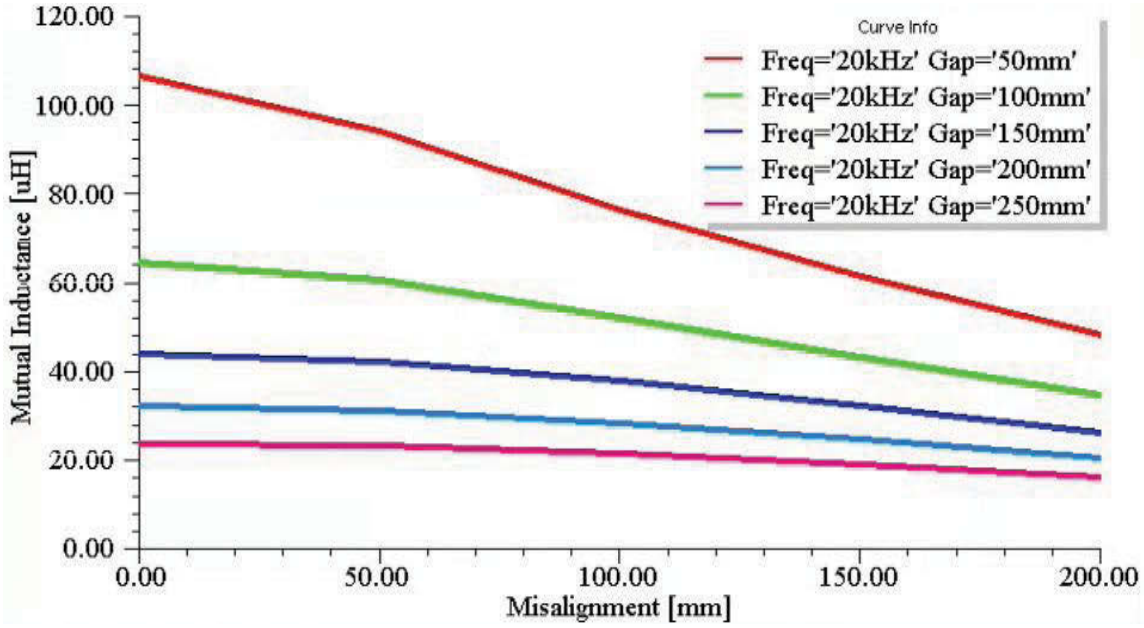

Fig. 3.22. Mutual inductance versus misalignment with 186 mm ferrite bar on both sides

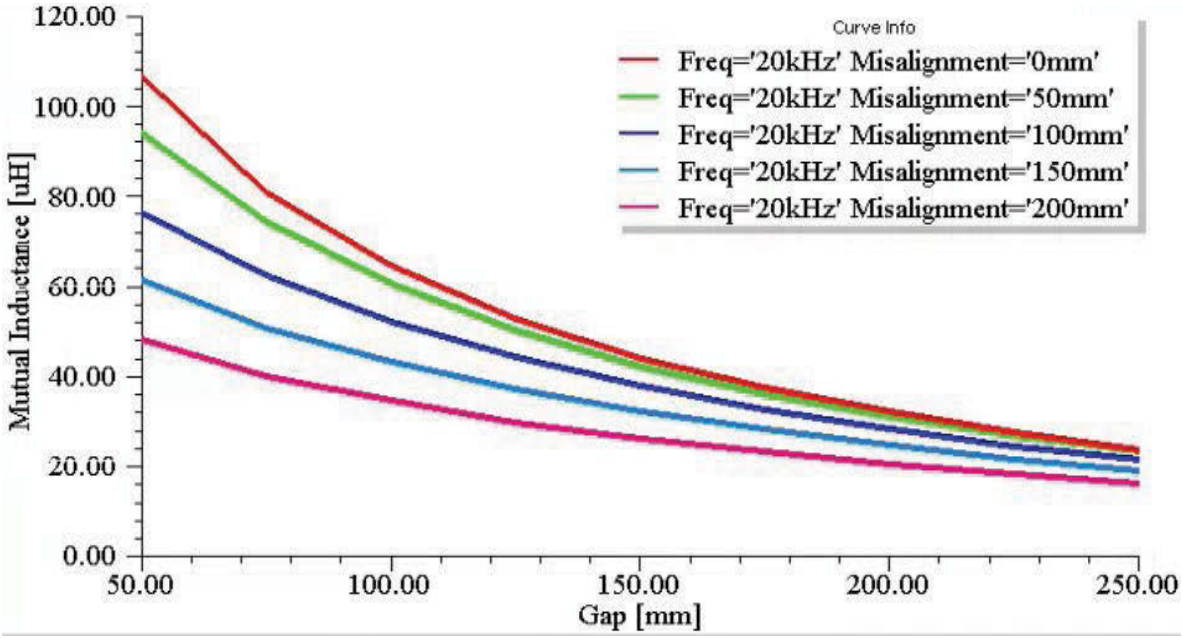

Fig. 3.23. Mutual inductance versus air bap distance with 186 mm ferrite bar on both sides

The mutual inductances between the primary and secondary windings are simulated with different airgaps and misalignment distances. Fig. 3.21 shows simulated results. The resistance and inductance are shown in each cell. The Current1/Current1 cell shows the primary side resistance and self-inductance. And Current2/Current2 cell shows the secondary side resistance and self-inductance. The Current1/Current2 and Current2/Current shows the mutual inductance therefore the values in these cells are the same. The resistance here is DC resistance as current is assumed to be distributed evenly. Fig. 3.22 shows mutual inductance versus misalignment distance. The misalignment distance starts from 0 and ends at 200mm, which is from alignment to more than 1/3 of the pad diameter.

Fig. 3.23 shows mutual inductance versus airgap distance. Mutual inductance decreases with increasing airgap and misalignment. For the same distance, the decrease ratio of mutual inductance versus gap is higher than that of the misalignment. The coupling coefficient versus airgap distance and the misalignment is shown in Fig. 3.24.

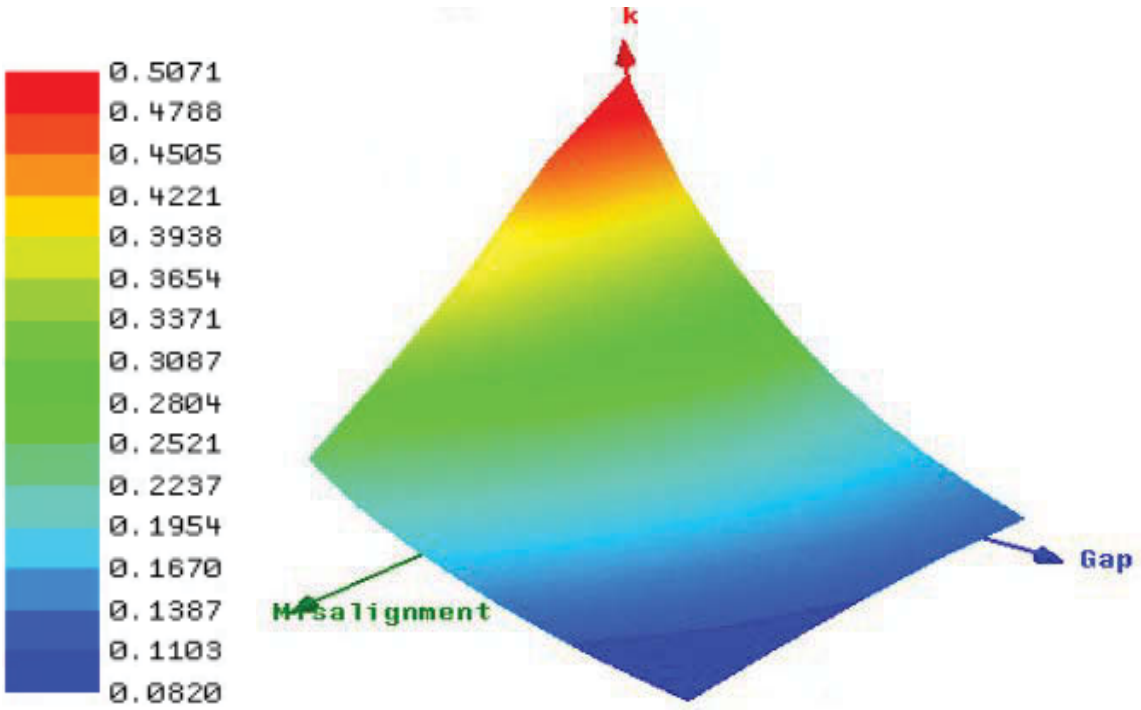

Fig. 3.24. Coupling coefficient versus misalignment and air gap distance with 186 mm ferrite bar on both sides

B) Model: secondary side with 93mm length ferrite bars

The on board system prefers light weight and low component count devices. The density of the ferrite bar is 4850 kg/m^3, and the weight of a 93*28*16mm ferrite bar is about 202 g. In order to evaluate the reduced weight secondary pad, the secondary side uses 93*28*16 mm ferrite instead of the 186*28*16 mm ferrite bars in the previous simulation. The inner side of the ferrite bar is 193 mm from the central point. The primary side still uses the same size 186*28*16mm ferrite bars. The simulation model is shown in Fig. 3.25.

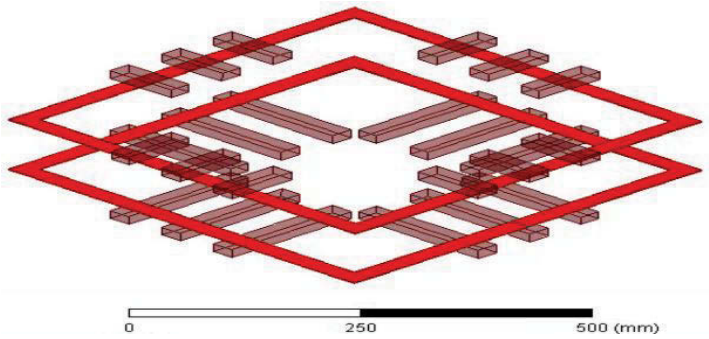

Fig. 3.25. Secondary side coil with 93 mm ferrite bar simulation

The simulated inductances of the primary and secondary windings are shown in Fig. 3.26. The mutual inductance versus the airgap is shown in Fig. 3.27, and the mutual inductance versus misalignment is shown in Fig. 3.28. The coupling coefficient of primary and secondary windings is shown in Fig. 3.29.

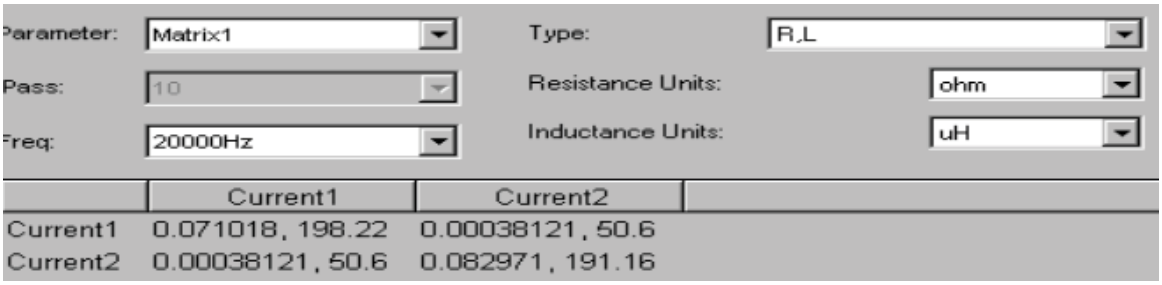

Fig. 3.26. Inductance of primary and secondary winding and mutual inductance with 93 mm ferrite bar on secondary side

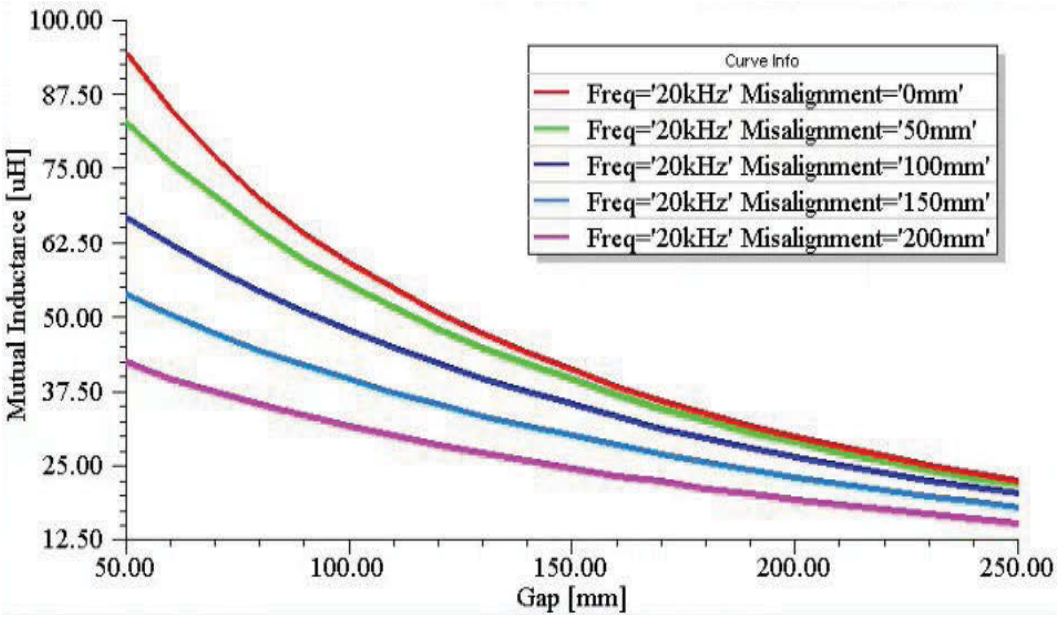

Fig. 3.27. Mutual inductance versus air gap distance with 93 mm ferrite bar on secondary side

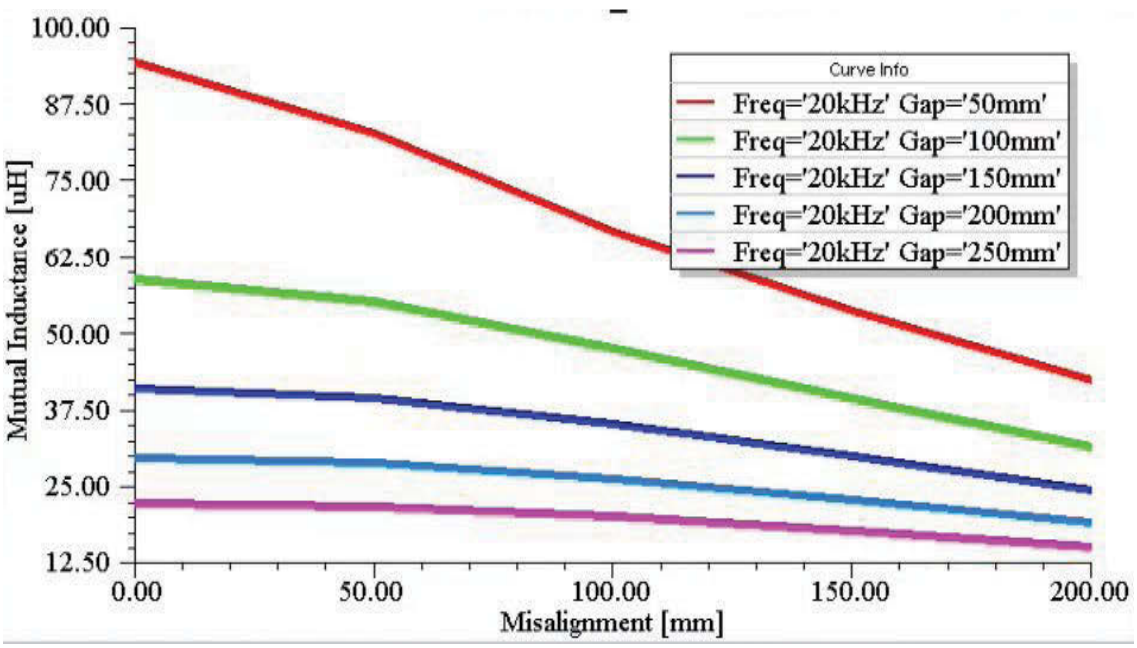

Fig. 3.28. Mutual inductance versus misalignment with 93 mm ferrite bar on secondary side

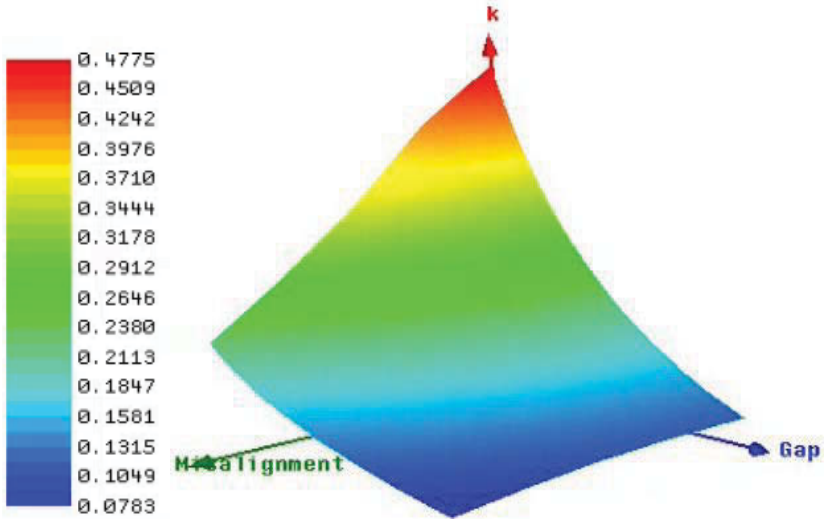

Fig. 3.29. Coupling coefficient versus misalignment and air gap distance with 93 mm ferrite bar on secondary side

C) Secondary side coil only

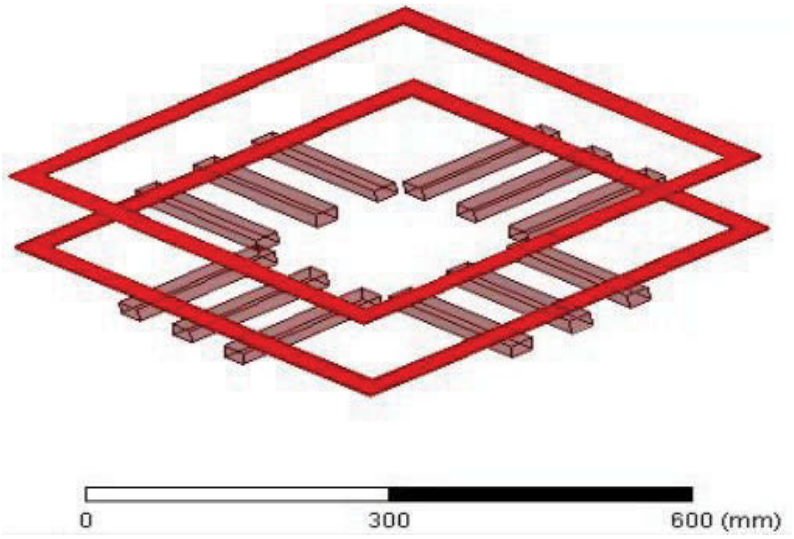

Fig. 3.30. FEA model for secondary side coil only pad

The secondary side coil only coupler is simulated in this part as shown in Fig. 3.30. The ferrite bars in the secondary side are removed. The primary side setup is the same as before.

The simulated inductances of the primary and secondary windings are shown in Fig. 3.31. The mutual inductance versus airgap is shown in Fig. 3.32, and the mutual inductance versus misalignment is shown in Fig. 3.28.

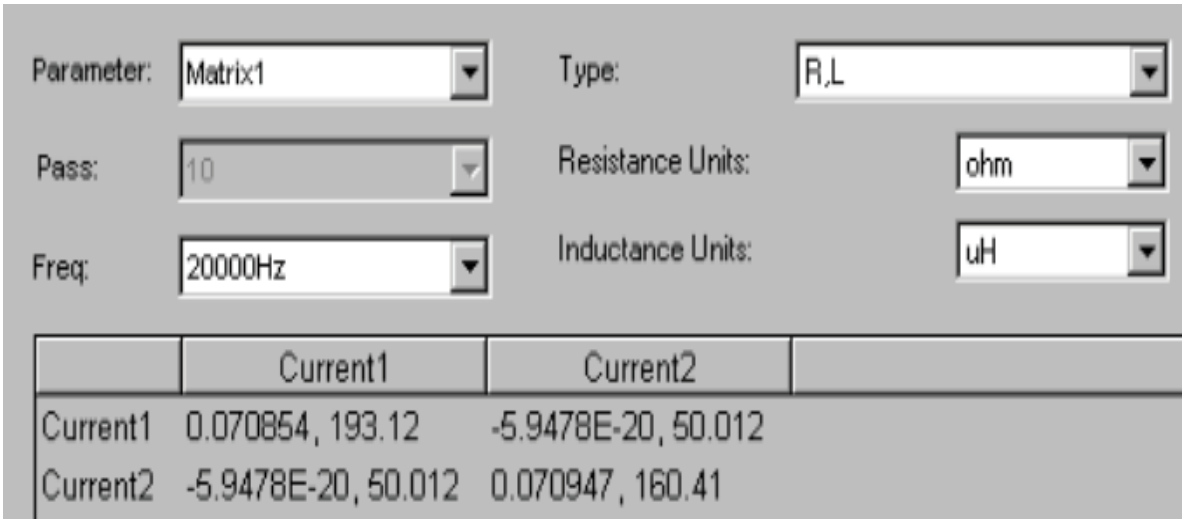

Fig. 3.31. Inductance of primary and secondary winding and mutual inductance of secondary side coil only pad

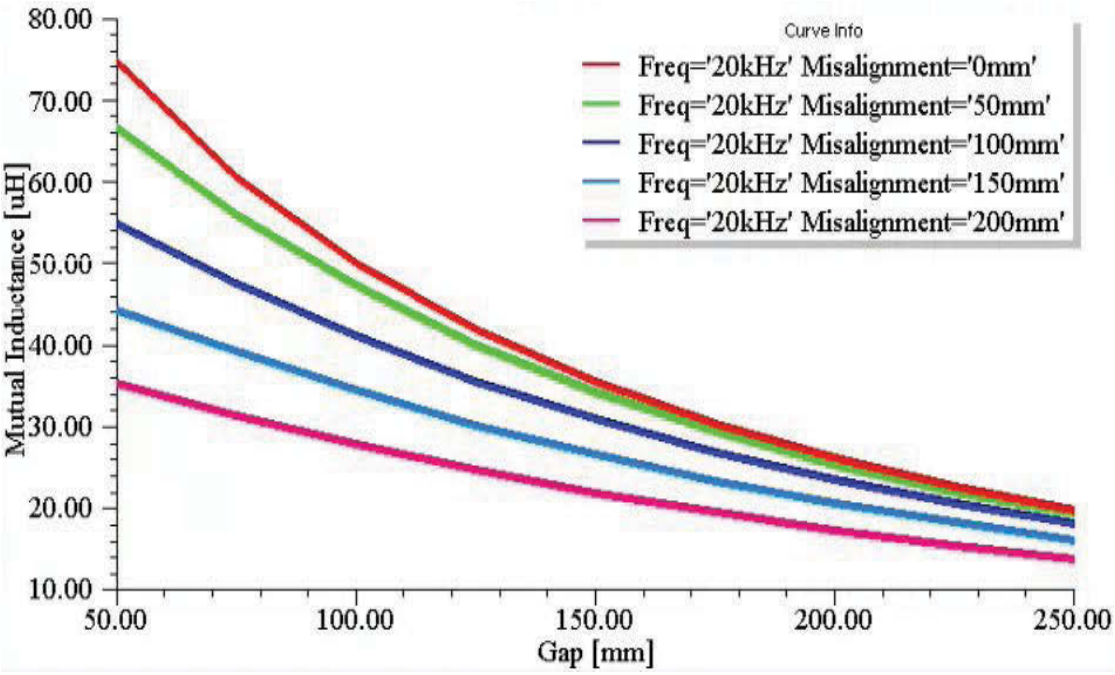

Fig. 3.32. Mutual inductance versus air gap distance with secondary side coil only pad.

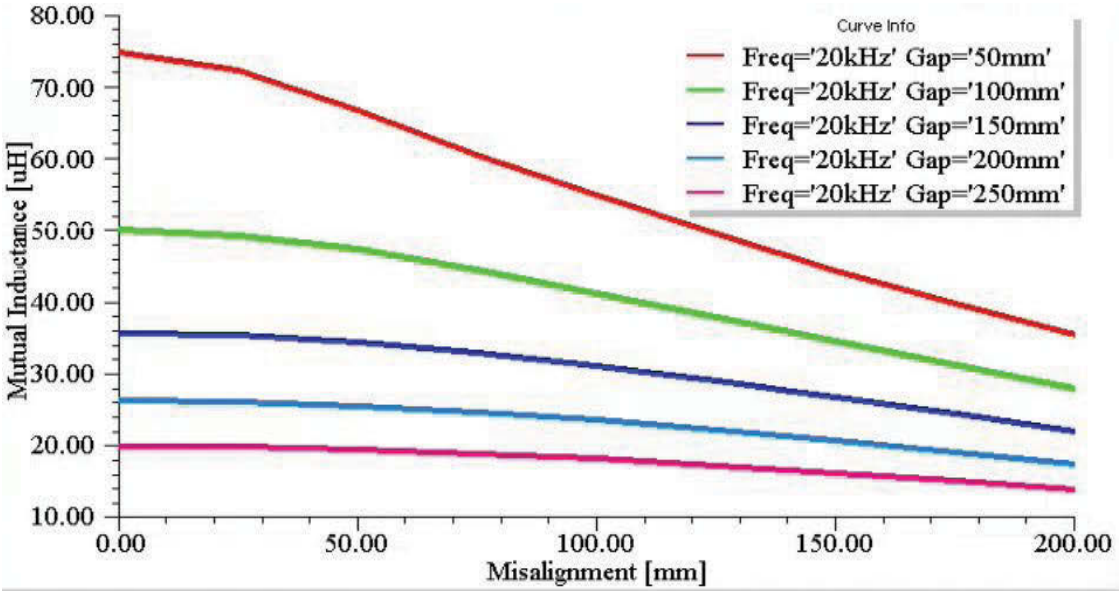

Fig. 3.33. Mutual inductance versus misalignment with secondary side coil only pad.

D) Coil Only Pad

For comparison to above pads, the coil only pad is simulated as shown in Fig. 3.34. All the ferrite bars on both sides are removed.

The simulated inductance of the primary and secondary winding is shown in the Fig. 3.35. The mutual inductance versus airgap is shown in Fig.3.36, and the mutual inductance versus misalignment is shown in Fig. 3.37.

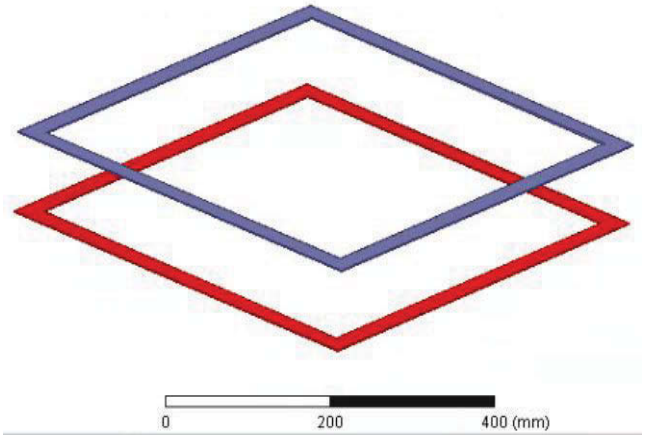

Fig. 3.34. FEA model for coil only pad.

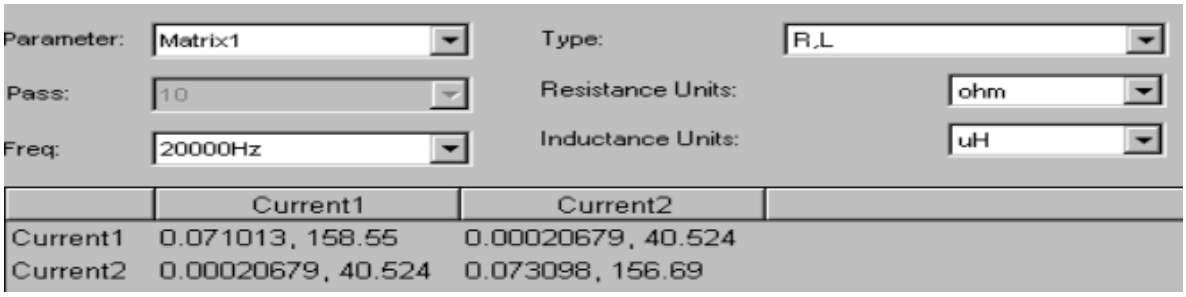

Fig. 3.35. Inductances of primary and secondary windings, and mutual inductance of coil only pad

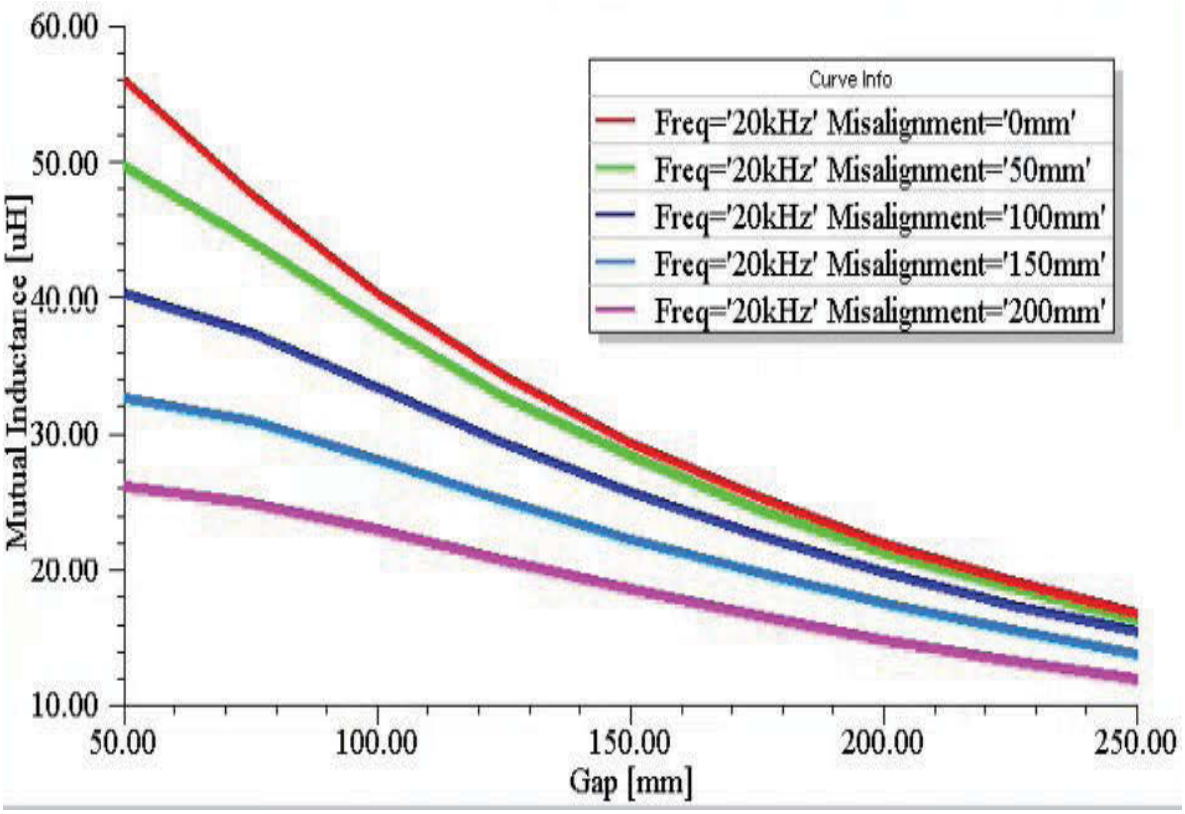

Fig.3.36 Mutual inductance versus air gap distance with coil only pad

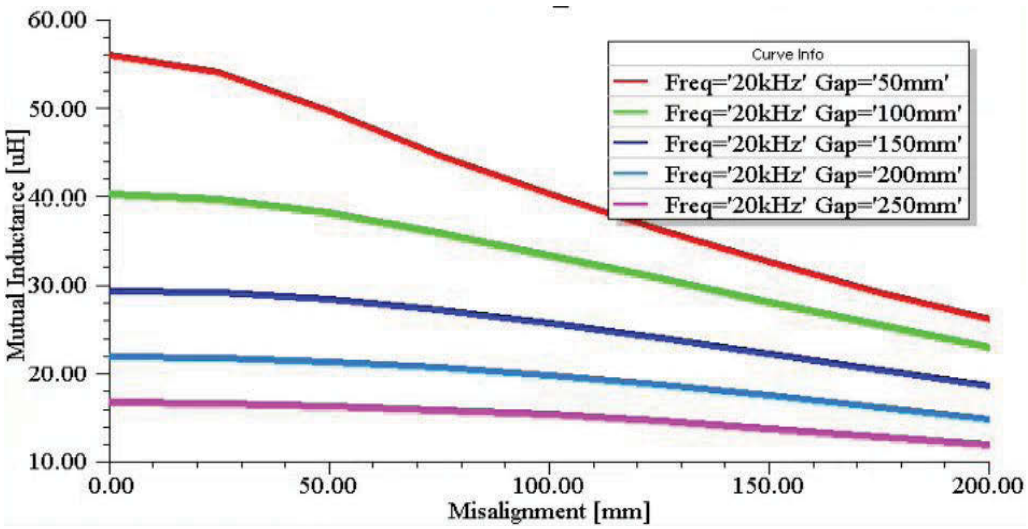

Fig. 3.37. Mutual inductance versus misalignment with coil only pad.

E) Comparison of Pads

For the same primary pad, the mutual inductances between it and above four secondary side pads are shown in the Fig. 3.38. Secondary side pad with more ferrite bars has higher mutual inductance with the primary side.

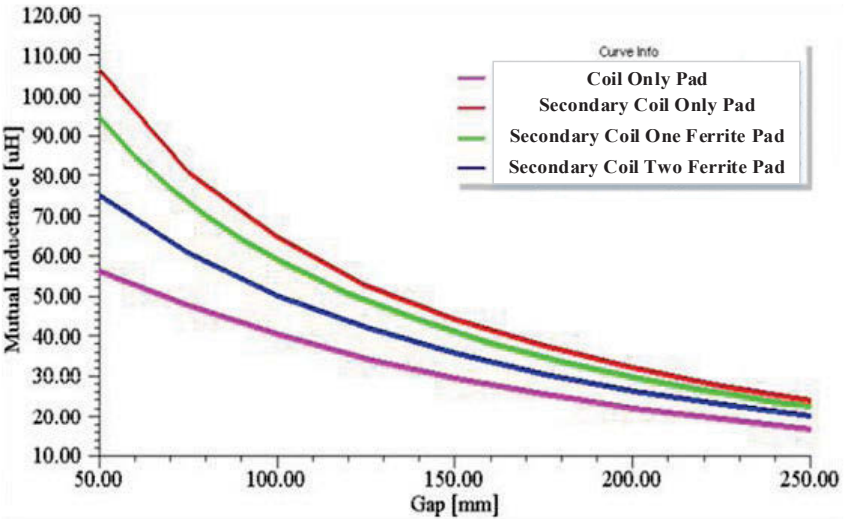

Fig. 3.38. Comparison of mutual inductance of different pads.

3.4.2 Experiment Validation

The full scale transformer with the same parameters in Table 3-7 is set up as shown in Fig. 3.39. The primary side uses two 93*28*16 mm ferrite strips to form a 186*28*16 mm longer ferrite strip. The primary winding is wound in the slot on a wood board. The ferrite bars are buried in the wood board. The secondary side setup is symmetrical to the primary. The secondary side is held by two plastic holders on four wood rods. The Litz wire with 350*0.08mm strands is used for winding. The airgap distance between the primary and secondary sides is in the range of 30mm to 400mm.

Fig. 3.39. Rectangular pad setup.

A) Self-Inductance

The inductance of the windings is measured using Keysight U1733C RLC meters. The primary winding and secondary winding are measured respectively. The self-inductance of the winding from simulation and experiment agrees well with each other.

Table 3-8. Inductance from Experiment and Simulation

	Simulation	**Experiment**
Coil only without ferrite	157.37 µH	157.61 uH
Primary Winding with two Ferrite Bars	197.52 uH	198.5 uH
Secondary Winding with one Ferrite Bar	188.95uH	192.4 uH

B) Coupling Coefficient

The mutual inductance is measured using aiding method. The aiding method coupling coefficient is shown as

$$\mathrm{k}_{aid}(z) = \left.\frac{L_{aid}-(L_1+L_2)}{2\sqrt{L_1L_2}}\right|_z \tag{3.38}$$

where *L1* and *L2* are the primary and secondary winding inductances, *Laid* is the measured inductance with *L1* and *L2* are series connected at certain airgap.

For the pad with 93*28*16mm ferrite bars, the measured aiding inductance and calculated coupling coefficient k are listed in Table 3-9.

Table 3-9. Measured Laid and calculated k with spacing

Airgap	**L_{aid}（uH）**	**k**
50	529.3	0.4776
100	462.3	0.2898
150	430.5	0.2
200	412	0.1489
250	400	0.115

The experiment and simulation results of the coupling coefficient for secondary sides with half ferrite bars are shown in Fig. 3.40. The coupling coefficients of the simulation and experiment agree well with a large airgap between windings. With smaller airgap, the results have a difference. This is because that in the experiment, the secondary side is held by two wooden rods and there is error in the measured distance. As mutual inductance has a higher increasing ratio to the distance, the error causes a significant measurement error in the coupling coefficient. This error could be removed by using a shelf type stand to hold the secondary side.

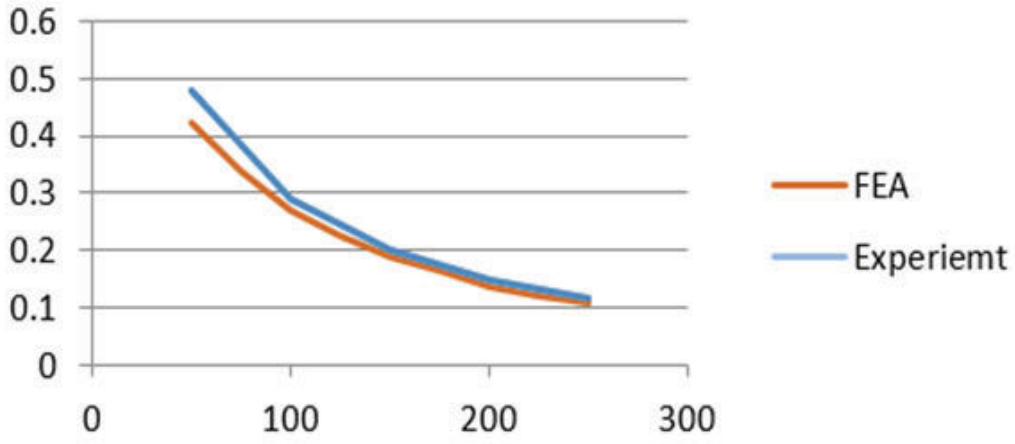

Fig. 3.40. Experiment and FEA results of coupling coefficient k

3.5 Summary

The power transfer capacity of a wireless charging system is limited by the wireless coupler. As the result, the coupler performances such as coupling coefficient and power rating are very important. An SS structure wireless charging system is simulated in the ANSYS Maxwell to estimate the coupler performance. The simulation results show that resonance

between windings and capacitors is formed. The loss in the coupler is low. The aluminium back plate significantly reduces the flux leakage to the surrounding space of the coupler, therefore reduces the potential harm to human or animals.

Then the winding loss of the circular pad is further investigated. The skin effect and proximity effect losses in two different multi-conductor wire bundles were calculated. The magnetic field strength linking the wires was estimated using FEM software. The copper loss of the coupler is calculated from these simulations. The result shows that type 3 wire has a lower effective resistance compared to type 2 wire. The wire twist was not considered in order to give a worst case scenario.

After that, the rectangular pads are analysed, and the results are validated by the experiment. Rectangular pads with different number of ferrite bars on the secondary side are simulated. The results of mutual inductance with different airgaps and misalignments are presented. The experiment shows that the simulation is accurate for predicting parameters. The parameters for circuit analysis could be based on the FEM parameter prediction for new pad design.

3.6 Reference

[3.1] J. Acero, C. Carretero, I. Lope, R. Alonso, O. Lucia, et al., "Analysis of the mutual inductance of planar-lumped inductive power transfer systems," IEEE Trans. Ind. Electron., vol. 60, pp. 410-420, 2013.

[3.2] E. R. Joy, A. Dalal, and P. Kumar, "Accurate computation of mutual inductance of two air core square coils with lateral and angular misalignments in a flat planar surface," IEEE Trans Magn., vol. 50, pp. 1-9, 2014.

[3.3] C. L. W. Sonntag, E. A. Lomonova and J. L. Duarte, "Implementation of the neumann formula for calculating the mutual inductance between planar PCB inductors", Int. Conf. Electrical Mach., pp. 1-6.

[3.4] H. Sakamoto, K. Harada, S. Washimiya and Y. Matstuda, "A noncontact charge system of an electric vehicle in the next generation", Proc. IEEE Int. Magn. Conf. (INTERMAG), no. ER-16.

[3.5] M. Kazimierczuk, "Transformers," in high-frequency magnetic components, ed: John Wiley & Sons, Ltd, 2013, pp. 412-471.

[3.6] S. Wang and D. G. Dorrell, "Loss analysis of circular wireless EV charging coupler," IEEE Trans. Magn., vol. 50, no 11 2014.

[3.7] M. Aissaoui, H. Allag, and J. P. Yonnet, "Mutual inductance and interaction calculation between conductor or coil of rectangular cross section and parallelepiped permanent magnet," IEEE Trans. Magn., vol. 50, no. 11, 2014.

[3.8] D. Dai, X. Zhang, and J. Wang, "Calculation of AC resistance for stranded single-core power cable conductors," IEEE Trans. Magn, vol. 50, article no. 11, 2014.

[3.9] M. Klauz and D. G. Dorrell, "Eddy current effects in a switched reluctance motor," IEEE Trans. Magn., vol. 42, pp. 3437-3439, 2006.

[3.10] M. Popescu and D. G. Dorrell, "Proximity losses in the windings of high speed brushless permanent magnet AC motors with single tooth windings and parallel paths," IEEE Trans. Magn., vol. 49, pp. 3913-3916, 2013.

[3.11] R. P. Wojda and M. K. Kazimierczuk, "Winding resistance of litz-wire and multi-strand inductors",IET Power Electron., vol. 5, no. 2, pp. 257-268, Feb. 2012.

[3.12] C. R. Sullivan and R. Y. Zhang, "Analytical model for effects of twisting on litz-wire losses", Proc. IEEE 15th Workshop Control Model. Power Electron., pp. 1-10, 2014.

[3.13] P. L. Dowell, "Effects of eddy currents in transformer windings," Electrical Engineers, Proceedings of the Institution of, vol. 113, pp. 1387-1394, 1966.

[3.14] J. A. Ferreira, "Improved analytical modeling of conductive losses in magnetic components," IEEE Trans. Power Electron., vol. 9, pp. 127-131, 1994.

[3.15] J. Ferreira, "Analytical computation of ac resistance of round and rectangular litz wire windings" Proc. Inst. Elect. Eng. Part B, vol. 139, no. 1, pp. 21-25.

Chapter 4

Inductive Charging Coupler with Assistive Coils

For a two-coil type wireless transformer, the maximum efficiency is limited by the coupling coefficient which rapidly decreases with increasing distance between the primary and secondary coils. The four-coil system is widely used in low power applications, where the maximum power transfer operating point is away from the maximum efficiency point. This chapter proposes an inductive charging coupler with small assistive coils, where the high power and maximum efficiency regions overlap. The design in this chapter is for level 2 EV charger.

4.1 Introduction

The output frequency of the high frequency inverter ranges from 10 kHz to several tens of MHz. For many high power applications, such as EV wireless charging, the maximum efficiency is sought in order to reduce the recharging cost. A power source with small impedance is preferred so that most of power can be transferred to the load. With the development of SiC and GaN devices, > 100 kHz inverters, which have low losses, are available for wireless charging applications. For low power applications, the impedance matching method is adopted to obtain the maximum power transfer [4.1].

For the wireless transformer design, the most common structures have two coils or four coils. In [4.2-4.7], two-coil circular pads, I pad, DD pads, and DDQ pad, were employed. Circular pads have the same misalignment tolerance in all directions, while the DD and I pads have

more misalignment tolerance in the forward and reverse directions. Power transfer linkage is established by the wireless power transfer(WPT) coupler, which is loosely coupled transformer. The coupling between the primary and secondary is low due to a large airgap.

In [4.8.4.12], four-coil systems are used in low power devices. Impedance matching is used to acquire high power output. The transfer efficiency of a four-coil system can be high, but many four-coil systems operate in the MHz frequency range, where a high-efficiency low-impedance power source currently is not available, giving a low total system efficiency [4.12] presented a four-coil 100 kHz EV system with high total efficiency. Coaxial windings were used for both sides. The high efficiency working point was away from the high power point. This means that it was oversized so that it could transfer sufficient power around the high efficiency point rather than in its high power region. Oversizing adds cost to the power electronics and transformer (higher device power ratings and thicker wire). In this chapter, an inductive charging coupler with separate small assistive coils is proposed. The frequency is 20 kHz to reduce the power electronics and eddy current losses. The proposed structure overlaps the high efficiency and high output power regions. The coupling coefficient was analysed using finite element analysis (FEA) and the power ratio was studied at circuit level. The simulation result is shown and compared with that of a similar sized two-coil system.

4.2 Wireless Charging Systems

A wireless transformer has a grid or power source primary coupler and secondary coupler which is connected to the vehicle battery charger. Generally, the primary coupler is isolated from secondary coupler. The electrical power will be transferred from the primary coupler to secondary coupler across the airgap via a magnetic link. Many wireless transformer

geometries have been proposed. The two-coil structure has one winding on the primary side and one winding on the secondary side. Each winding can be formed by one or more coils connected in series or parallel combination. For the four winding structure, there is an extra resonant coil or compensation coil in both the primary and secondary sides. The extra coils are short circuited or connected to a capacitor. Both the two winding and four winding structures are single phase applications. For single phase application, there can be multiple winding structures, but they can be treated as a combination of two or four winding systems. There is limited research on multi-phase structures. This is probably due to the complexities of a wireless transformer design and the control of the charging system.

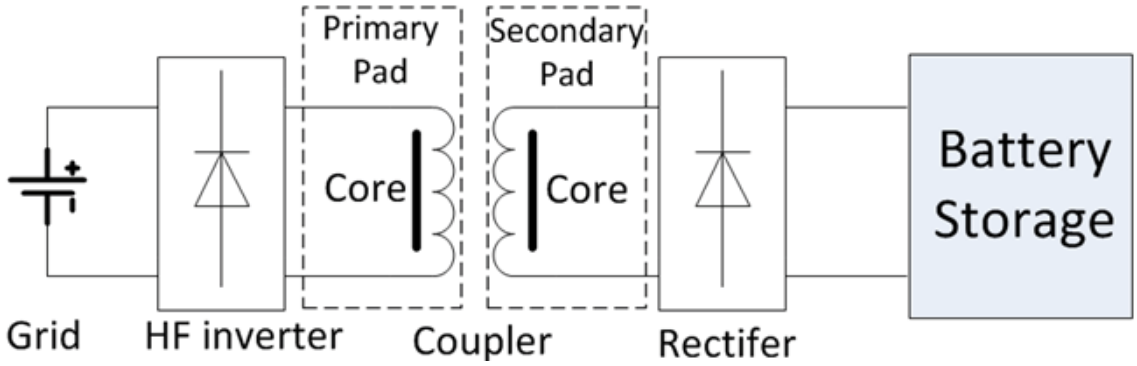

Fig. 4.1. Wireless charging circuit.

4.2.1 Two Winding Structure

The two-coil system is widely used in inductive charging applications. The general structure is shown in Fig. 4.1. Fig. 4.2 shows the equivalent circuit, where *L1* and *L2* are the inductances of the primary and secondary windings; *C1* and *C2* are the compensation capacitors and series-series (SS) capacitor compensation is used here; *R1* and *R2* are the total

parasitic resistances of the windings and capacitors, and *Rload* is the load for the wireless charging system, respectively.

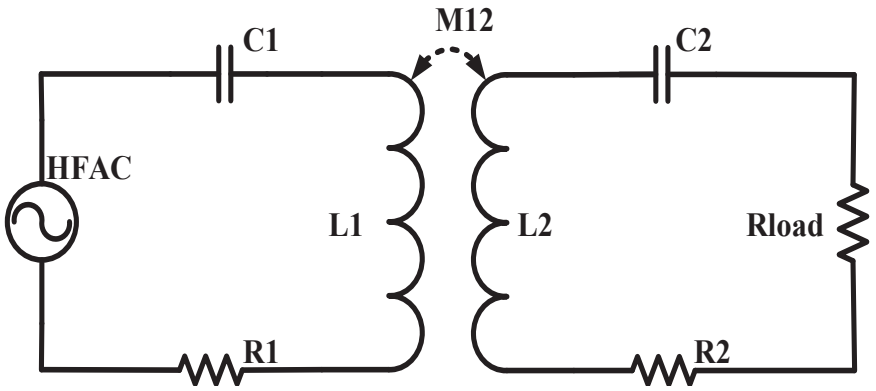

Fig. 4.2. General structure for series-series compensation.

The voltage equations can be written as

$$U = I_1 Z_1 + I_2 j\omega M_{12} \text{ and } 0 = I_1 j\omega M_{12} + I_2 Z_2 \quad (4.1)$$

where

$$Z_1 = R_1 + j\omega L_1 + {}^{1}/_{j\omega C_1} \qquad Z_2 = R_2 + R_{load} + j\omega L_2 + {}^{1}/_{j\omega C_2} \quad (4.2)$$

Assuming that the inductance is fully compensated by the capacitor at the HFAC frequency $\omega L1 = 1/\omega C1$, $\omega L2 = 1/\omega C2$, and mutual inductance $M = M12 = M21$, then

$$U = \left[R_1 + \frac{(\omega M)^2}{R_2 + R_{load}}\right] I_1 \quad (4.3)$$

$$j\omega M Y_{11} U = \left(R_{eq} + R_2 + R_{load}\right) I_2 \quad (4.4)$$

$$R_{eq} = R_1 + \frac{(\omega M)^2}{R_2 + R_{load}} \quad (4.5)$$

Therefore, the ratio between *I1* and *I2* is

$$\frac{|I_1|}{|I_2|} = \frac{(R_{eq}+R_2+R_{load})}{\omega M R_1 R_{eq}} = \frac{(R_{eq}+R_2+R_{load})}{kQR_1R_{eq}} \tag{4.6}$$

The efficiency of the two-coil system is

$$\eta = \frac{I_2^2 R_{load}}{I_2^2(R_{load}+R_2)+I_1^2 R_1} \tag{4.7}$$

Fig. 4.3 shows the simulation results from circuit analysis (the inductance and resistance values used in circuit analysis are from a model developed in ANSYS Maxwell 3D) for the efficiency and power output for variation of the coupling coefficient *k*. The system frequency is 20 kHz and the inductance is fully compensated by the capacitors. Both efficiency and power output, without the SS capacitors, decrease with decreasing coupling coefficient. The efficiency curve with SS compensation shows a similar trend but the output power is much higher than that without the SS capacitors when k is small. Since the efficiency increases with the increasing *k*, the coupling coefficient is an important design parameter. For private-use EV wireless charging applications, the goal is to reach Level 1 or Level 2 charging, with the power from 1 to 6.6 kW, with the highest efficiency possible. Due to practical considerations, such as the limitation of the coupler size and essential gap between ground and vehicle, the coupling coefficient is between 0.1 and 0.3 from most published studies.

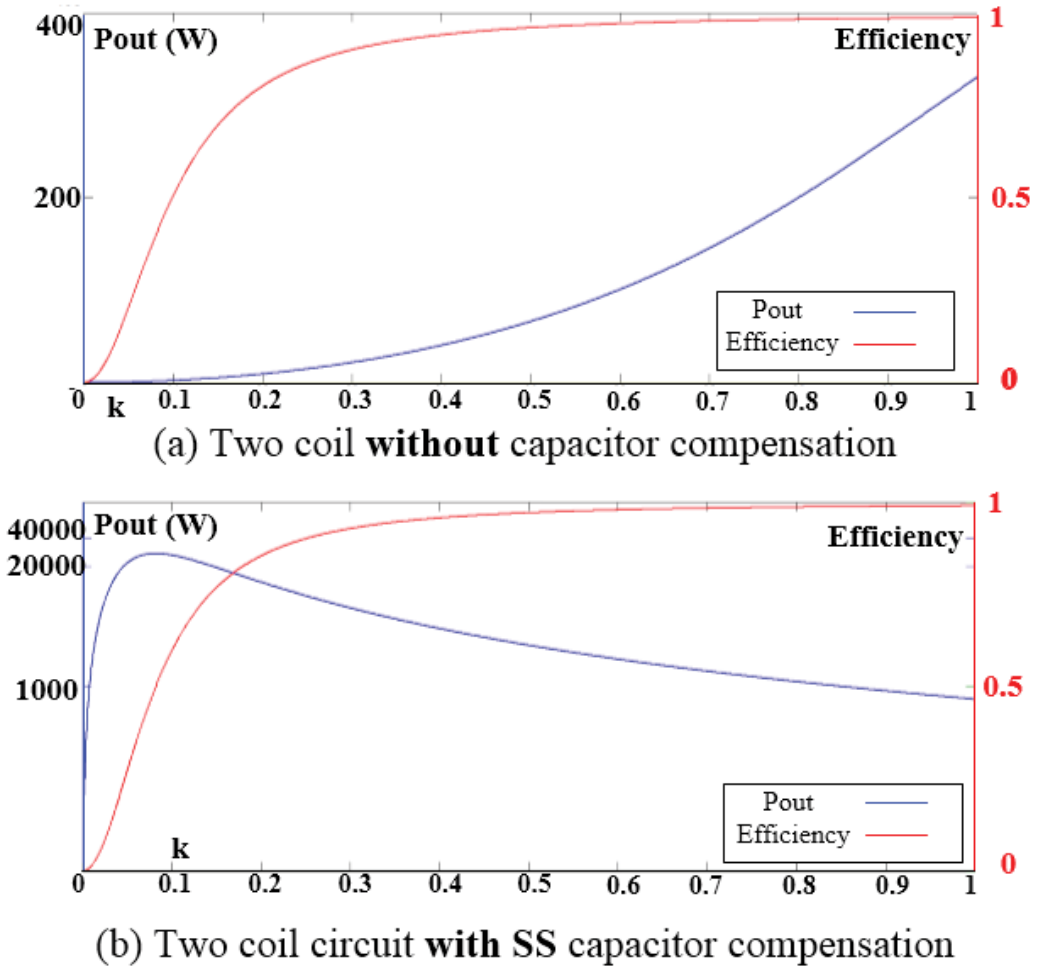

Fig. 4.3. Simulation results: (a) uncompensated circuit efficiency and power output, (b) SS compensated efficiency and power output

4.2.2 Four Winding Structure

The four-coil system was reported in [4.11]. Impedance matching between the input and output is applied to acquire the maximum power output in low power applications, which often have a system efficiency of lower than 50%. In [4.12], a four-coil system is used for EV wireless charging, in which the maximum efficiency principle is used. There is still a power-efficiency split in the coaxial coil coupler where the maximum power and efficiency

cannot be reached at the same time. The general structure of four winding system is shown in Fig. 4.4.

The system is driven by a high frequency power source. The circuit equation matrix for a four-coil system is

$$\begin{bmatrix} U_0 \\ 0 \\ 0 \\ 0 \end{bmatrix} = \begin{bmatrix} Z_1 & j\omega M_{12} & j\omega M_{13} & j\omega M_{14} \\ j\omega M_{21} & Z_2 & j\omega M_{23} & j\omega M_{24} \\ j\omega M_{31} & j\omega M_{32} & Z_3 & j\omega M_{34} \\ j\omega M_{41} & j\omega M_{42} & j\omega M_{43} & Z_4 \end{bmatrix} \begin{bmatrix} I_1 \\ I_2 \\ I_3 \\ I_4 \end{bmatrix} \tag{4.8}$$

where $Z_{\mathrm{i}} = R_{wi} + j\omega L_i + {}^{1}/_{j\omega C_{\mathrm{i}}}$ and i=1,2,3.

$$Z_4 = R_{w4} + j\omega L_4 + {}^{1}/_{j\omega C_4} + R_{load} \tag{4.9}$$

and M is the mutual inductance between two-coils. The power output to the load is

$$P_{out} = |I_4|^2 R_{load} \tag{4.10}$$

The efficiency of the four-coil system is

$$\eta = \frac{P_{out}}{P_{out}+P_{loss}} = \frac{|I_4^2|R_{load}}{|I_4^2|R_{load}+\sum_{i=1}^{4}|I_i^2|R_i} \tag{4.11}$$

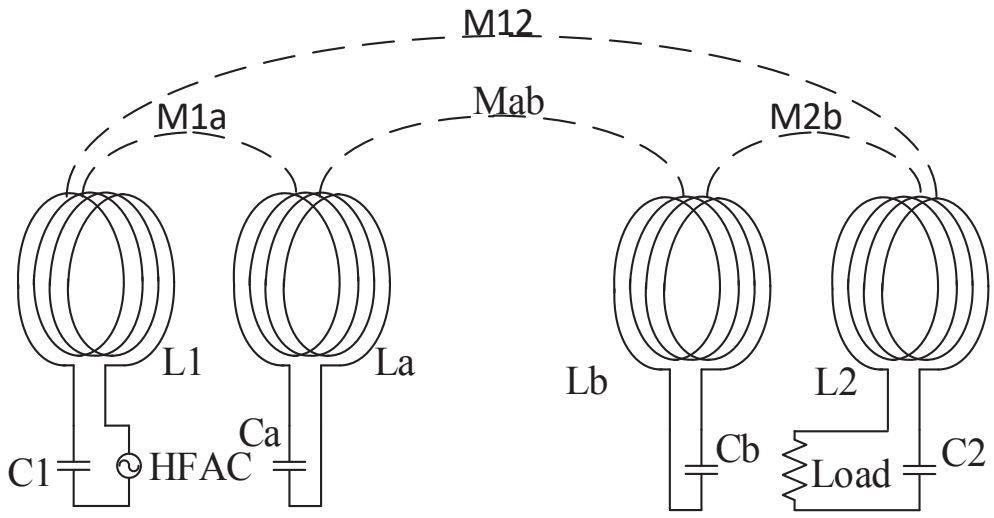

Fig. 4.4. General structure for four-coil system.

Table 4-1 Parameters of Simulated Coupler

Coil/Ferrite	Length [mm]	Turns
Coil 1-2	700×700	10
Coil a-b	400×48	10
Ferrite bar	186×28×16	n/a

4.3 Proposed Coupler with Assistive Coils

Since the wireless transformer is a loosely coupled transformer, the leakage flux is high. In order to reduce this, the magnetic field needs to be modified so that the flux linkage between two sides is increased and the leakage is reduced. To do this, a coupler with assistive coils is proposed, and this is shown in Fig. 4.5. Fig. 4.5(a) shows a 3D view, while Fig. 4.5(b) shows

the top view of the primary coupler and Fig. 4.5(c) shows a side view. Each side of the coupler has the major coil, four small assistive coils, and ferrite, which is used to help the flux linkage. The four assistive coils are connected in series or parallel, forming an assistive winding, which makes it a four-coil system. In this chapter, the SS connected compensation is analysed. The transformer is simulated in the ANSYS Maxwell 3D. The parameters for the transformer are shown in Table 4-1. The frequency of the system is set to 20 kHz; hence, ferrite and Litz-Wire are used to reduce eddy current loss.

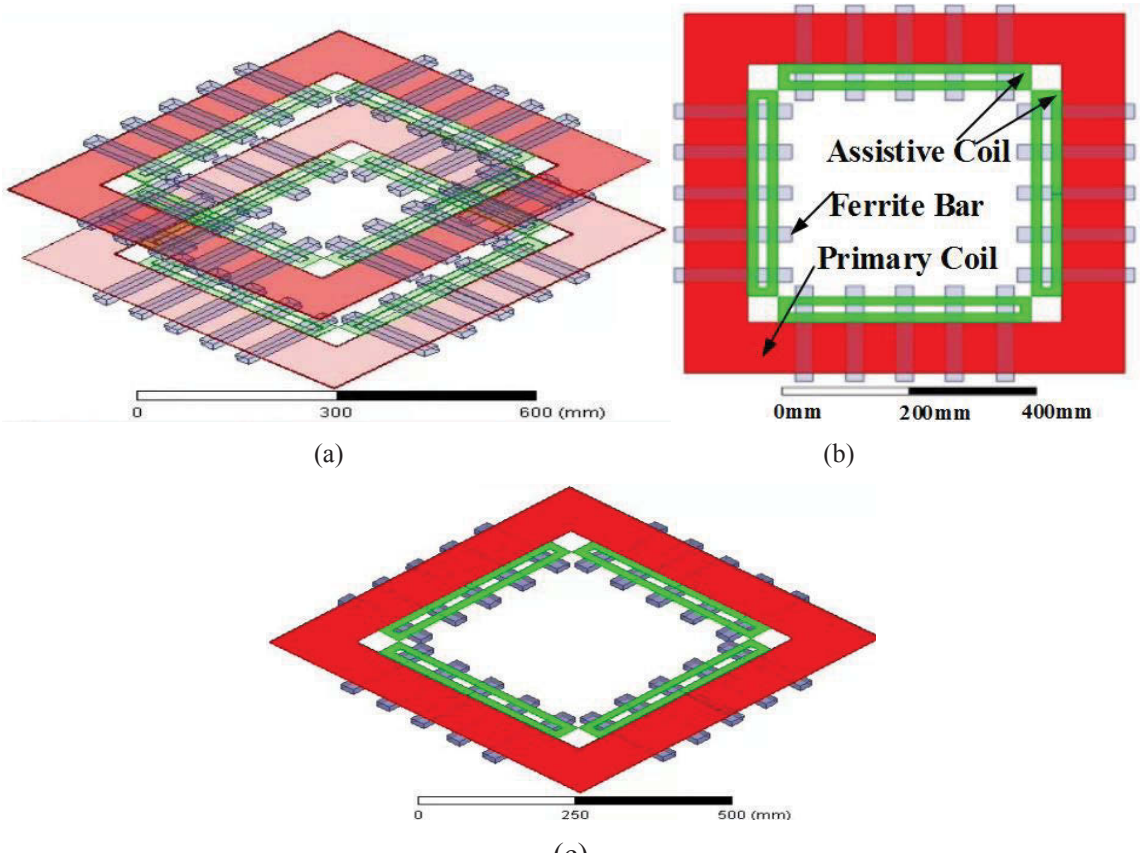

Fig. 4.5. General structure for four-coil system: a) 3D view of transformer; b) top view of primary coupler; c) side view of primary coupler.

4.3.1 Circuit Model for Proposed Coupler

Fig. 4.6 shows the circuit model for the coupler with the assistive coils. Four small coils on the primary side are series connected and form the assistive coil *La.* The secondary side has the assistive coil *Lb. La* and *Lb* are connected to capacitors *Ca* and *Cb*, respectively. The high frequency power is connected to the primary coil *L1* and compensation capacitor *C1*. The load is series connected to the secondary coil *L2* via capacitor *C2*. The mutual inductances between coils are shown as *M1a, M12, M1b, M2a, M2b, Mab. Mab* is the mutual inductance between coils a and b.

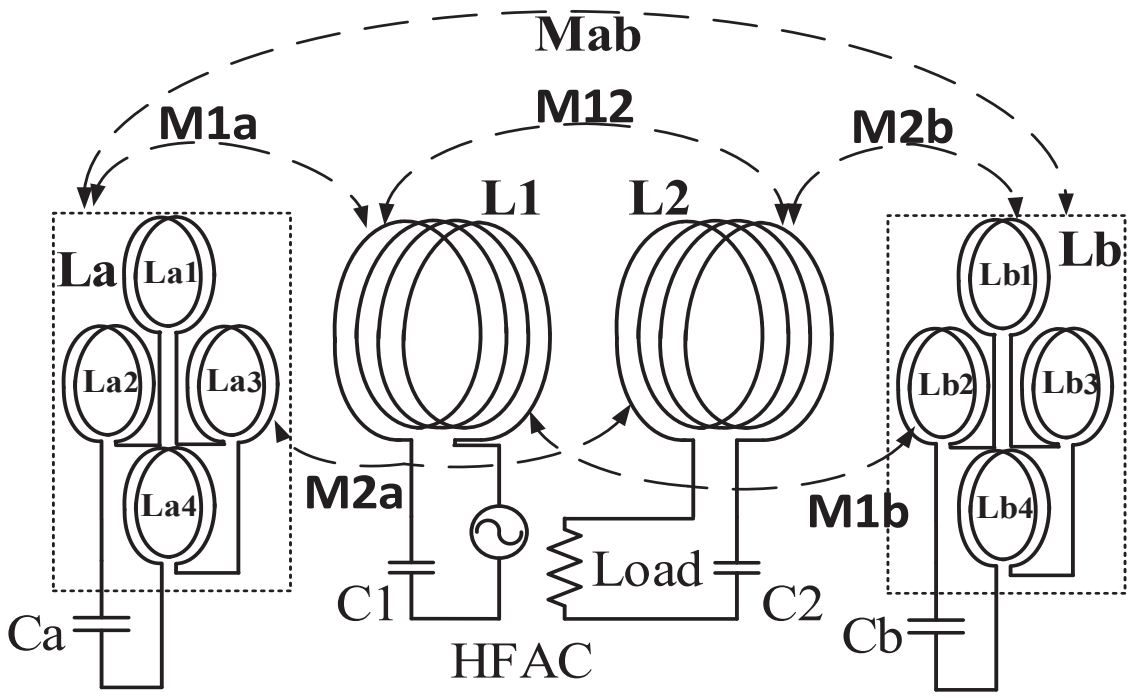

Fig. 4.6. Circuit model for proposed coupler with assistive coil system.

4.3.2 Simulation Results

A. FEA simulation result

The inductance matrix of the proposed system was simulated. The airgap distance between the primary and secondary coils is set to 200 mm in the FEA simulation, which is about 1/3 of the transformer length. The inductance matrix from the FEA simulation is shown in Table 4-2, and the coupling coefficient matrix is shown in Table 4-3.

Table 4-2 Inductance Matrix of Four Coils

Inductances [μH]	Coil 1	Coil 2	Coil 3	Coil 4
Coil 1	160	39.012	6.835	36.975
Coil 2	39.012	198.42	1.555	6.832
Coil 3	6.8352	1.555	198.42	38.993
Coil 4	36.975	6.832	38.993	160

For different working conditions, the airgap length varies. The coupling coefficient k for varying airgap length is shown in Fig. 4.7. The coupling between the primary and secondary windings decreases with increasing airgap. The k_{1a} between windings 1 and a is almost constant when the airgap is large. k_{1a} is higher than k_{2a} when the airgap is relatively small, which may be affected by the secondary side winding and ferrite. k_{2a} decreases with the

separation and its values are small beyond 150 mm, which means the coupling between the major coil and the assistive windings is weak.

Table 4-3 Coupling Coefficient Matrix of Four Coils

k	Coil 1	Coil 2	Coil 3	Coil 4
Coil 1	1	0.218	0.0383	0.230
Coil 2	0.218	1	0.00784	0.0382
Coil 3	0.038	0.00784	1	0.219
Coil 4	0.230	0.0383	0.21851	1

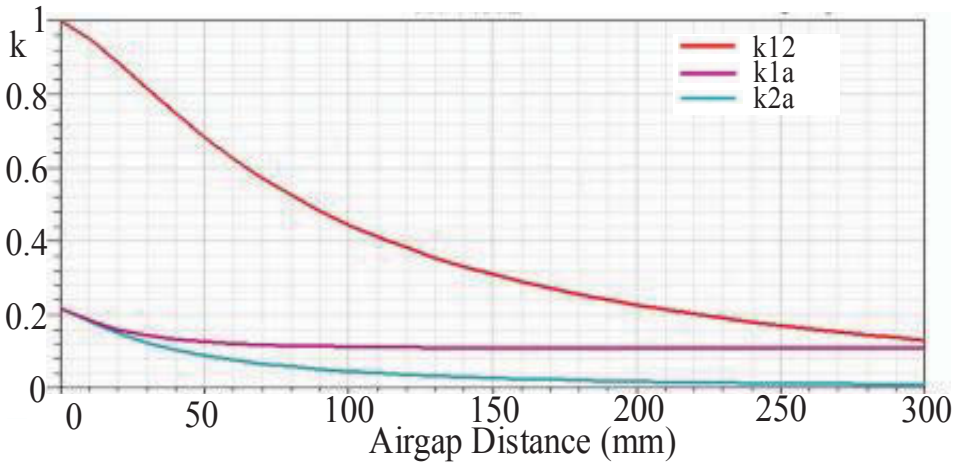

Fig. 4.7. Coupling coefficient via airgap length`

4.3.3 Circuit Analysis

With an ideal high frequency power source, the compensation capacitor affects the system characteristic. To estimate the output power and efficiency, it is important to simulate the compensation characteristic of the two-coil system and the proposed system. The circuit model in 4.2.1 simulates the two-coil system and the circuit model in Section 4.2.2 simulates the proposed system. The 700 mm square pads are used for both the two-coil and the proposed pads. The resonant capacitances for each winding at 20 kHz are normalised as *C1r, C2r, C3r*, and *C4r*.

A) Two-coil system with SS compensation

The performance of the two-coil system is different with different capacitor compensation connection. The series-series compensation is employed in both two-coil and proposed systems for comparison. The output frequency of the power source is set to 20 kHz. The inductance matrix in Table 4-2 for a 700 mm square pad with 150 mm airgap is used for the simulations. In the two-coil system, there are only primary coil and secondary coil capacitors, which are *C1* and *C4* for the convenience of comparison to the proposed four-coil system. The winding resistance is set to 0.09 Ω for all the windings.

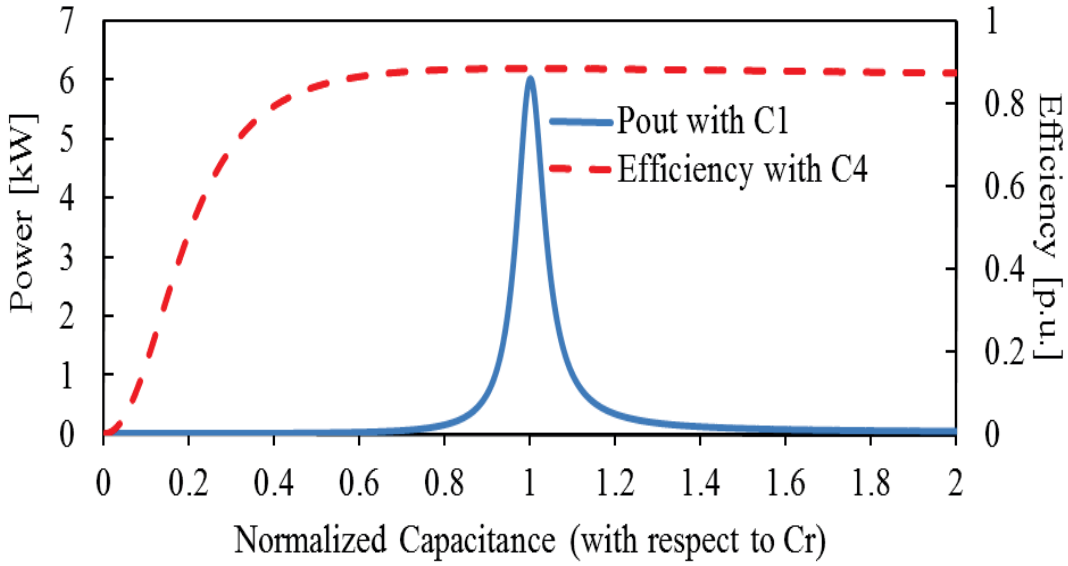

Fig. 4.8. Two-coil system characteristic with *C1* and *C4*.

The dash line in Fig. 4.8 shows the two-coil system efficiency with changing *C4* with fixed *C1* = *Cr* (resonance of *L1/C1* or *L4/C4*). The solid line shows the power output with changing *C1* with *C4* fixed at *Cr*. Both the maximum power and efficiency are reached around the *L1/C1* and *L4/C4* resonance points. However, the maximum overall system efficiency is lower than 0.9 in the two-coil system.

B) Four-coil system with SS compensation

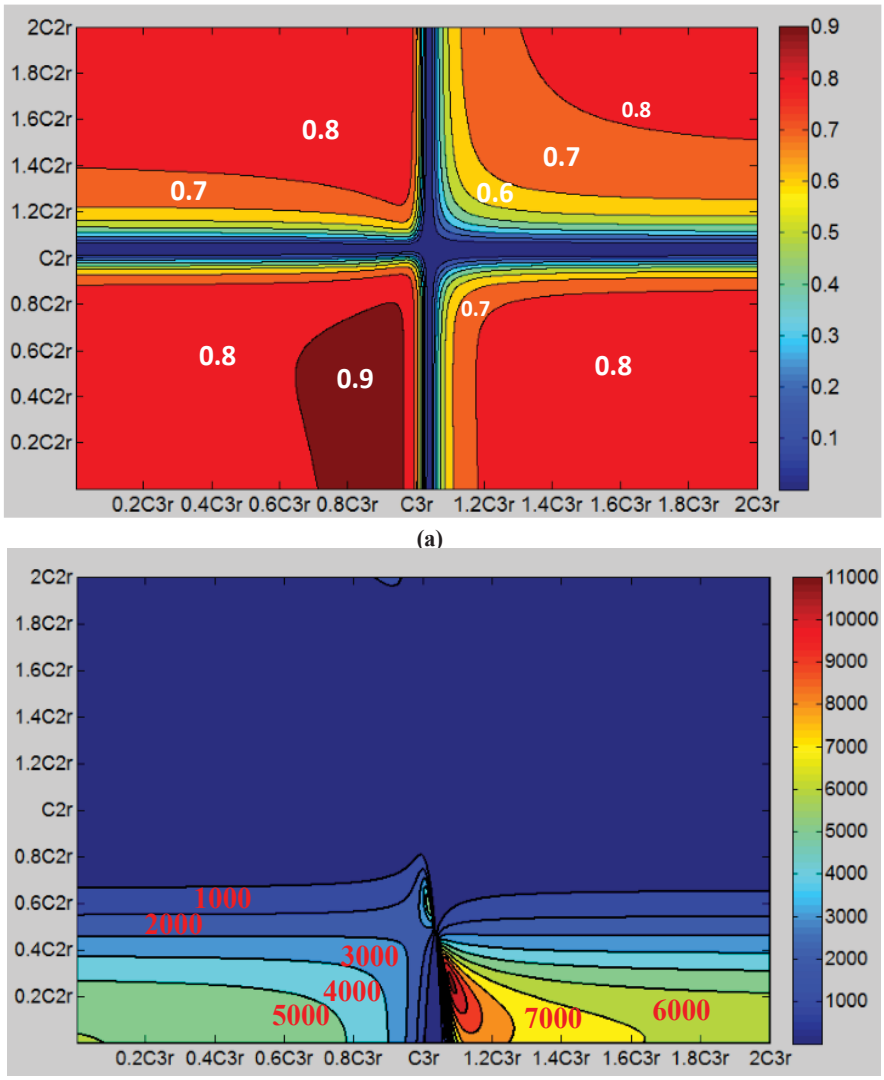

Fig. 4.9. Proposed coupler optimisation (efficiency and power maps).

The capacitor for the primary coil is *C1*, and that for the primary assistive coil is *C2*. The capacitor for the secondary assistive coil is *C3* and that for the secondary coil is *C4*. In the proposed system, the maximum overall efficiency is over 0.94 (Fig. 4.9). When the assistive coils are tuned to resonate at the source frequency, higher power is transferred to the assistive coil compared to the load side. The power is consumed by the parasitic resistance which causes a cross-shaped low efficiency region as shown in Fig. 4.9(a). The highest efficiency

region is on the bottom left, close to *C3r*. The highest power transfer region, which reaches 11 kW, is on the bottom right, close to *C3r*. The highest efficiency region can transfer 1 to 5 kW, which is sufficient for a level 1 or 2 EV charger. The primary compensation capacitor has a higher impact on power transfer compared to the secondary side because only part of the primary coil flux links the secondary coil; hence, the power map is not symmetrical. The maximum power and efficiency regions are still slightly away from each other, but in the > 90 % efficiency area, the power is up to 5 kW, which is higher than the two-coil SS compensation system.

4.4 Summary

In this chapter, the two-coil and four-coil structure IPT couplers are first reviewed. The coupler with assistive coils is then proposed. In order to transfer power to an EV with high efficiency, the wireless transformer needs to be designed properly. The FEA simulation is employed and followed by circuit analysis for the proposed geometry. The proposed system is capable of transferring 1 to 5 kW power with over 90% efficiency.

4.5 References

[4.1] S. Y. R. Hui, W. Zhong, and C. K. Lee, "A critical review of recent progress in mid-range wireless power transfer," IEEE Trans. Power Electron., vol. 29, pp. 4500-4511, 2014.

[4.2] C. Wang, O. H. Stielau, and G. A. Covic, "Design considerations for a contactless electric vehicle battery charger," IEEE Trans. Ind. Electron., vol. 52, pp. 1308-1314, 2005.

[4.3] M. Budhia, J. T. Boys, G. A. Covic, and C. Y. Huang, "Development of a single-sided flux magnetic coupler for electric behicle IPT charging systems," IEEE Trans. Ind. Electron., vol. 60, pp. 318-328, 2013.

[4.4] S. Wang and D. G. Dorrell, "Loss analysis of circular wireless EV charging coupler," IEEE Trans. Magn., vol. 50, article 8402104, 2014.

[4.5] W. Shuo and D. G. Dorrell, "Review of wireless charging coupler for electric vehicles", Proc. IEEE 39th Annu. Conf. Ind. Electron. Soc. (IECON), pp. 7274-7279

[4.6] F. Musavi, M. Edington and W. Eberle, "Wireless power transfer: A survey of EV battery charging technologies", Proc. IEEE ECCE, pp. 1804-1810.

[4.7] G. A. Covic, M. L. G. Kissin, D. Kacprzak, N. Clausen and H. Hao, "A bipolar primary pad topology for EV stationary charging and highway power by inductive coupling", Proc. IEEE ECCE, pp. 1832-1838.

[4.8] Y. H. Kim, S. Y. Kang, S. Cheon, M. L. Lee, J. M. lee, and T. Zyung, "Optimization of wireless power transmission through resonant coupling," in Proc. SPEEDAM 2010, 2010, pp. 1069-1073.

[4.9] S. Cheon, Y. H. Kim, S. Y. Kang, M. L. Lee, J. M. Lee, and T. Zyung, "Circuit-model-based analysis of a wireless energy-transfer system via coupled magnetic resonances," IEEE Trans. Ind. Electron., vol. 58, pp. 2906-2914, 2011.

[4.10] P. Si, A. P. Hu, J. W. Hsu, M. Chiang, Y. Wang, S. Malpas, et al., "Wireless power supply for implantable biomedical device based on primary input voltage regulation", *Proc. 2nd IEEE Conf. Ind. Electron. Appl.*, pp. 235-239.

[4.11] A. Kurs, A. Karalis, R. Moffatt, J. D. Joannopoulos, P. Fisher, and M. Soljačić, "Wireless power transfer via strongly coupled magnetic resonances," Science, vol. 317, pp. 83-86, 2007.

[4.12] Q. Zhu, L. Wang, and C. Liao, "Compensate capacitor optimization for kilowatt-level magnetically resonant wireless charging system," IEEE Trans. Ind. Electron., vol. 61, pp. 6758-6768, 2014.

Chapter 5

IPT System Analysis

In order to achieve high efficiency performance for IPT system, it is necessary to study the operating mechanism, which will provide insight into the characteristics. As stated in chapter 3, the IPT system has HF inverter, wireless transformer/coupler, and rectifier. The IPT system will be analysed on circuit level in this chapter.

There are primary side and secondary side of IPT system, and they are separated without wire connections. Different control strategies were proposed based on the characteristic. In [5.1-5.4], the separated single control was employed. The separated single side control methods control primary side and secondary side separately. And the control for each side doesn't require feedback from the other side. In [5.2], the primary side control uses frequency control and secondary side regulates the received power to the load. The separated single side control doesn't require wireless signal transfer devices. However, it is not possible for bidirectional power flow with this control as cooperation between primary side and secondary side is necessary in bidirectional power transfer. The dual side controls were proposed for bidirectional power flow for IPT applications in [5.5-5.10]. In [5.10], dual side phase shift has been employed with full bridge inverter on both side.

5.1 Circuit Analysis with Compensation

5.1.1 System efficiency relationship with Rload.

From the equivalent circuit, the input power from the HF power sources is,

$$P_{in}(R_L, X_L) = \frac{V_i^2[R_p + Re(Z_{21})]}{|Z_p + Z_{21}|^2} \tag{5.39}$$

From equation (3.17), the output power of the SS compensated circuit is

$$P_{out}(R_L, X_L) = \frac{X_m^2 V_i^2 R_L}{|Z_c|} = \frac{(\omega M)^2 V_i^2 R_L}{|Z_c|} = \frac{\omega^2 V_i^2 k L_1 L_2 R_L}{|Z_c|} \tag{5.40}$$

where

$$Z_c = (Z_p + Z_{21})^2 (Z_s + Z_L)^2 \tag{5.41}$$

For a given coupler and power source, the input voltage *Vi*, coupling coefficient *k*, primary and secondary inductances L_1 and L_2 are fixed. Therefore, for a certain load R_L, the maximum power output is reached when Z_c is minimized.

$$\eta = \frac{P_{out}}{P_{in}} = \frac{X_m^2 R_L}{(Z_s+Z_L)^2[R_p+Re(Z_{21})]} = \frac{X_m^2 R_L}{(Z_s+Z_L)^2[R_p+Re(\frac{X_m^2}{Z_s+Z_L})]} =$$

$$\frac{X_m^2 R_L}{[(R_s+R_L)^2+(X_s+X_L)^2](R_p+\frac{X_m^2(R_s+R_L)}{(R_s+R_L)^2+(X_s+X_L)^2})} =$$

$$\frac{X_m^2 R_L}{[(R_s+R_L)^2+(X_s+X_L)^2]\, R_p+X_m^2(R_s+R_L)} \tag{5.42}$$

In case to working at the maximum efficiency point, the reactive part in secondary side should be cancelled, i.e. $X_s+X_L = 0$. For a given capacitor, the power source frequency should be at the resonance frequency of the secondary side for the maximum efficiency consideration.

The load for maximum system efficiency is yielded when [1],

$$\mathrm{R}_{Load,opt} = \sqrt{R_s^2 + \frac{R_s}{R_p} X_m^2} \tag{5.43}$$

The system efficiency is simulated in the MATLAB using the parameters in Table 5-1. From the equation, the maximum efficiency is supposed to occur at 4.80 Ohms. The simulation result is shown in Fig. 5.1. From the figure, the system efficiency firstly increases with the increase of load resistance. After reaching the optimum load for maximum efficiency point, the system efficiency decreases gradually. The system efficiency is sensitive to the load variation around the optimum point.

Table 5-1 Parameters for Efficiency Analysis

f(Hz)	20,000
R_p (ohm)	0.4
Mutual Inductance (mH)	38.82
R_{load} (ohm)	1-10

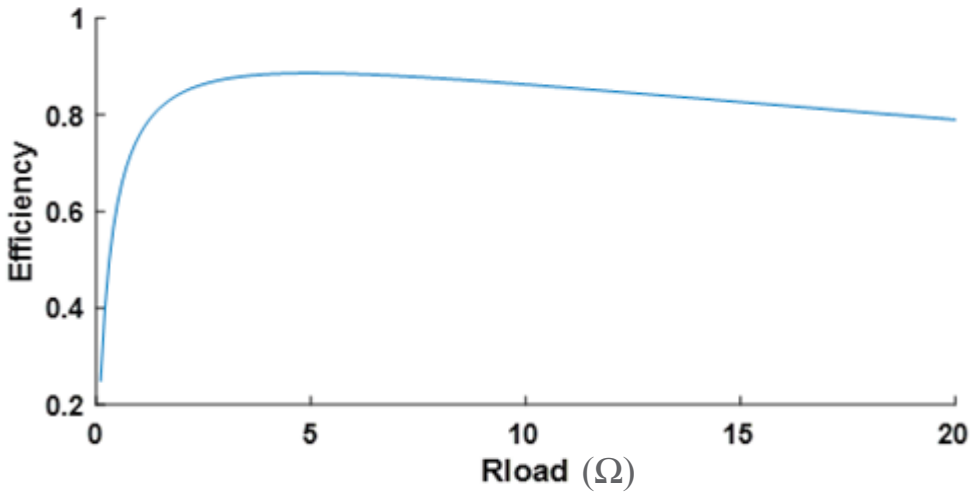

Fig. 5.1. Efficiency versus R_{load}.

5.1.2 Secondary Side Output Current

The currents in primary and secondary windings are shown in (3.15) and (3.16), and the secondary side current could be further expressed as

$$I_s = \frac{j\omega M I_p}{Z_s + Z_L} = \frac{j\omega M}{Z_s + Z_L} \frac{V_i}{Z_p + Z_{21}} \tag{5.44}$$

As stated in the previous part, the maximum efficiency is reached at the secondary side resonance frequency, and the reactive part is eliminated in Z_s. In order to acquire unity power factor, the primary side reactive part should be cancelled as well. The secondary side current is

$$I_s = \frac{j\omega M V_i}{R_p(R_s + R_L) + (\omega M)^2} \tag{5.45}$$

When the quality factor Q is high in the IPT system, $R_p(R_s + R_L)$ is much smaller than $(\omega M)^2$. Assume the frequency of the power source is in high frequency region, the angular frequency ω is high, and $(\omega M)^2 \gg R_p(R_s + R_L)$, therefore $R_p(R_s + R_L)$ part could be neglected, and the secondary side current is

$$|I_s| = \frac{V_i}{\omega M} \tag{5.46}$$

The secondary side current performs as current source in this case. The current in the secondary side has nearly linear relationship to the input voltage.

5.1.3 Efficiency with the Mutual Inductance

The system efficiency is

$$\eta = \frac{X_m^2 R_L}{(R_s+R_L)^2 R_p + X_m^2 (R_s+R_L)} \tag{5.47}$$

And from

$$\frac{1}{\eta} = \frac{(R_s+R_L)^2 R_p}{X_m^2 R_L} + \frac{R_L(R_s+R_L)}{R_L} \tag{5.48}$$

it can be seen that the system efficiency increases with increasing mutual inductance. This shows that smaller airgap for certain pad design would give a better system efficiency. From the pad design point of view, the mutual reactance should be as high as possible.

The simulation results are shown in Fig. 5.2. The system efficiency is as depicted, which increases with the increase of mutual inductance. At the same time, as the simulation parameters are the same as those in Table 5-1. For the same mutual inductance, the system efficiency with optimal load R_{load} has higher efficiency than other load resistance.

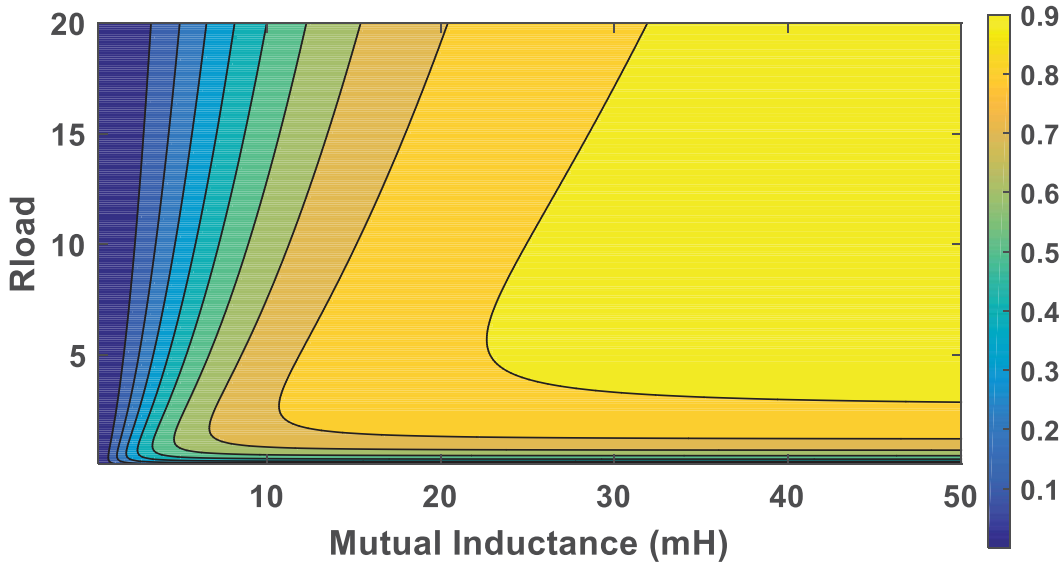

Fig. 5.2. Efficiency map of mutual inductance and Rload.

5.1.4 IPT System Performance versus Frequency

When the coupler and airgap distance is set up, the optimal capacitance of the compensation capacitors could be calculated by setting the secondary side resonance frequency to equal the power source frequency. The HF power source frequency may vary around the secondary side resonance frequency, and therefore, for the given system, the frequency response is simulated. The simulation model in chapter 4 for the two-coil system is employed. The simulation parameters are shown in Table 5-2.

Table 5-2. Frequency Analysis Parameters

Primary and Secondary Inductances	200 μH
Mutual Inductance	38.82 uH
Primary and Secondary Capacitances	330 nF
Primary and Secondary Winding Resistances	0.4 Ohm
R_{load}	3.5 Ohm
Vin	50 V
Frequency Range	0-40 kHz

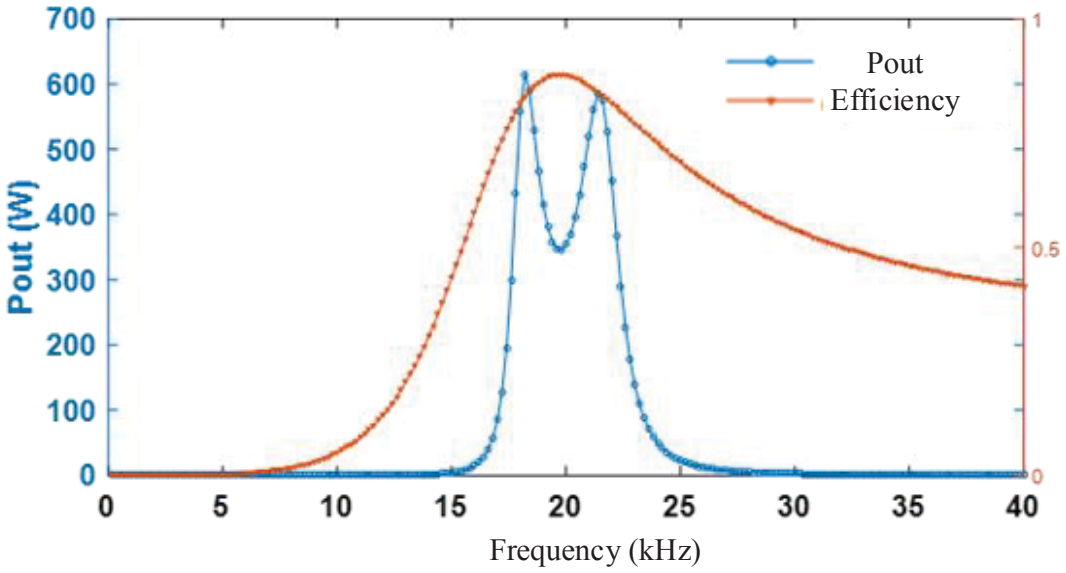

Fig. 5.3. Pout and efficiency versus HF power source frequency

The simulation results are shown in Fig. 5.3. There is only one highest efficiency operating point, which is around the secondary side resonance frequency f_2. There is power bifurcation phenomenon in this simulation. There are two power output peak points: one is at the lower frequency side of f_2 and the other is at the higher frequency side. The output power at f_2 is a local low output.

5.1.5 Impedance Analysis

With the parameters in Table 5-3, the input frequency analysis for AC power input was performed. The frequency analysis of the circuit is shown in Fig. 5.4.

The input impedance *Zin* is low around the nominal frequency 20 kHz. The power output reaches the unity power factor at the resonance frequency. For a power source with internal

resistance, the maximum power output is reached when Zin is equal to the source internal resistance *Rs*.

Table 5-3 Parameters of the IPT system

Nominal frequency	20 kHz
L_1 and L_2 (uH)	200
M (uH)	38.82
C_1 and C_2 (uF)	0.33
R_1 and R_2 (Ohm)	0.4
R_{load} (Ohm)	10

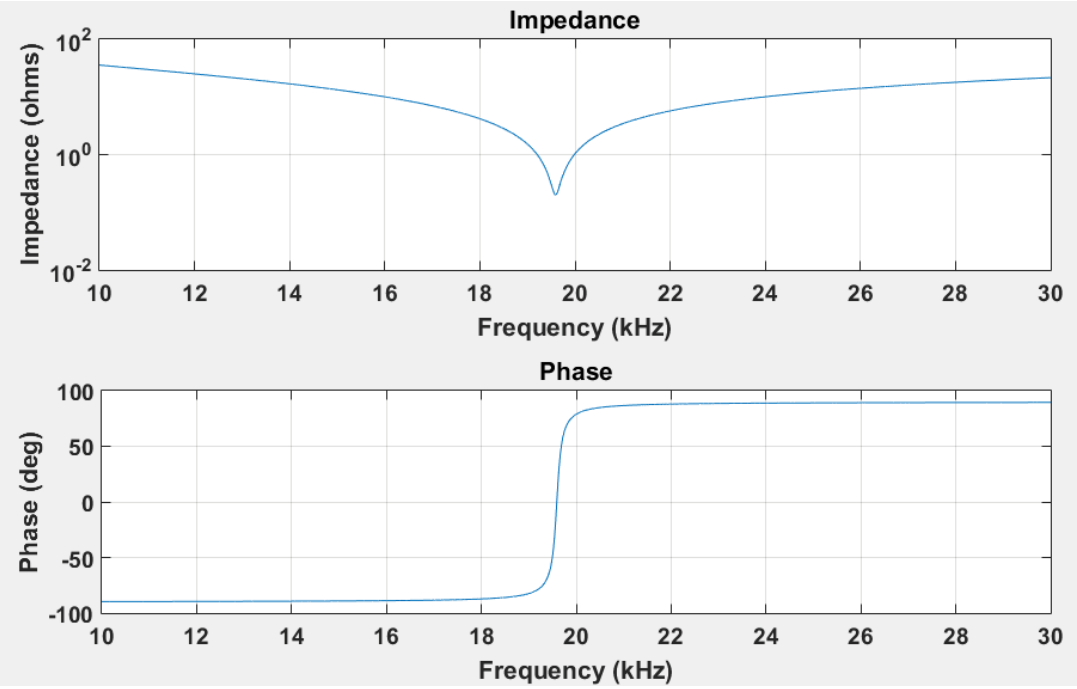

Fig. 5.4. The frequency analysis: a) impedance verse frequency, b) Phase angle versus frequency

5.2 System Simulation

5.2.1 DC Input Simulation

With the parameters defined in Table 5-1, the simulation model was built in MATLAB/SIMULINK as shown in Fig. 5.5. The input is a DC voltage source, followed by a full bridge IGBT inverter. The primary side of the coupler is connected to the output of the full bridge inverter. The secondary side of the coupler is connected to a full bridge diode rectifier. A resistant load is connected to the DC side of the rectifier.

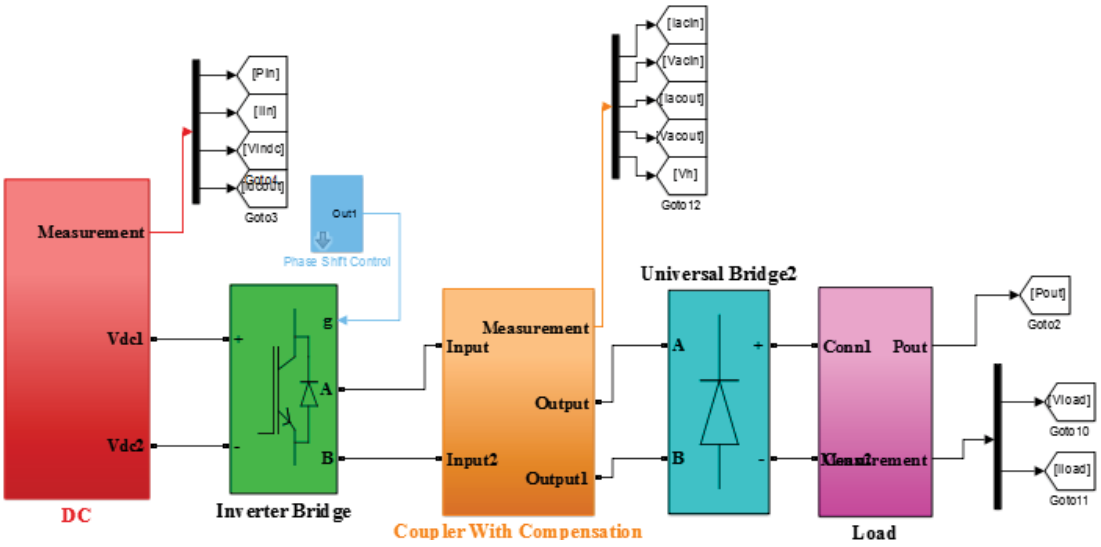

Fig. 5.5. IPT system simulation model

The DC power source voltage is 70 V. By changing the phase shift angle between the two bridge legs, the output power could be controlled.

5.2.2 Full bridge Inverter

In order to supply high frequency AC power to the coupler, the grid current is rectified and it charges a large capacitor which can be considered as a DC voltage source. The DC voltage source is then connected to the primary side of the coupler via a DC-AC converter. The secondary side of the converter is connected to another rectifier to convert the high frequency AC to DC to charge the battery. The transfer system from primary side capacitor to secondary side battery part can be modelled as a DC-DC converter.

The full bridge DC-DC converter is shown in Fig. 5.6. By using IGBT/MOSFET for full bridge on both sides, the IPT system could achieve bidirectional power transfer. In this

research, only power flow from the primary side to the secondary side is considered. However, as the system is symmetrical, the bidirectional power flow is possible.

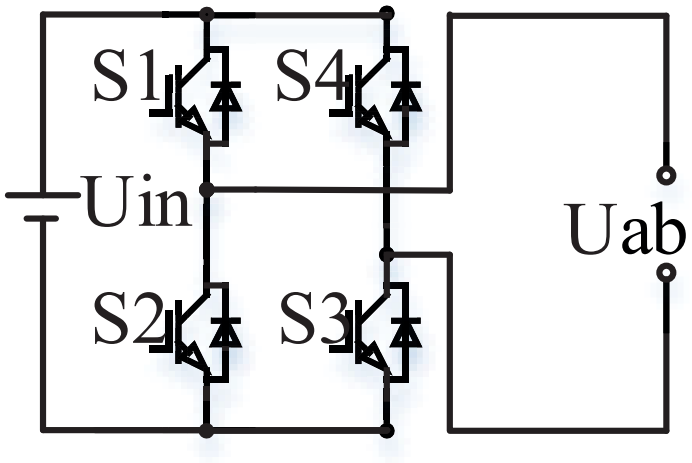

Fig. 5.6. Full bridge inverter.

5.2.3 Phase shift Control

The phase shift control is employed for the full bridge. The advantages of the phase shift control are the simplicity and low switching frequency for IGBT/MOSFET. There are other modulation methods for the full bridge control. However, due to the high system frequency for IPT applications, which is generally within 10-100 kHz, the switching loss of using complex modulation methods would be significant for the Si based devices. It is possible to employ other modulation methods with SiC or GaN devices. In this research, the inverter is Si based IGBT, and the phase shift control is chosen.

The waveform for the phase shift control is shown in Fig. 5.7. The driving signals for IGBT S1, S2, S3 and S4 are square waves with 50% duty cycle. The gate signals for S1 and S2 are opposite. The gate signal for S1 is 15 V when the gate signal for S2 is 0. The gate signals for

S3 and S4 are opposite as well. The phase shift angle α is defined as the overlap angle between S1 and S2 from the position where both S1 and S2 are switched on as shown in Fig. 5.7. ω is the angular frequency of the driving signal.

Using the Taylor's series, the first harmonic amplitude of output voltage with respect to phase shift angle α is

$$V_{out.k} = \frac{4V_{DC}}{\pi}(\sin\frac{\alpha}{2}) \tag{5. 49}$$

The maximum output voltage is $\frac{4V_{DC}}{\pi}$ when the phase shift angle is π, and the minimum output voltage is 0 when the phase angle is 2π.

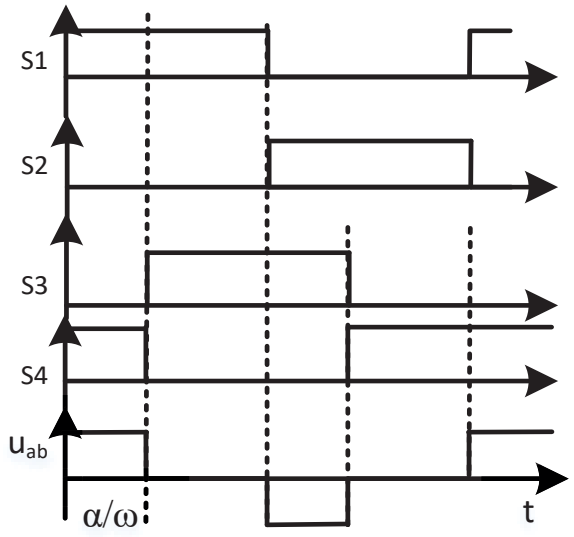

Fig. 5.7. The phase shift control for full bridge Inverter.

5.2.4 IPT System Simulation Results

A) Phase Shift α =180 Degrees

The output voltage and current of the inverter with phase shift angle 180 degrees are shown in Fig. 5.8. The inverter output is almost with unity power factor. The load voltage and current are shown in Fig. 5.9. As the compensation capacitor C and winding inductance L form a bandpass filter, the output voltage on the load is sinusoidal. In Fig. 5.10, the waveform on the top is the output power to the load, and the bottom waveform is the input power from the DC power source. The efficiency at this phase shift angle is 80.3%.

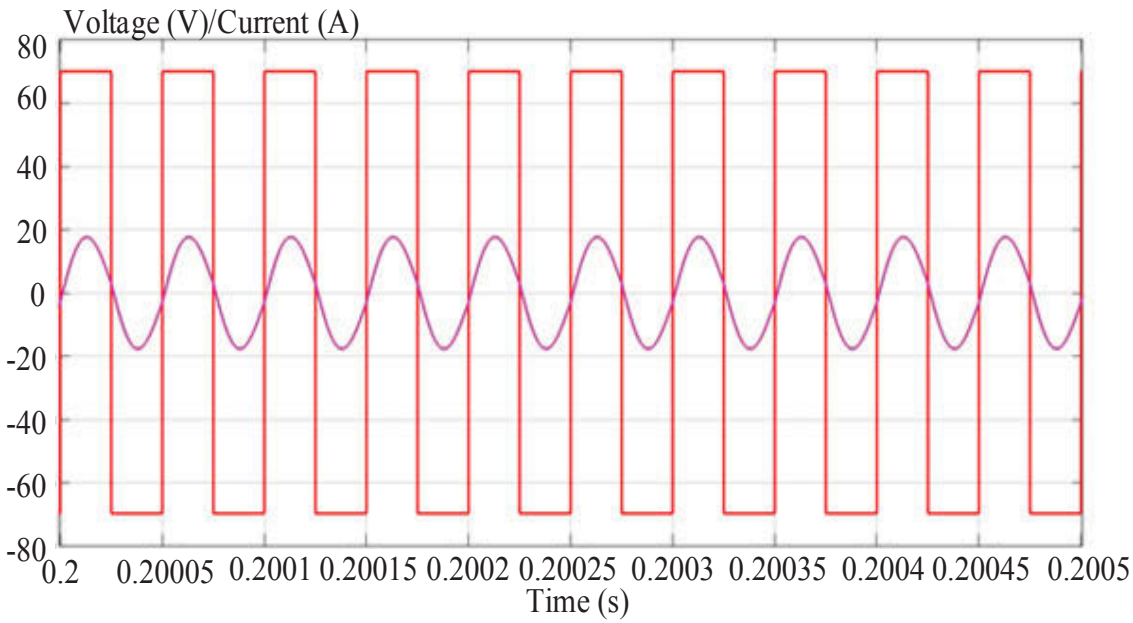

Fig. 5.8. Full bridge output voltage and output current

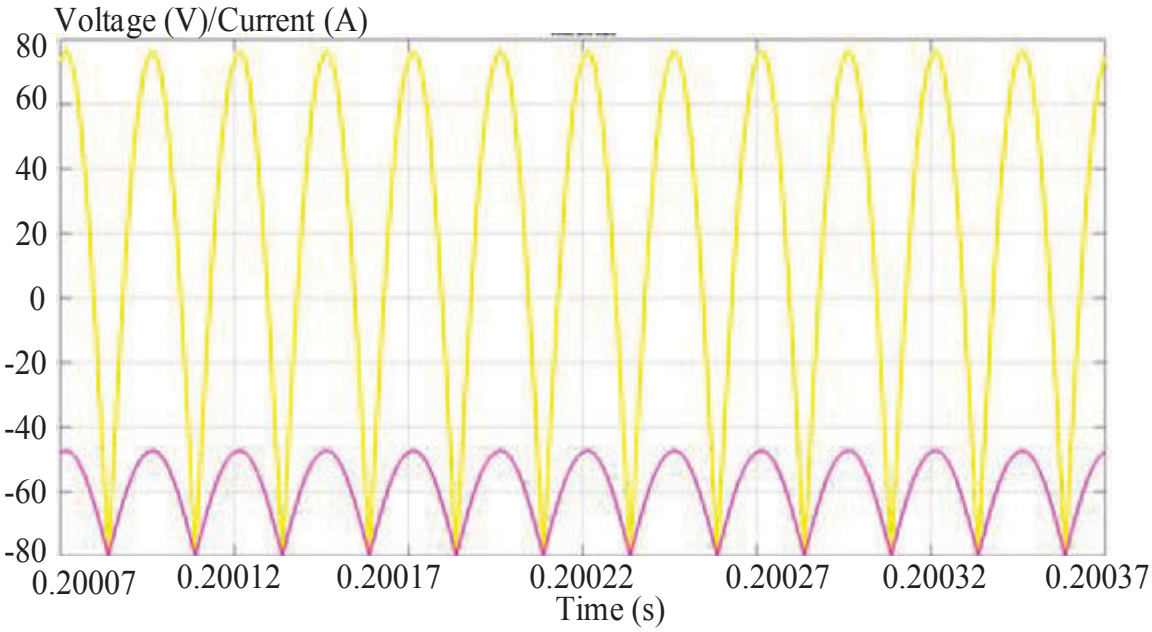

Fig. 5.9. Load voltage V_{load} and current I_{load}.

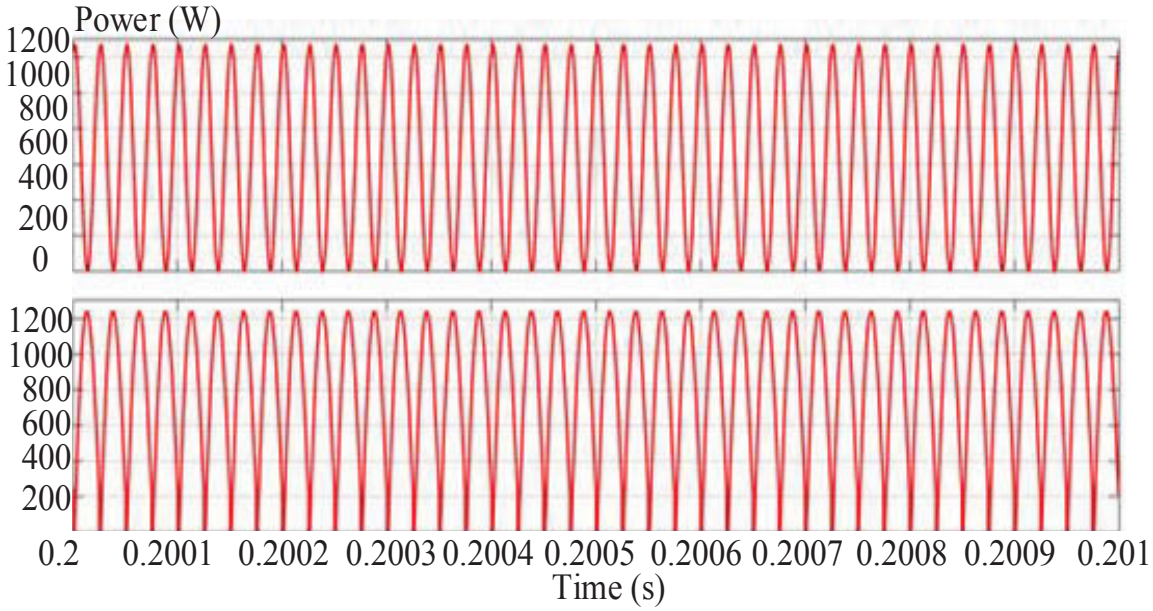

Fig. 5.10. Output power (top) and input power waveforms (bottom).

B) Phase Shift of 120 degrees

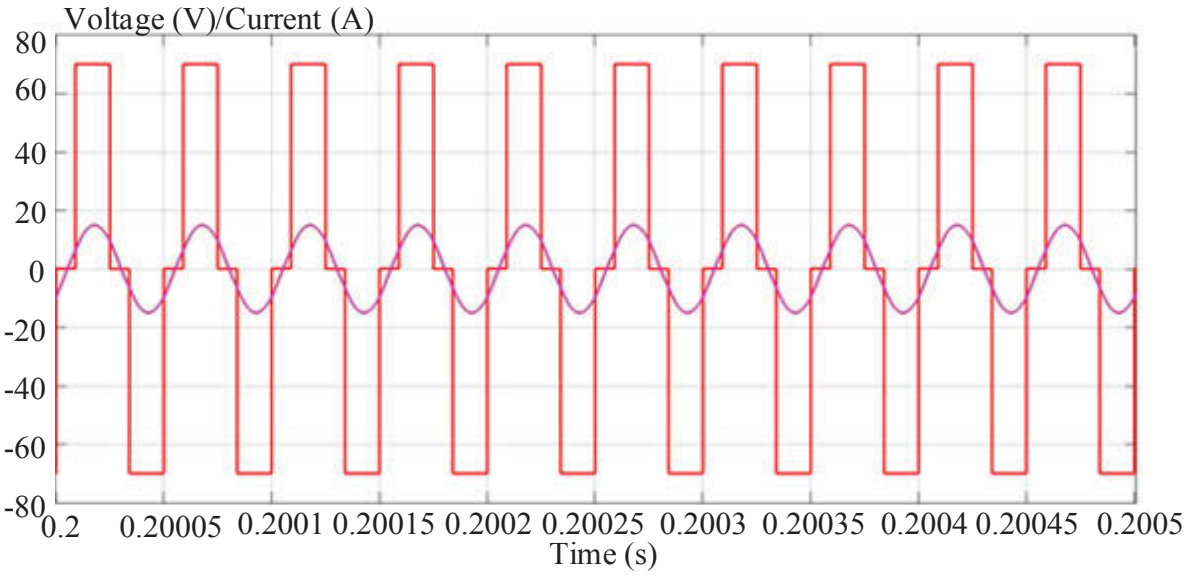

Fig. 5.11. Inverter output voltage and current at α =120.

The output voltage and current of the inverter with phase shift angle of 120 degrees are shown in Fig. 5.11. The unity power factor output is almost reached as the first harmonic of voltage at α =120^{o} has the same frequency as that at α =120^{o}. In Fig. 5.12, the waveform on the top is the output power to the load and the bottom waveform is the input power from the DC power source. The input power waveform is non-sinusoidal, and this is due to that the power is only transferred when the inverter has output voltage. In the experiment system, this causes fluctuation of the DC bus voltage as the capacitor is used to regulate the voltage.

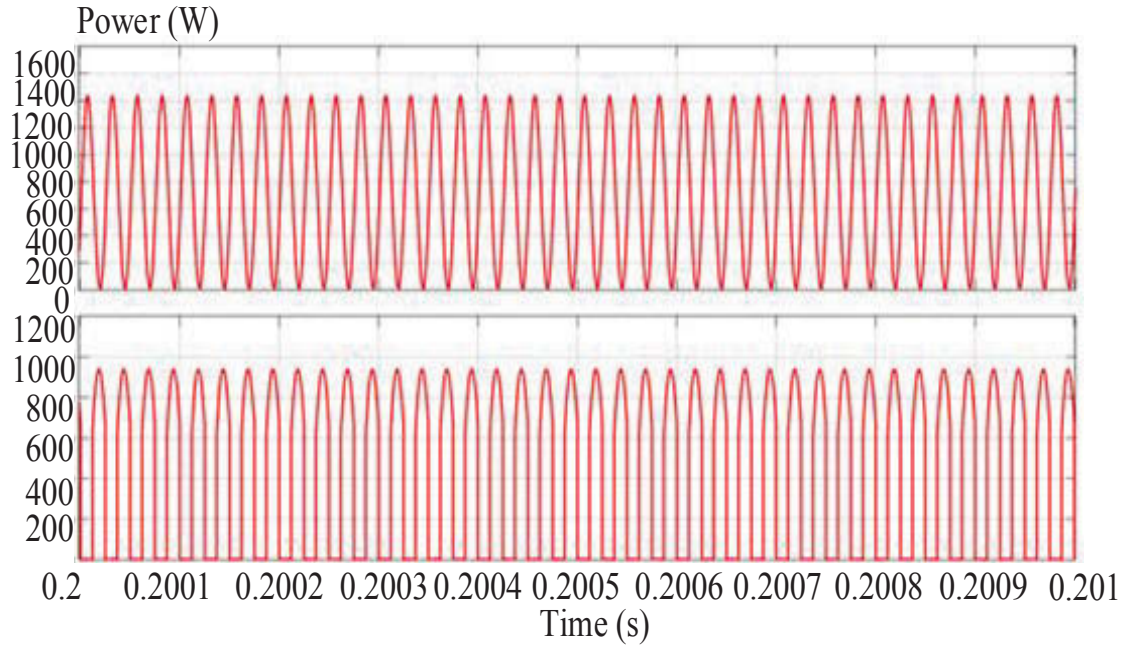

Fig. 5.12. Output power (top) and input power waveforms at $\alpha = 120^{o}$.

C) Simulation With Different Phase Shift Angles

Table 5-4. Output Power with Phase Shift Angle

Phase shift Angle (Degree)	Pout (W)	Pin (W)
180	647.9	806.4
150	600.6	736.6
120	496.6	597.4
90	317.5	386.48

With the same DC voltage of 70 V, the IPT system with different phase shift angles is simulated. The input and output powers are shown in Fig. 5.13 and Table 5-4. From the figure,

it can be seen that the output power decreases with the increasing phase shift angle, and reaches the maximum power output at 180 degrees, which is the maximum phase shift angle.

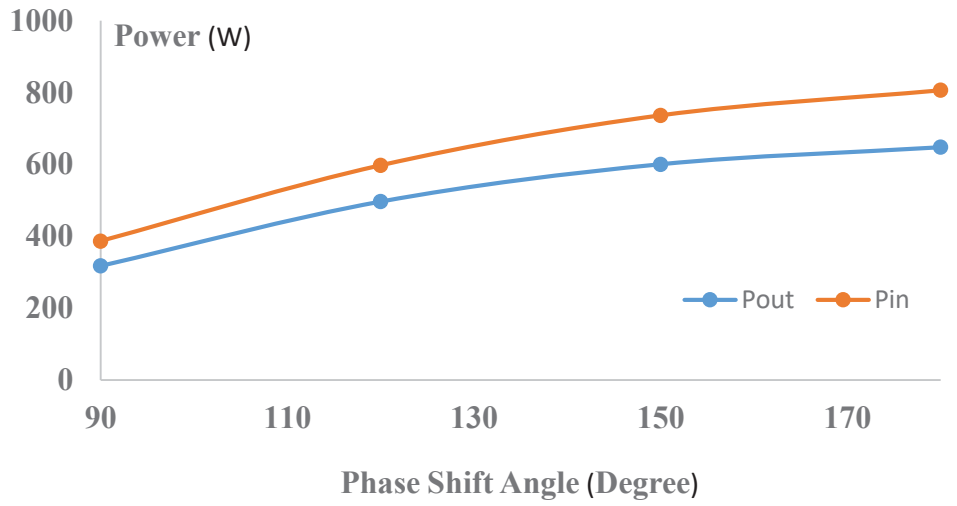

Fig. 5.13. Output power and input power versus phase shift angle

The efficiency η of the system is calculated from

$$\eta = \frac{\int_{t_0}^{t} P_{out} dt}{\int_{t_0}^{t} P_{in} dt} = \frac{\int_{t_0}^{t} V_{load} I_{load} dt}{\int_{t_0}^{t} V_{in} I_{in} dt} \tag{5.50}$$

where Vload and Iload are the voltage and the current of the load. Vin and Iin are the voltage and output current of the DC power source, respectively.

In the system analysis, the input AC power source has sinusoidal voltage output, the frequency of which is the 1st harmonics of the square wave from phase shift control. The phase shift changes other harmonic components which would has impact on the system efficiency. Also, the phase shift angle, which changes the switching loss in the inverter, has

impact on the efficiency as well. The system efficiency versus phase shift angle is as shown in Fig. 5.14.

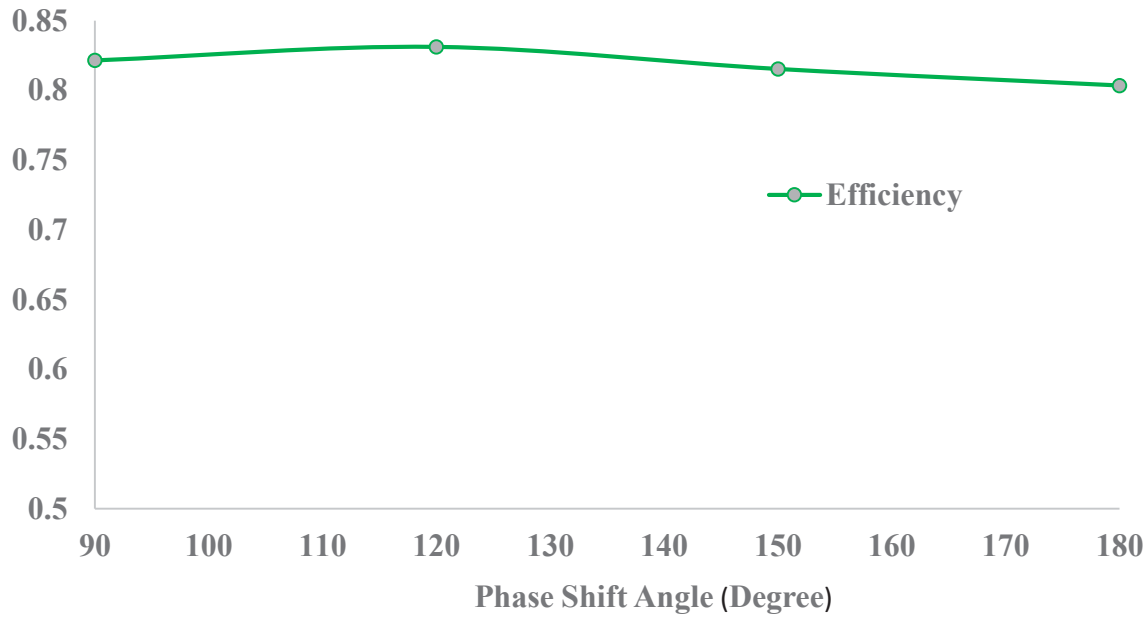

Fig. 5.14. Efficiency versus phase shift angle.

5.2.5 Charger with Three Phase AC Source Simulation Results

Level 2 chargers would be the major choice for commercial parking or recharging stations, where the 3-phase power source is available with higher power ratio. The simulation model for IPT system with three phase power input is shown in Fig. 5.15. The power source is connected to the DC link capacitor via three phase diode bridge rectifier. The rest of the system is the same as the DC power source simulation.

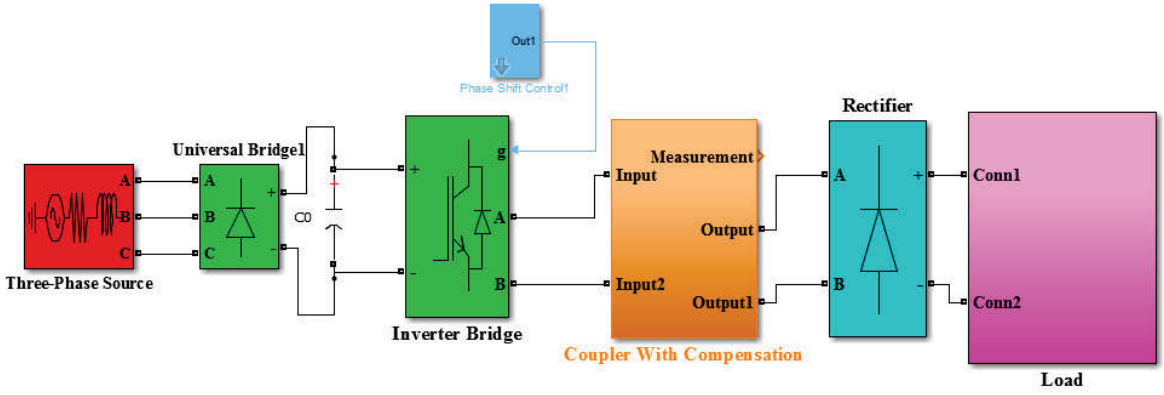

Fig. 5.15. Simulation model of IPT system with three phase input.

The phase shift angle in this simulation is 180 degrees. The output current and voltage of the three phase rectifier are shown in Fig. 5.16 and Fig. 5.17 respectively. The voltage reaches 70 volts after 0.03 s, and the current is about 12 A with ripple at the same time.

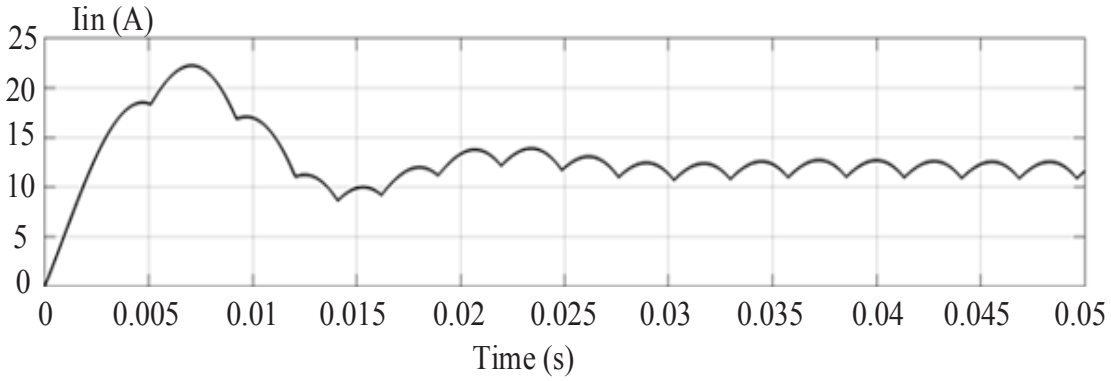

Fig. 5.16. Output current of three phase rectifier.

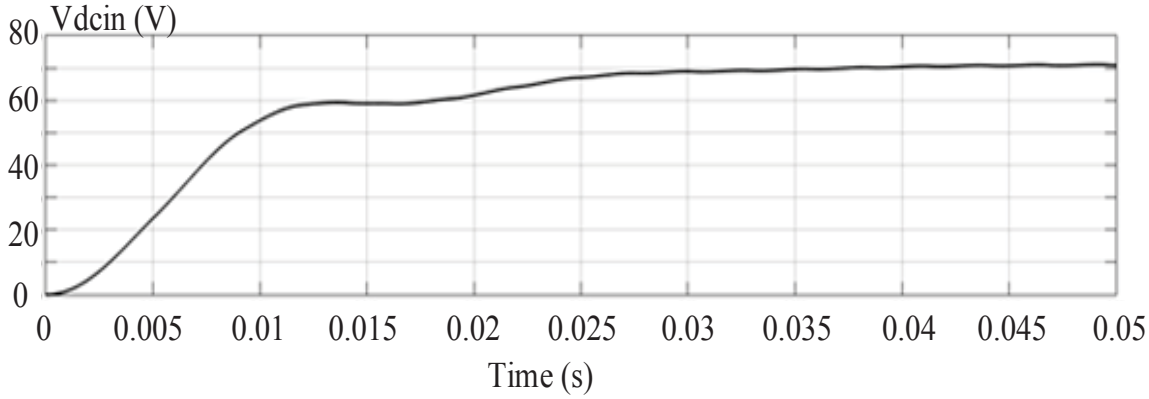

Fig. 5.17. Three phase rectifier DC link voltage.

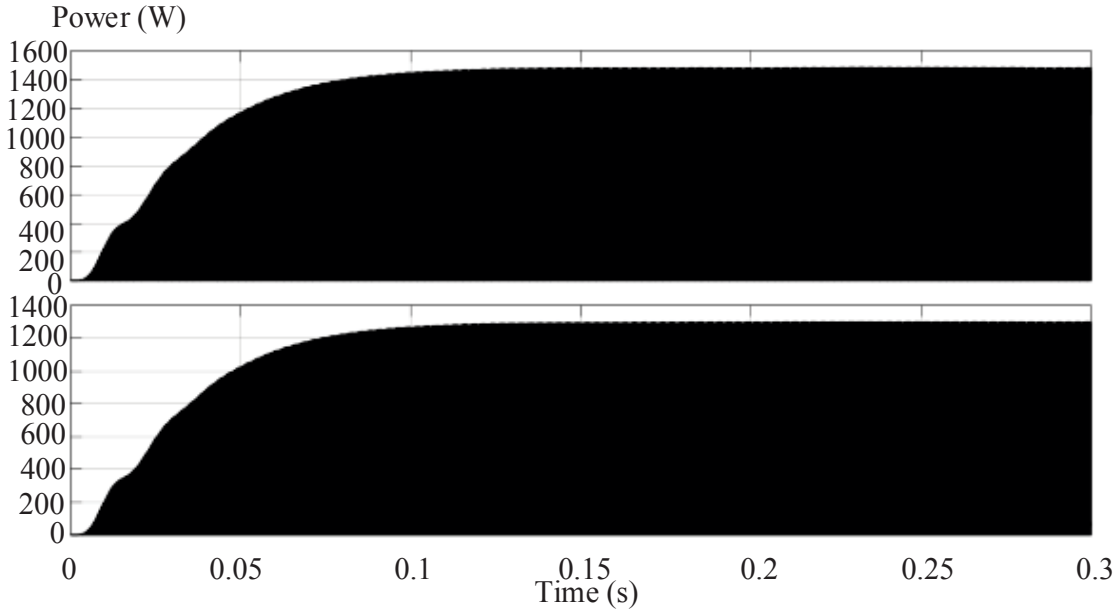

Fig. 5.18. Three phase IPT system input power and output power.

The input and output powers are shown in Fig. 5.18. The efficiency of the IPT system is 81.1 %.

5.3 Experiment

The IPT experiment circuit is shown in Fig. 5.19. The rectifier is connected to the grid via a VARIAC, which is used to control the DC link voltage Vin. The DC side of the IGBT full bridge inverter is connected to the DC link of rectifier, and AC side is connected to the primary side of the coupler via a series connected capacitor. The load is connected to the secondary side of the coupler via a series connected capacitor.

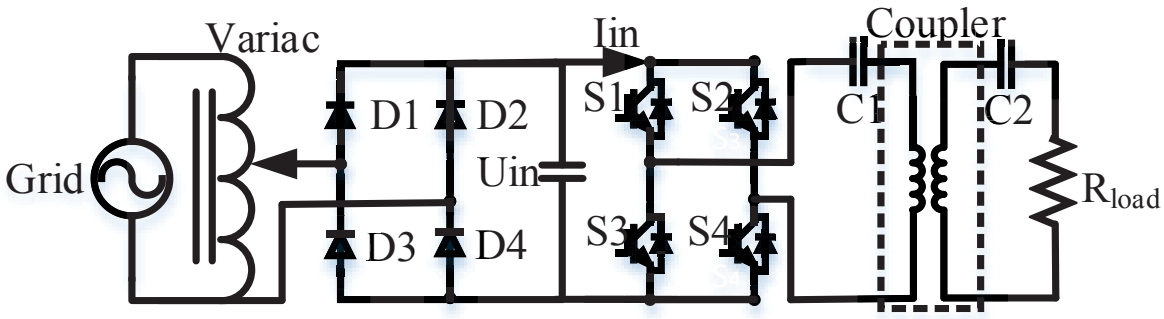

Fig. 5.19. IPT experiment circuit.

The experimental rig is shown in Fig. 5.20 and Fig. 5.21.

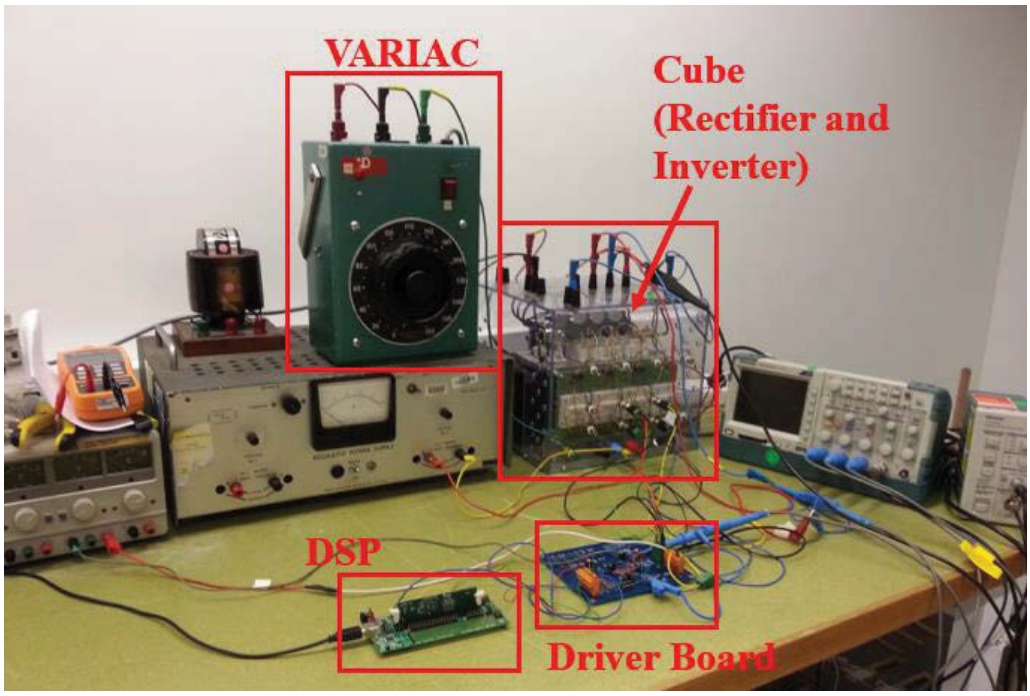

Fig. 5.20. Test rig: primary side.

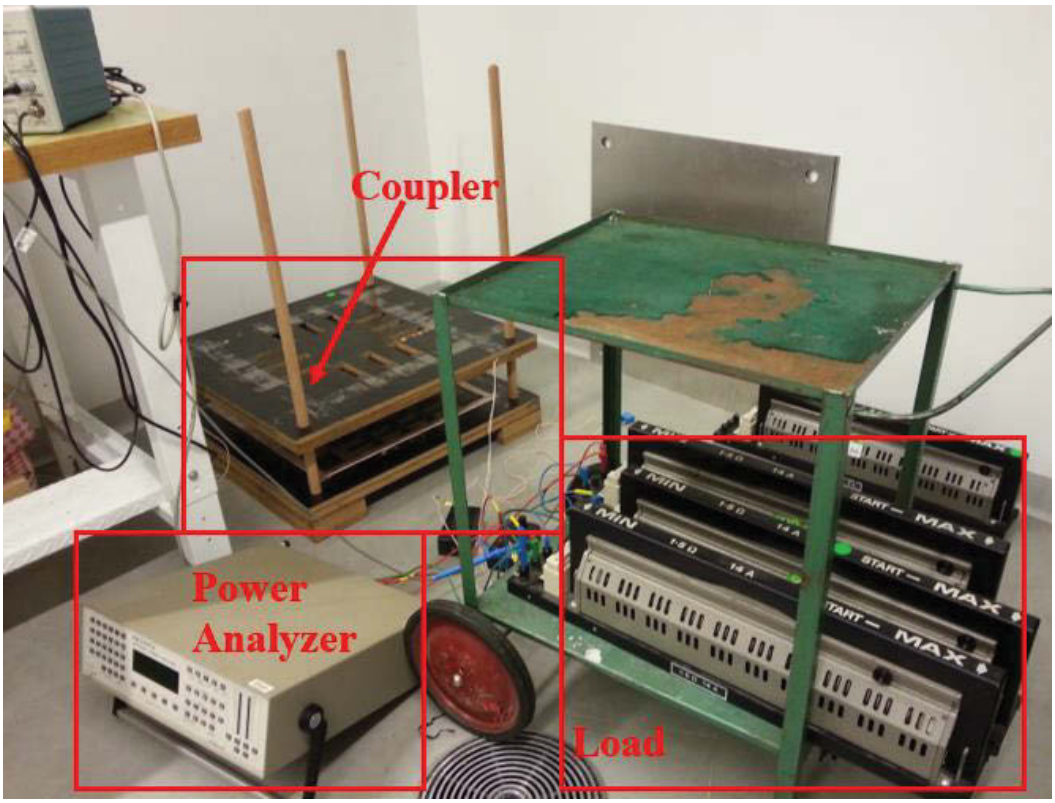

Fig. 5.21. Test rig: coupler and load.

5.3.1 Coupler setup

The coupler tested in chapter 3 is used in the experiment. The 350*0.08mm Litz-Wire has been used for the coupler windings. Both windings have ten turns of wires. The Primary winding was finished as shown in Fig. 5.22 a) and the coupler is shown in Fig. 5.22 b).

As Litz-wire has plenty of thin strands, the coating on each strands needs to be removed properly, which is not possible to be done using soldering iron or burned by fire. The soldering pot was employed in removing the coating and soldering.

The primary side uses 186*28*16 mm ferrite bars, and the secondary side uses the 93*28*16mm. The winding inductances and mutual inductance are shown in Table 3-8 and 3-9.

The capacitances of compensation capacitors are 330nF for both primary and secondary sides, and the compensation is SS connected.

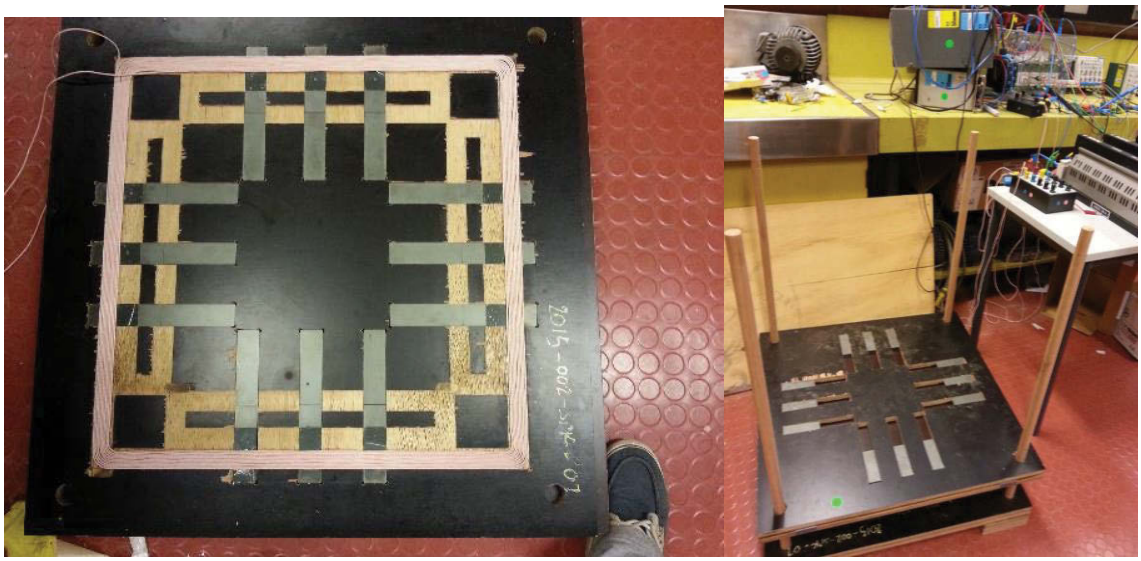

a) b)

Fig. 5.22. a) Coupler primary side, and b) Coupler

5.3.2 Power Electronics setup

A) Rectifier and Inverter

The SEMIKON Cube, which has three phase bridge rectifier and three phase bridge inverter, is used for primary side rectifier and inverter. The rectifier and inverter module in SEMOKON Cube is shown in Fig. 5.23. The rectifier is SKD 51 module, which is a three phase diode rectifier, and it also could be used as single phase rectifier. The full bridge inverter consists of two SKM 50 GB dual IGBT modules. Each module is composed of two series connected IGBTs and used as one leg of the bridge.

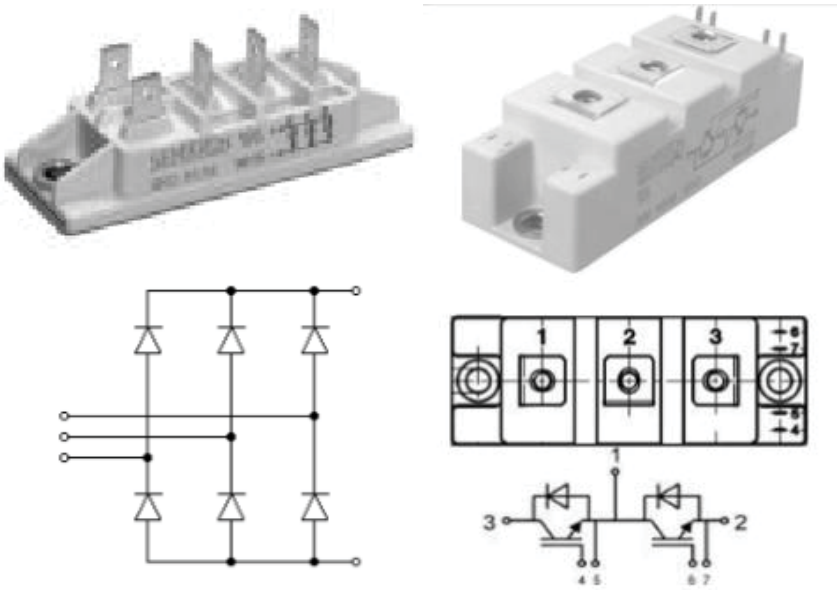

Fig. 5.23. Rectifier module and IGBT module for experiment.

The primary side DC bus capacitors are electrolytic capacitors, and their individual value is 2200 μF/400 V, 2 connected in series, 2 in parallel. The equivalent capacitance of the complete DC bus is 1100 μF/800 V.

B) Gate Driver

The SEMIKON cube has internal gate drivers for IGBT bridges. However, the required input is 15 V, which is not on the same level of the DSP output. Therefore, INFINEON IR2003 half bridge drivers are used to boost the voltage of DSP output from 3.3 V to 15 V and it is used as the input for the internal full bridge inverter driver. The Schematic and Printed Circuit Board (PCB) of the driver board are shown in Fig. 5.24, and Fig. 5.25.

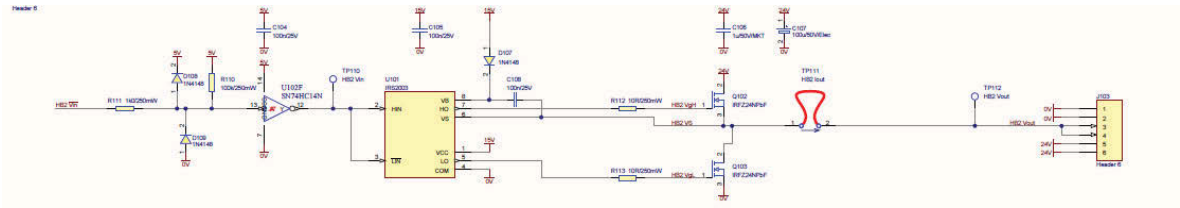

Fig. 5.24. Schematic diagram of gate drive.

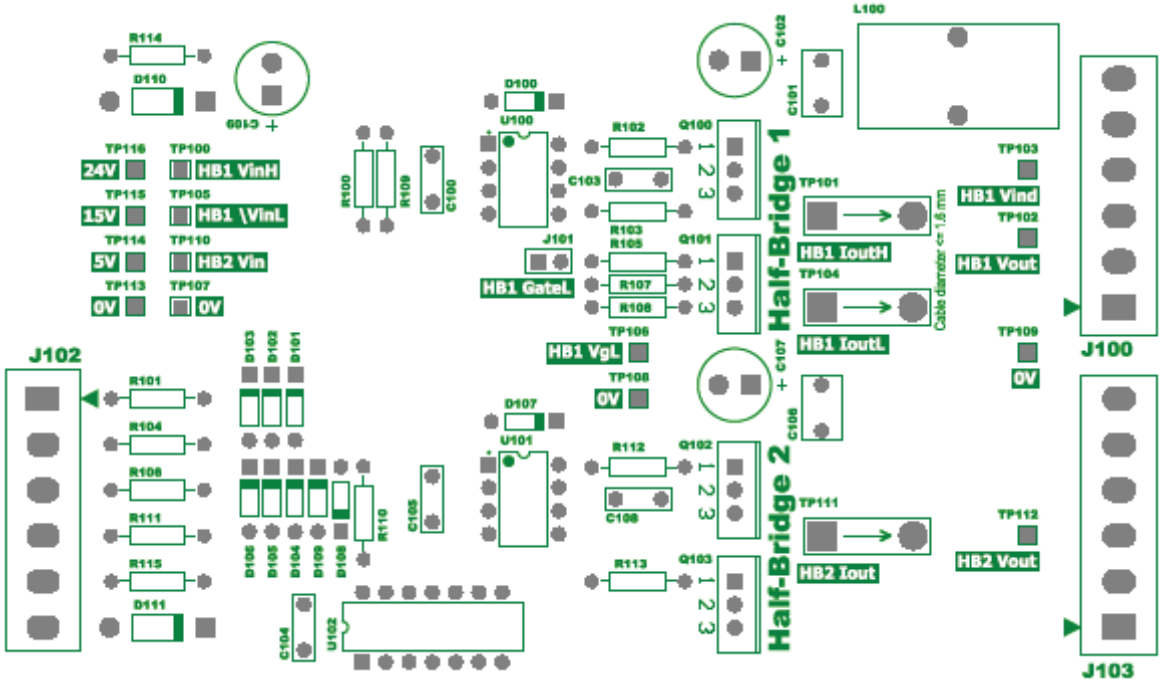

Fig. 5.25. PCB view of gate drive.

5.3.3 Experiment Result

The DSP output PWM, gate driver PWM and output voltage of full bridge inverter are shown in Fig. 5.26. The system frequency is 19,600 Hz. The DSP output is 3.3 V and the gate driver output voltage is 15 V. The peak to peak output voltage of inverter is 100 V.

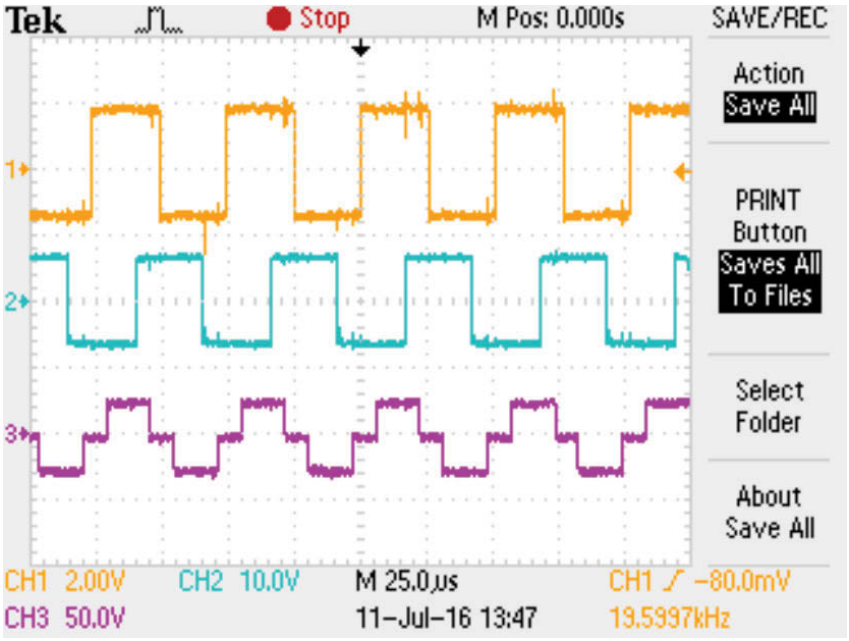

Fig. 5.26. DSP output, gate drive signal and the inverter output.

Fig. 5.27 shows the time delay between the gate driver signal and the inverter output voltage. The delay is 4.8 us, which is caused by the gate driver recharging time.

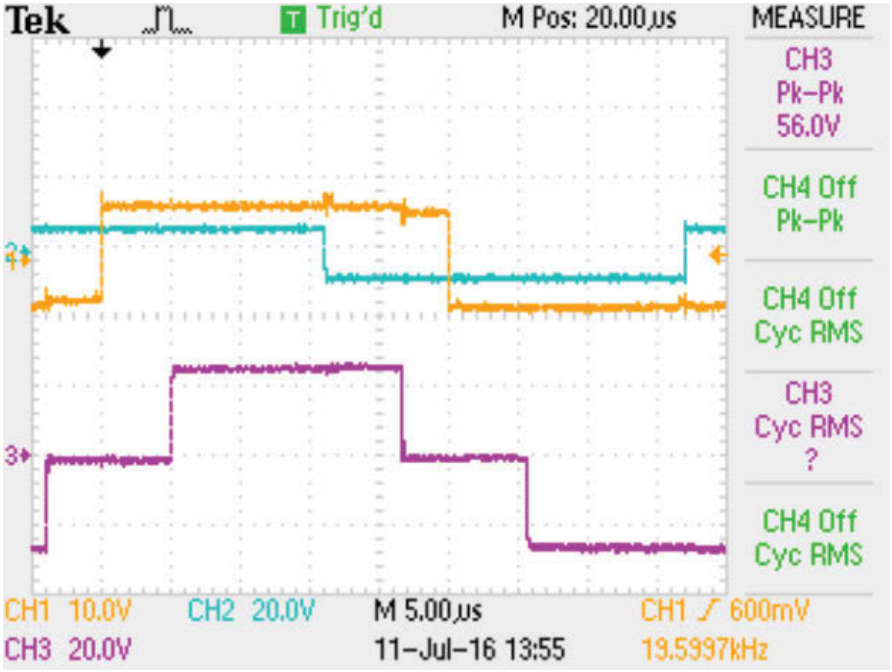

Fig. 5.27. Time delay between the drive signal and the output voltage.

The primary inductance is 199.8 uH, and the secondary side inductance is 192uH. The coupling coefficient k is 0.2 at 15cm. The load is composed of two series connected variable resistors, which has 3.5 Ohm total resistance, and 8 uH inductance. The compensation capacitors in primary and secondary sides are both 330 nF.

The input voltage and current for the primary side for a 346 W test are shown in Fig. 5.28. The top waveform is the output voltage of the inverter, and the bottom waveform is the inverter output current waveform. The system input power in the middle is calculated from inverter output voltage and current waveform. The output power to the load is measured using power analyser as shown in Fig. 5.29. A maximum power of 1.03 kW was transferred to the resistance load with efficiency of 83% at 21 kHz, 15 cm airgap in experiment. Transferring higher power is possible. However, due to current limitation of the load, it was not performed.

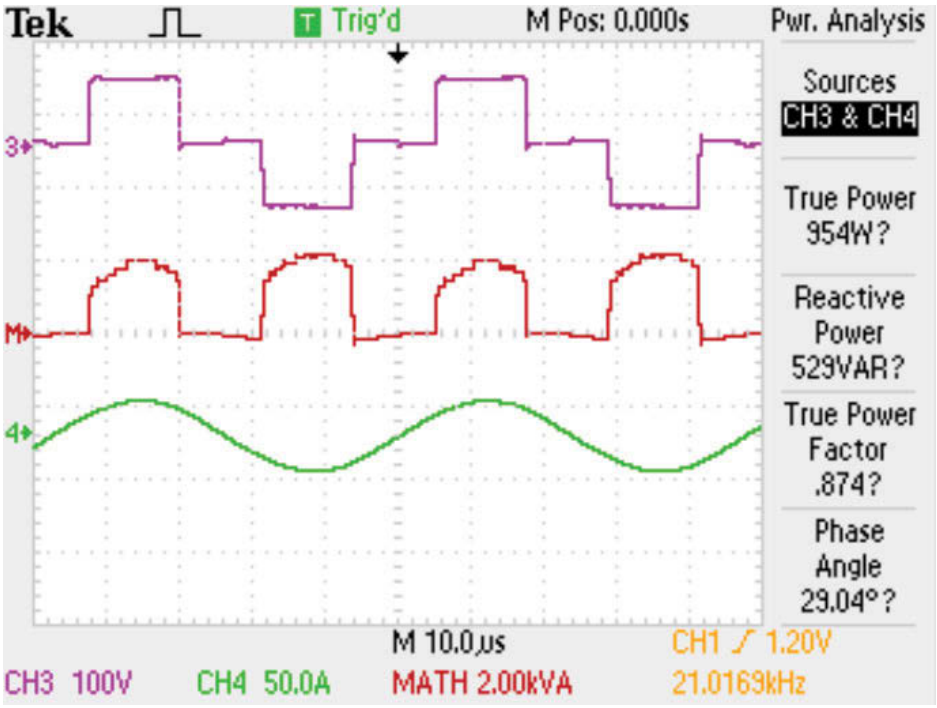

Fig. 5.28. The voltage and current inputs of the primary side.

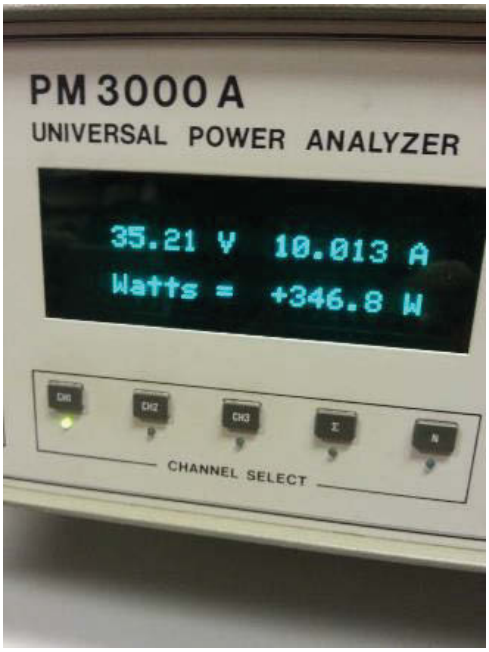

Fig. 5.29. The voltage, current and power to the load.

The output voltage and current of inverter at 21 kHz and 20 kHz are shown in Fig. 5.30 Fig. 5.31

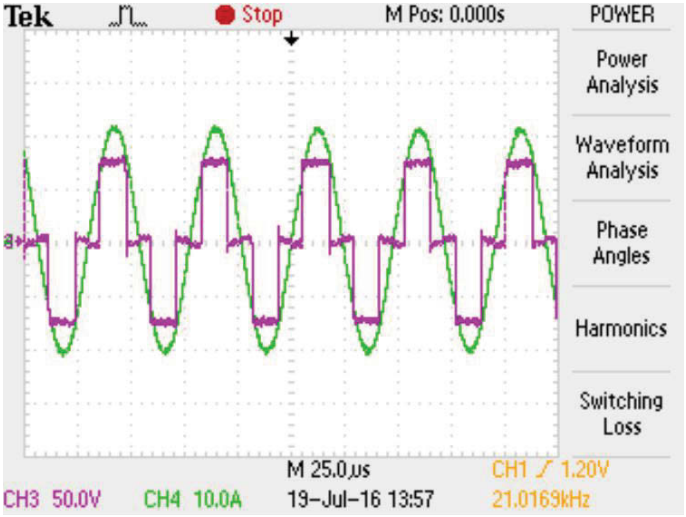

Fig. 5.30. Inverter output voltage and current at 21 kHz.

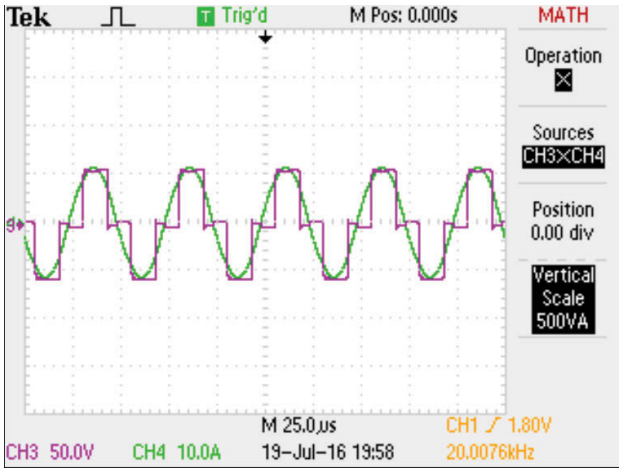

Fig. 5.31. Inverter output voltage and current at 20 kHz

Table 5-5 shows the system efficiency with different loads at 21 kHz. The maximum measured efficiency is 84.9%. The efficiency in the circuit analysis simulation reaches 90%, which is higher than the experiment. The reason might be that some of the wires are lab

wires which have higher resistance than the Litz wire. Fig. 5.32 shows the efficiency versus load resistance. The highest efficiency happens when the load is around 5 ohm.

Table 5-5. System Efficiency Versus Load

f(kHz)	Input	Output	Vload	Iload	Efficiency
21017	399	320	36.69	8.191	80.2%
21017	356	293.4	38.55	7.889	0.826478873
21017	344	292.2	38.71	7.7	0.849418605
21017	331	280.2	38.68	7.44	0.84652568

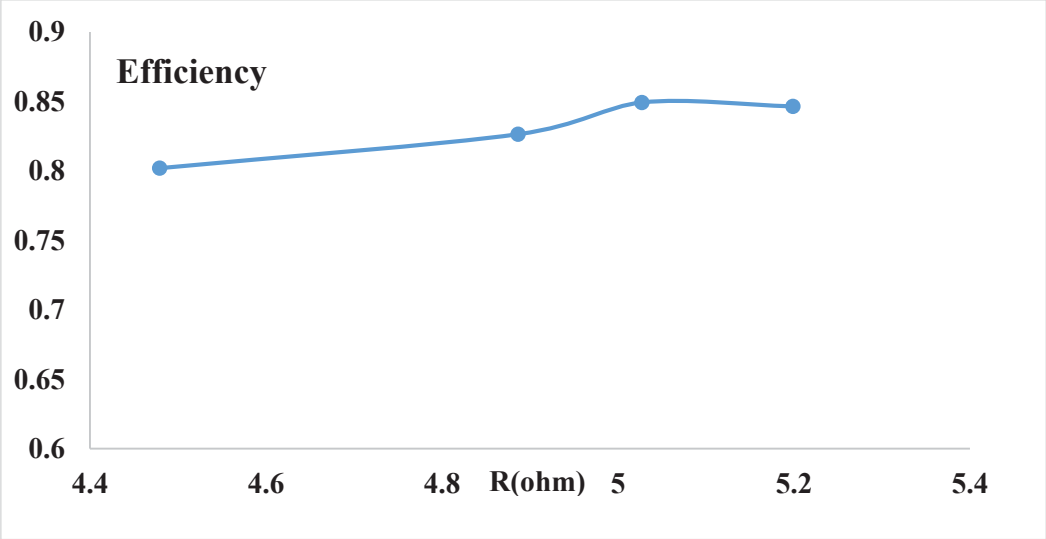

Fig. 5.32. System efficiency versus load resistance

5.4 Summary

In this chapter, the IPT system is analysed on circuit level. The system performance including efficiency and transferred power are investigated. The system performance would be affected by load resistance, mutual inductance, and frequency.

The experiment has been carried out based on analysis. The experiment results validate the circuit analysis.

5.5 References

[5.1] Y. H. Chao, J. J. Shieh, C.-T. Pan, W.-C. Shen and M.-P. Chen, "A primary-side control strategy for series-parallel loosely coupled inductive power transfer systems", Proc. IEEE Conf. Ind. Electron. Appl., pp. 2322-2327.

[5.2] N. Liu and T. G. Habetler, "Design of a universal inductive charger for electric vehicles", Proc. IEEE Transp. Electrification Conf. Expo., pp. 1-6, 2014.

[5.3] H. L. Li, A. P. Hu, G. A. Covic and T. Chunsen, "A new primary power regulation method for contactless power transfer", Proc. IEEE ICIT, pp. 1-5.

[5.4] J. Miller, O. Onar and M. Chinthavali, "Primary-side power flow control of wireless power transfer for electric vehicle charging", IEEE J. Emerg. Sel. Topics Power Electron., vol. 3, no. 1, pp. 147-162, 2015

[5.5] U. K. Madawala and D. J. Thrimawithana, "A bidirectional inductive power interface for electric vehicles in V2G systems", IEEE Trans. Ind. Electron., vol. 58, no. 10, pp. 4789-4896, 2011

[5.6] M. J. Neath, A. K. Swain, U. K. Madawala, D. J. Thrimawithana and D. M. Vilathgamuwa, "Controller synthesis of a bidirectional inductive power interface for electric vehicles", Proc. 3rd IEEE ICSET, pp. 60-65

[5.7] D. J. Thrimawithana, U. K. Madawala and M. Neath, "A synchronization technique for bidirectional IPT systems", IEEE Trans. Ind. Electron., vol. 60, no. 1, pp. 301-309, 2013

[5.8] B. X. Nguyen, "An efficiency optimization scheme for bidirectional inductive power transfer systems", IEEE Trans. Power Electron., vol. 30, no. 11, pp. 6310-6319, Nov. 2015.

[5.9] T. Diekhans and R. W. D. Doncker, "A dual-side controlled inductive power transfer system optimized for large coupling factor variations and partial load", IEEE Trans. Power Electron., vol. 30, no. 11, pp. 6320-6328, Nov. 2015.

[5.10] A. Berger, M. Agostinelli, S. Vesti, J. Oliver, J. Cobos and M. Huemer, "A wireless charging system applying phase-shift and amplitude control to maximize efficiency and extractable power", IEEE Trans. Power Elect., vol. 30, no. 11, pp. 6338-6348, 2015

CHAPTER 6

Conclusions and Future Work

6.1 Conclusions

In this thesis, inductive power transfer system has been studied and developed. The general conclusions of this thesis can be summarised as:

1. Review of the state of art of inductive power transfer technology.
2. Analysis of the coupler parameters including size, inductance and mutual inductance with different airgaps and misalignments.
3. Development of coupler winding resistance analysis which has been done using a combination of 2D and 3D finite element analysis.
4. Proposal of a new type of coupler with assistive coils. The compensation for this type of coupler is further investigated.
5. Analysis of the IPT system performance on circuit level, including the efficiency and power versus different coupler parameters, and the results are validated by experiment.

6.2 Future Work

Inductive charging is an attractive solution for EV recharging and it is desired with the potential to extend the EV driving range without additional battery packs on board. Based on the progress obtained from this thesis, the continued work of this research area can be described as

1. Based on the work in chapter 4, optimize the coupler geometry to achieve better performance with misalignment and different airgap distance.

2. Develop dynamic charging system with different coupler geometries. Investigate the system performance with EV at different driving speed, multi-load, and misalignment.

3. Further develop experiment in Chapter 5 with control strategy, considering the power factor control as part of the system control to reduce the voltage stress on the HF inverter, especially at low power output stage.